Politecnico di Torino

Politecnico di Torino

Corso di Laurea Magistrale in Ingegneria Biomedica
A.a. 2024/2025
Sessione di Laurea Marzo 2025

Network-based diffusion analysis and functional connectivity in modelling atrophy progression for early detection of GBA-associated Parkinson's disease

Relatore:
Prof. Molinari Filippo
Correlatori:
Prof. Salvi Massimo
Prof. Filippi Massimo
Prof.ssa Agosta Federica
Dott.ssa Basaia Silvia

Candidato:
Tommaso Cusolito

Contents

1. Parkinson's Disease and GBA Mutation 6
1.1. Parkinson's Disease 6
1.1.1. Epidemiology and Risk Factors 6
1.1.2. Pathology 7
1.1.3. Clinical Features 8
1.1.3.1. Motor Symptoms 8
1.1.3.2. Non-motor symptoms 8
1.1.4. Diagnosis 8
1.1.4.1. Parkinsonian Syndromes 9
1.1.4.2. Neuroimaging 9
1.1.4.3. Rating Scales 9
1.1.5. Treatment 11
1.2. Alpha Synuclein and GBA Mutation 11
1.2.1. Alpha Synuclein 11
1.2.1.1. Physiological Role 11
1.2.1.2. Aggregation of α-Syn 12
1.2.1.3. Prion-Like Behavior 13
1.2.1.4. Other Proteinopathies 13
1.2.2. GBA Mutations 13
1.2.2.1. Glucocerebrosidase 14
1.2.2.2. Impact of GBA Mutation on PD 14
2. Magnetic Resonance Imaging 15
2.1. Basic Principles 15
2.1.1. Source of MR Signal 15
2.1.2. Excitation and Relaxation Phase 16
2.1.3. Spatial Encoding 17
2.1.4. Contrast Modulation 19
2.1.5. Pulse Sequences 20
2.2. Structural MRI 23
2.2.1. Extraction of GM Thickness 23
2.3. Functional MRI 24
2.3.1. Resting-State Networks 25
2.4. MRI findings in PD Patients 26
2.4.1. Structural MRI findings 26
2.4.2. Functional MRI findings 26
3. Connectomics 27
3.1. Functional Connectome (FC) 27

3.2. Graph Theory 27
3.3. Network Based Statistics (NBS) 28
3.4. Modelling Neurodegeneration 29
3.4.1. Models Based on Local Gene Expression 29
3.4.2. Machine and Deep Learning Models 30
3.4.3. Computational Models based on Network Based Diffusion 31
3.4.4. Network Diffusion Models (NDM) 32
3.4.5. Models Simulating Aggregation 33
3.4.6. Aggregation-Network-Diffusion (AND) Model 34
3.4.6.1. Smoluchowski Aggregation 34
3.4.6.2. Network Diffusion 35
3.4.6.3. Misfolded Monomer Production 36
3.4.6.4. Aggregation and Diffusion Rate 36
3.4.6.5. Complete AND Model 36
3.4.6.6. Results 37
4. Materials and Methods 38
4.1. Subjects 38
4.1.1. Clinical Evaluation 39
4.1.2. Genetic Screening 39
4.1.3. Neuropsychological and Behavioural Evaluations 40
4.2. MRI Acquisition 40
4.3. MRI Analysis 41
4.3.1. Brain Parcellation 41
4.3.1.1. Cortical Thickness Measurement 41
4.3.1.2. Gray matter volumetry 41
4.3.1.3. Cortical Thickness and GM Volumetry Normalization 42
4.3.2. Functional Connectivity 42
Rs-fMRI Preprocessing 42
4.3.2.1. Functional Connectome Reconstruction 42
4.3.2.2. Structural Connectome Construction of Independent Controls 43
4.4. Connectomics 44
4.4.1. Graph Analysis 44
4.4.2. Network Based Statistics 47
4.5. Model 47
4.5.1. System of Ordinary Differential Equations (ODE) 47
4.5.2. ODE45 49
4.5.2.1. Initialization 49
4.5.2.2. Configuration 49

4.5.3. Evaluation of System Output 50
4.5.4. Optimization 50
4.5.4.1. Seed Region Selection 50
4.5.4.2. Exploration of Suitable Parameters Bounds 51
4.5.4.3. Protein Form Selection 51
4.5.4.4. Constant Optimization 52
5. Results 53
5.1. Connectomics 53
5.1.1. Graph Analysis 53
5.1.2. Network Based Statistics 53
5.2. Simulating Atrophy 54
5.2.1. Seed Region Selection 54
5.2.2. Exploration of Suitable Parameter Bounds 55
5.2.3. Protein Form Selection 56
5.2.4. Performance of the Optimization Process 57
5.2.5. Parameters Selected in the Optimization Process 58
5.2.6. Regions Selected in the Optimization Process 59
5.2.7. Characteristic Atrophy Patterns 59
5.2.8. Spatial and Temporal Evolution of Simulated Atrophy 60
6. Discussion 62
6.1. Connectomics 62
6.2. Neurodegeneration Modelling 62
7. Conclusion 64
Bibliography 65

Abstract

Parkinson’s disease (PD) is a prion-like neurodegenerative disorder driven by α-synuclein misfolding, spreading pathology across the brain, especially in cases with GBA mutations. Advances in MRI processing, such as graph analysis and connectomics, help map brain-wide functional connectivity and clarify neurodegenerative mechanisms. Network analysis reveals how diseases alter brain organization and hypothesizes abnormal protein spread. The Aggregation Network Diffusion (AND) model predicts future pathology based on baseline data, simulating misfolded protein spread and aggregation into neurotoxic forms. To account for individual variability in disease progression, AND must adapt to subject-specific dynamics for accurate atrophy modelling. Thirteen GBA-positive, 39 GBA-negative PD patients and 60 age- and sex-matched controls underwent clinical evaluation, 3DT1-weighted and resting-state functional MRI (rs-fMRI) at baseline and, only PD patients, over a 7-year period. Functional connectome for each subject was obtained from rs-fMRI scans as the Pearson’s correlation coefficient between time-series in 83 cortical and subcortical brain regions. Graph analysis and connectomics assessed global and local functional topologic network, and regional functional connectivity using Network Based Statistics (NBS). AND model was developed to predict PD pathology progression as a spreading process from a seed through an averaged functional connectome extracted from healthy controls. Pearson’s correlations were calculated between AND-predicted atrophy and the observed longitudinal atrophy in PD patients over follow-ups of 7-years. Through the use of grid searches and optimization methods, the model was tailored to each individual, maximizing correlation values by refining model parameters, and selecting seed regions. Relative to controls, GBA-positive PD patients showed severe global functional network alterations, while GBA-negative patients showed relatively preserved functional brain architecture. Considering NBS analysis, functional connectivity breakdown in the parietal lobe, temporal, and occipital, sensorimotor, and right frontal differentiated GBA-positive PD patients from controls. AND model produced highly variable results across both groups. Seed region identification showed overlapping patterns across both groups. In GBA-negative patients, the model primarily selected regions in the temporal lobe, with secondary preference for the frontal lobe. Similarly, in GBA-positive patients, regions were mainly located in the temporal lobe, with additional preference for the basal ganglia and sensorimotor lobe. Parameter optimization enabled detailed analysis of simulated atrophy patterns, with the global network "transmissibility" constant, beta, emerging as the key factor. Lower beta values, with a seed region in the temporal lobe, led to early involvement of the basal ganglia, frontal, and temporal lobes at 24 months, followed by progression to the parietal, sensorimotor, and occipital lobes at later stages. In contrast, higher beta values, starting from the same lobe, resulted in early involvement of the basal ganglia, temporal, frontal, parietal, and sensorimotor lobes, with later progression to the occipital lobe. These findings show that GBA mutations drive distinct functional network changes in PD. Patient-specific spreading patterns confirmed the need for individualized model fitting. Integrating predictive modelling with connectivity analysis offers new insights into PD progression.

1. Parkinson's Disease and GBA Mutation

1.1.Parkinson's Disease

Parkinson's Disease (PD) is a progressive neurodegenerative disorder first identified in 1817 by surgeon James Parkison and later distinguished it from other tremor-related conditions by neurologist Jean-Martin Charcot, identifying PD as a separate movement disorder. (1)

PD presents a range of symptoms, both motor and non-motor, that can impact the way of life of those affected. The main motor symptoms include tremor, rigidity, bradykinesia (or akinesia), and postural instability with additional motor features that may include reduced facial expression, speech and swallowing difficulties. These symptoms progressively worsen over time, exacerbating disability and mortality while diminishing quality of life. Non-motor symptoms, which can precede motor signs by years, encompass mood disturbances (e.g., depression and apathy), cognitive impairment, fatigue, sleep disorders, and autonomic dysfunctions such as orthostatic hypotension and excessive sweating. (2)

While rates vary significantly, the neurodegeneration progression is a characteristic of PD which is used for diagnosis. Both lack of progression and rapid declines may point to an exclusion of PD or other alternative diagnosis respectively. PD neurodegeneration often shortens life expectancy, but many individuals can deal with its symptoms for decades, such as cognitive and motor decline. The onset of disability may put those affected in need of personal or long-term care, placing considerable strain on caregivers and family.

1.1.1. Epidemiology and Risk Factors

Globally, neurological disorders are the leading cause of disability with PD ranking 10th in terms of global disease burden. In 2019, more than 8.5 million people were reported to be living with PD worldwide (3). PD has a higher prevalence in developed regions in North America and Europe but this datum might be affected by underreporting in less-developed regions making it difficult to identify the true global burden of the disease (4).

The same global epidemiological trends can be found in Italy with a 2020 systematic review and meta-analysis which found the prevalence of PD in Italy to be 1937 per million individuals, with a sharp increase with age, which is confirmed to be the most significant risk factor in this population too (5). The male-to-female prevalence ratio is also consistent with global data with men being more likely to develop PD. Moreover, demographic variation in Italy, due to its aging population, increases the burden of degenerative diseases significantly stressing the national healthcare system (5).

Aging is indeed a major contributor as most cases occur after 60 and early-onset PD, with diagnosis before 50, comprise only 4% of the total (6). Another factor is a family history of PD since first-degree relatives have an approximately two- to three-fold higher risk of developing it and familiar forms contributing to 5-15% of all cases (7). Key genetic mutations can also affect disease progression with SNCA mutations associated with earlier disease onset, faster progression, and prominent non-motor symptoms. Other mutations include those in LRRK2, PRKN, PINK1 and GBA genes (8). Although not common, GBA mutations are noteworthy for their link to earlier onset, severed disease progression and rapid cognitive decline (9).

1.1.2. Pathology

PD is characterized by the loss of dopaminergic neurons in the substantia nigra (SN), the striatum, the globus pallidus and the thalamus. These regions are related to the control of voluntary movement and the limitation of involuntary actions.

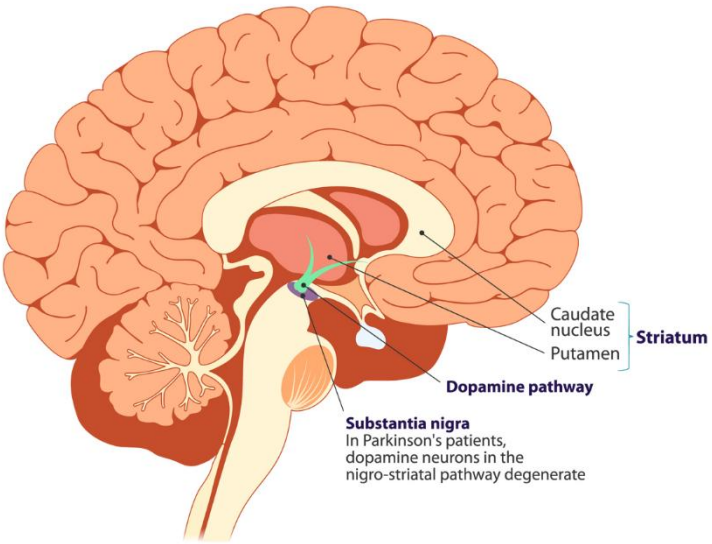

Figure 1.1.2.1: Neuroanatomy of brain regions mainly affected by Parkinson's Disease (10)

The degeneration of dopaminergic neurons, the formation of Lewy Bodies (LBs) and the depigmentation of the *pars compacta* of the SN are all PD features revealed by post-mortem examinations. Lewy bodies are caused by misfolded alpha-synuclein (α-Syn) proteins which lead to the formation of insoluble spherical, eosinophilic inclusions within neurons, composed of more than 90 proteins, with alpha-synuclein and ubiquitin as the primary components.

While post-mortem disease characterization is clear, the early identification of PD is more challenging as 30% of dopaminergic neurons may be lost once the motor symptoms begin, ramping up to 60% once they are detectable (11). This lag is partly due to the ability of the brain to compensate and adapt to neuronal loss and damage.

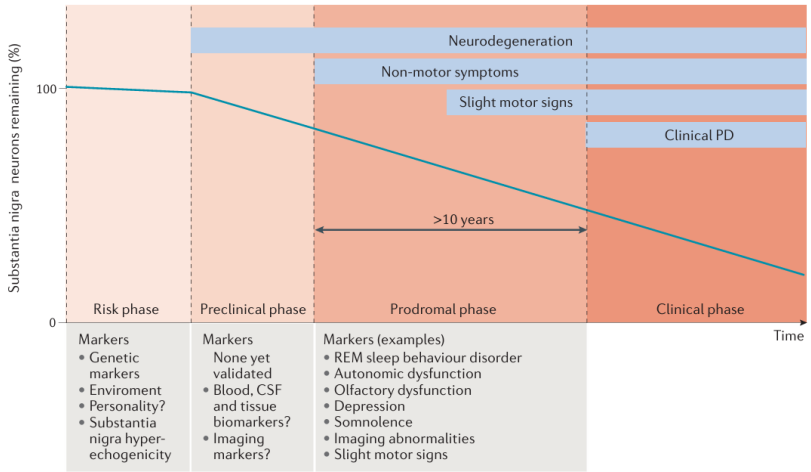

Figure 1.1.2.2.: SN Neuronal Quantity Decline with PD Phase Progression (11)

1.1.3. Clinical Features

Parkinson's disease manifests with both motor and non-motor symptoms which evolve in intensity as the disease progresses.

1.1.3.1. Motor Symptoms

The PD diagnosis comes with the identification of specific motor affections, chief among them is the presence of bradykinesia in association with tremors and rigidity, which is often asymmetrical. Other symptoms can range across postural instabilities, postural abnormalities, gait disturbances and freezing-of-gait (FoG) episodes. Another confirmation of PD can be achieved through means of observation of the alleviation of these symptoms as the patient is treated with levodopa (12).

The following motor symptoms, along with their clinical context, are critical for PD diagnosis and management:

- **Bradykinesia**: Characterized by slowed movements with reduced amplitude, often accompanied by hypomimia, hypophonia, reduced blinking, and fine motor difficulties like micrographia or inability to fasten buttons.
- **Tremor**: A resting, low-frequency tremor often begins unilaterally and may later affect both sides. It diminishes with voluntary movement and is differentiated from essential tremor, a separate neurological disorder which affects action movements.
- **Rigidity**: Stiff limbs, torso, or shoulders, often mistaken for arthritis or injuries.
- **Postural Instability**: Difficulty maintaining balance with an increased fall risk, particularly in later stages.
- **Gait Disturbances**: Common in advanced PD, including Freezing of Gait (FoG), a temporary failure to step, and festination, a reduction of step size and an increase in step frequency often preceding FoG.
- **Speech Impairments**: Hypokinetic dysarthria causing reduced volume, monotone pitch, breathiness, and articulation issues.

1.1.3.2. Non-motor symptoms

Earliest indicators of PD are non-motor symptoms which include depression, constipation and REM sleep behaviour disorder. These can show up to 15 years prior to clinical diagnosis and their recognition opens the door for early intervention and tracking strategies. (13)

1.1.4. Diagnosis

In-vivo clinical PD diagnosis as described by the Movement Disorder Society (MDS) (14) relies on the identification of some of the most common motor symptoms such as bradykinesia alongside with tremor or rigidity. Researchers are focused on the task of the identification of biomarkers for PD to allow for an early identification which is not achievable only looking at the aforementioned criteria. Furthermore, the latter can only provide a probable diagnosis, and histopathology is the only method which provides certainty of PD. Additional confidence of diagnosis can be acquired by looking at patient response to dopaminergic therapy such as dyskinesia, rest tremor in a limb, olfactory loss, and cardiac sympathetic denervation.

On the other hand, a loss of diagnosis confidence can be induced by several factors, such as a rapid progression of gait impairment or a lack of it over five or more years, respiratory disfunction, and severe autonomic failure within the first five years of the disease. The absence of common non-motor symptoms can also put cast doubts on the diagnosis. Certain criteria definitively rule out a diagnosis of Parkinson's disease. These include evident cerebellar abnormalities, cortical sensory deficits, downward supranuclear gaze palsy, a confirmed diagnosis

of probable behavioral variant frontotemporal dementia or primary progressive aphasia, parkinsonism confined to the lower limbs for over three years, lack of any observable response to high-dose levodopa, and normal functional neuroimaging of the presynaptic dopaminergic system.

1.1.4.1.Parkinsonian Syndromes

To administer proper care, it's necessary to differentiate between the various Parkinsonian syndromes. Stratification is useful for the identification of symptoms, prognoses and potential treatments (15). The primary syndromes are:

- Idiopathic Parkinson's Disease: the most common form of PD, defined by hallmark motor symptoms such as tremor, rigidity, and bradykinesia.
- Dementia with Lewy Bodies (DLB): showing symptoms of dementia and parkinsonism, with visual hallucinations, fluctuating cognition, and REM sleep behavior disorder.
- Progressive Supranuclear Palsy (PSP): showing postural instability, gait disturbances and cognitive decline, with faster progression.
- Multiple System Atrophy (MSA): a separate neurodegenerative disorder affecting multiple systems, presenting with parkinsonism, autonomic dysfunction, and cerebellar ataxia.
- Corticobasal Degeneration (CBD): triggering asymmetric motor symptoms, cognitive impairment, and phenomena such as the "alien limb".
- Vascular Parkinsonism (VaP): presents cerebrovascular disease and may respond to treatment of underlying vascular issues.

1.1.4.2.Neuroimaging

While neuroimaging is not used for PD diagnosis, brain MRIs are useful to exclude structural abnormalities which might explain the presence of Parkinson's-like features and provide additional information which may lead to alternative diagnosis of MSA or PSP.

A single photon emission computed tomography using 123I-FP-CIT (DaTscan) highlighting striatal dopamine transporter allows to quantify presynaptic dopamine transporter density and observe loss of dopaminergic neurons. The technique is especially useful in scenarios where the diagnosis remains uncertain after other clinical evaluations (16) and the patient is supposed to receive implants for deep brain stimulation (DBS) as it requires a higher diagnosis confidence due to the invasiveness of the procedure.

1.1.4.3. Rating Scales

Clinical evaluation for PD uses standardized tools and scales such as the Movement Disorder Society - Unified Parkinson's Disease Rating Scale (MDS-UPDRS) and Hoehn and Yahr scale to rate disease progression and motor impairment.

a) Hoehn and Yahr

The Hoehn and Yahr (H&Y) scale was first introduced in 1967 and is a widely used clinical tool to evaluate the severity of PD symptoms. It ranges across stages 1 through 5 where each stage indicates a different grade of disability. Stage 1 refers to unilateral involvement, followed by bilateral involvement without balancing issues at stage 2, postural instability at stage 3, loss of physical independence at stage 4, and being wheelchair or bed-bound at stage 5.

The severity of these motor symptoms correlates with neurocognitive complications, such as dementia, depression, and hallucinations, getting more severe with higher scores.

A modified version of the H&Y scale introduced in the 1990s includes 0.5-point increments, improving its descriptive accuracy. Both versions are quick to administer, typically requiring less than five minutes as clinicians observe patients performing tasks.

H&Y and mH&Y

Stage	Hoehn and Yahr Scale	Modified Hoehn and Yahr Scale
1	Unilateral involvement only usually with minimal or no functional disability	Unilateral involvement only
1.5	-	Unilateral and axial involvement
2	Bilateral or midline involvement without impairment of balance	Bilateral involvement without impairment of balance
2.5	-	Mild bilateral disease with recovery on pull test
3	Bilateral disease: mild to moderate disability with impaired postural reflexes; physically independent	Mild to moderate bilateral disease; some postural instability; physically independent
4	Severely disabling disease; still able to walk or stand unassisted	Severe disability; still able to walk or stand unassisted
5	Confinement to bed or wheelchair unless aided	Wheelchair bound or bedridden unless aided

Table 1.1: Hoehn and Yahr (H&Y) scale and its modified version (mH&Y) scale

b) Unified Parkinson's Disease Rating Scale (UPDRS)

The UPDRS is a comprehensive tool used to assess various aspects of PD, divided into four parts:

- Part I: Non-Motor Experiences of Daily Living
    - Comprises 13 questions, divided into two sections:
        - Part IA: Six clinician-administered questions assessing complex behaviors.
        - Part IB: Seven self-administered questions evaluating non-motor symptoms.
- Part II: Motor Experiences of Daily Living
    - Assessing how motor symptoms impact daily activities and functionality.
- Part III: Motor Examination
    - Evaluating motor signs of PD while noting whether the patient is in the ON or OFF medication state and accounting for co-existing medical conditions.
- Part IV: Motor Complications
    - Evaluating motor fluctuations, dyskinesias, and complications like OFF-state dystonia, with a summarization of the patient's functional status over the previous week.

In summary, the UPDRS provides an evaluation of both motor and non-motor symptoms, with a detailed overview of the patient’s clinical condition and disease progression.

1.1.5. Treatment

Current therapies focus on symptom alleviation as there are none which modify disease progression. The main strategies depend on dopamine replacement with the alternative use of DBS for advanced PD. While these therapies are effective in managing motor symptoms, they don't affect disease progression thus making the patient dependent and at high risk to develop side effects. These include levodopa-resistant symptoms such as freezing, dysarthria, dysphagia, hallucinations, cognitive decline, sleepiness, and incontinence (17).

- Levodopa

Levodopa is the most effective treatment for symptom management. It can cross the blood-brain barrier and arrive to the substantia nigra where it can be converted to dopamine and supplied to the remaining dopaminergic neurons.

Unfortunately, it carries a limitation which is the development of motor complications after repeated use, such as fluctuations, dyskinesia and dystonia. Additional side effects include manifestations of symptoms of nausea, hypotension, confusion, hallucinations, and impulse control disorders which become more common as higher doses are required.

On the other hand, levodopa's effects are rapid and last several hours for patients in the early stages. The situation changes as the disease progresses, shortening the effect of symptom relief thus requiring more frequent dosing. 'OFF' states experienced by patients may be characterized by severe motor symptoms similar to the ones observed in advanced states. (18)

- Dopamine Agonists

Dopamine agonists directly stimulate dopamine receptors in the striatum, bypassing the need for conversion by dopaminergic neurons. While they are less effective than levodopa for managing motor symptoms, they carry a lower risk of side effects. Dopamine agonists may be used as monotherapy in early stages or in combination with levodopa (17).

- Deep Brain Stimulation (DBS)

A surgical treatment option for advanced PD is the implantation of devices for Deep Brain Stimulation (DBS). This approach involves delivering high-frequency electrical currents to specific brain regions, typically the subthalamic nucleus, globus pallidus internus, or thalamus. The currents modulate neural circuits which are responsible for movement with excitatory and inhibitory effects.

Unfortunately, DBS carries a series of potential side effects due to the complexity of the procedure and due to the possibility of developing cognitive decline and psychiatric disturbances limiting its possible application. Despite these risks, it remains a valuable option for appropriately vetoed patients with advanced PD. (19)

1.2.Alpha Synuclein and GBA Mutation

1.2.1. Alpha Synuclein

One of the defining characteristics of PD is the accumulation of the protein alpha-synuclein (α-Syn) in the brain, affecting the development and progression of the disease (20)

1.2.1.1. Physiological Role

α-Syn is a small, soluble protein found in presynaptic terminals of neurons where it regulates neurotransmitter release. It is encoded in the SNCA gene, and its mutations can lead to α-Syn misfolding.

Its intrinsic disorder under physiological conditions allows for a high degree of structural flexibility which enables interaction with a wide range of molecular targets but also makes it prone to misfolding. In its native state, α-Syn exists in various forms, including monomers, oligomers, and membrane-bound conformations, with its state influenced by pH, lipid composition, and protein concentration (21).

The regulating role of α-Syn is to facilitate the assembly and maintenance of the SNARE (soluble N-ethylmaleimide-sensitive factor attachment protein receptor) complex which is responsible for efficient neurotransmitter release. (22)

In PD, however, α-Syn becomes misfolded and aggregates into insoluble fibrils and other abnormal clumps of protein found inside neurons (23). This misfolding disrupts α-Syn's normal functions and contributes to the formation of Lewy bodies, a pathological hallmark of PD. Both genetic and environmental factors can drive this process such as mutations in the *SNCA* gene (24) and environmental exposures to pesticides. (25)

The presence of these aggregates interferes with cellular processes and contributes to neurodegeneration observed both in PD and other α-Syn related disorder. In summary, α-Syn requires a delicate balance to fulfil its physiological role whose absence can trigger neurodegeneration.

1.2.1.2.Aggregation of α-Syn

Under normal physiological conditions, α-Syn predominantly exists as a monomer in equilibrium with its membrane-bound or tetrameric forms. The tetrameric state is particularly resistant to pathogenic aggregation. However, disruptions in this equilibrium, triggered by changes in the cellular environment or stressors, can result in monomer assembly and subsequent oligomer formation. Notably, monomeric α-Syn is kinetically stable under physiological conditions but is susceptible to nucleation at hydrophilic/hydrophobic interfaces, where local protein concentration increases due to amphipathic interactions. α-Syn aggregation follows a nucleation-dependent polymerization mechanism, characterized by three distinct phases: a lag phase, a slow process where monomers form unstable nuclei, an elongation phase and a stationary phase, where dynamic equilibrium between monomers is established (26).

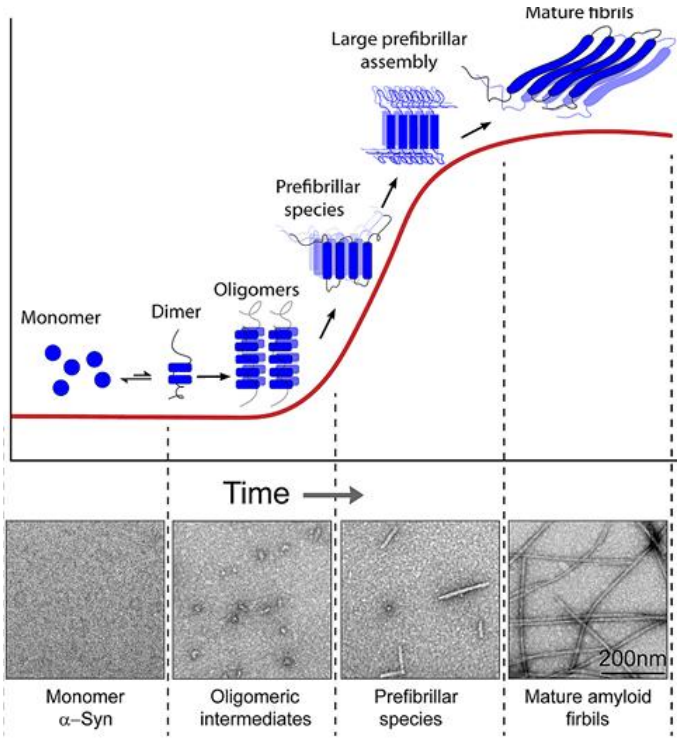

Figure 1.2: Stages of Aggregation of α-Syn (26)

An acceleration of this process can be caused by the presence of preformed fibrillar seeds in a process of heterogeneous nucleation which accelerates aggregation bypassing the lag phase. Through this process, α-Syn aggregation can be triggered in regions which don't produce misfolded α-Syn explaining one of the key mechanisms of disease spread.

The presence of oligomeric intermediates, especially the high molecular weight prefibrillar species, is linked to cellular dysfunction as they interact with organelles disrupting homeostasis. Evidence from transgenic models and human brain samples confirms the presence of such oligomers in synucleinopathies, highlighting their pathological relevance. (26)

1.2.1.3.Prion-Like Behavior

One of the most striking features of misfolded α-Syn is its ability to aggregate and propagate between neurons in a prion-like manner. This behavior implies that misfolded α-Syn can induce properly folded α-Syn proteins in nearby neurons to adopt a similar misfolded conformation, perpetuating a cycle of protein misfolding and aggregation (27). This mechanism of spread contributes to the progressive nature of PD and other synucleinopathies, where pathological α-Syn gradually affects interconnected regions of the brain.

The spreading of α-Syn is believed to happen through different pathways: exosome-mediated, direct cell-to-cell and endocytosis-mediated transmission. All these processes have an end in the transmission of α-Syn within the recipient cell where the misfolded α-Syn acts as a template, inducing normal α-Syn to adopt the pathological conformation (27). At a larger scale and over time, this prion-like spread facilitates propagation and progression of PD.

1.2.1.4.Other Proteinopathies

α-Syn's prion-like behavior is not unique and shares similarities with other misfolded proteins implicated in neurodegenerative diseases, such as tau and beta-amyloid in Alzheimer's disease (AD).

Like α-Syn, tau is a protein that aggregates and spreads across neurons. Misfolded tau is present in all tauopathies, such as AD and frontotemporal dementia. Both proteins use similar mechanisms for propagation, such as exosomal transport and direct cell-to-cell transfer. However, while α-Syn primarily affects synaptic and dopaminergic neurons, tau pathology is often associated with microtubule destabilization and widespread cortical involvement. (28)

In contrast, AD presents beta-amyloid aggregates into extracellular plaques instead of intracellular inclusions while still exhibiting prion-like characteristics with the same misfolding dynamics (29). Another confirmation of the similarity of pathological pathways of α-Syn and beta-amyloid can be found in their co-occurrence within mixed neurodegenerative conditions. (30)

These findings group α-Syn within a category of misfolded proteins which drive neurodegenerative diseases allowing for the sharing of protein dynamics information across the different diseases which ultimately leads to the uncovering of new avenues for therapeutic intervention.

1.2.2. GBA Mutations

Mutations in the GBA gene, which encodes the enzyme glucocerebrosidase (GCase), represent one of the most significant genetic risk factors for PD. GBA mutations are well known for their association with Gaucher's disease, a lysosomal storage disorder, but their link to PD has gained increasing attention in recent years. Epidemiological studies have shown that individuals carrying GBA mutations have a significantly higher risk of developing PD compared to non-carriers (31).

The prevalence of GBA observed in the general population is approximately 4-6% of PD cases in (32). The most common GBA mutations associated with PD include *N370S* and *L444P*, both of which have been implicated in increasing susceptibility to the disease. GBA mutations have also been associated with an earlier

onset of PD symptoms, a greater incidence on cognitive features (33), and a faster progression of both motor and non-motor symptoms (34).

Given the distinct clinical phenotype of PD in GBA mutation carriers understanding the role of GBA mutations and GCase activity is crucial for developing targeted therapies aimed at modifying disease progression.

1.2.2.1.Glucocerebrosidase

GCase plays a critical role in lipid metabolism by operating within lysosomes, the cellular organelles responsible for breaking down and recycling various macromolecules, in particular glucorebroside which is a lipid component of cellular membranes. Its breakdown generated ceramide, which serves as a signaling molecule that regulates apoptosis, cell differentiation, and inflammatory responses.

Impaired GCase activity disrupts lysosomal balance, leading to stress, reduced autophagic clearance and accumulation of undegraded substrates. The combined effects of this stress, toxic alpha-synuclein aggregates, and disrupted cellular signalling ultimately culminates in neuronal death. (35)

1.2.2.2.Impact of GBA Mutation on PD

Numerous studies have demonstrated a mechanistic link between the impaired function of GCase and the accumulation of α-Syn, suggesting that GBA mutations may exacerbate this pathological process.

Bae et al. (2015) investigated the role of glucocerebrosidase deficiency in promoting α-Syn aggregation in neuronal models of PD. Their study found that reduced GCase activity, because of GBA mutations, leads to impaired lysosomal function and subsequent accumulation of α-Syn. This finding suggests that normal GCase function is critical for the degradation of misfolded α-Syn via the autophagy-lysosome pathway. (36)

Maor et al. (2019) expanded upon these concepts by exploring the prion-like spread of α-Syn in *D. melanogaster* in presence of human mutant GCase. Their study provided evidence that GBA mutations increase α-Syn aggregation and accumulation locally within affected neurons. (37)

Migdalska-Richards et al. (2020) investigated the role of a specific GBA mutation, L444P, in formation and spread of α-Syn by injecting pre-formed α-Syn fibrils in mice with a knock-in mutation, finding greater formation and spread of α-Syn compared to wild-type. (38).

Collectively, these studies provide insights into the mechanisms by which GBA mutations accelerate α-Syn aggregation and spread. The primary driver appears to be the deficiency in GCase activity, which leads to lysosomal dysfunction and, consequently, to an impaired autophagy-lysosome pathway, reducing the ability of cells to clear misfolded or aggregated proteins, including misfolded α-Syn.

2. Magnetic Resonance Imaging

Magnetic resonance imaging (MRI) is a non-invasive imaging technique that employs strong magnets and low-energy radiofrequency waves, without using ionizing radiation which characterises techniques providing similar results (39). With advancements in technology and decreasing costs, MRI is becoming more accessible and widely utilized in clinical and research settings.

MRI has its base in the principles of nuclear magnetic resonance (NMR) which was experimentally demonstrated in 1946 by Felix Bloch and Edward Purcell, who in 1952 received a Nobel Prize in Physics for it. NMR's potential for medical diagnostic started being explored in 1971 with Raymon Damadian identifying different relaxation times across different tissue types. The final breakthrough which opened up NMR use to the field of medical imaging was achieved by the work of Paul Lauterbur, Peter Mansfield, and Richard Grannell, who introduced the use of spatially varying magnetic fields for spatial encoding (40).

Contemporary MRI systems utilize cryogenic superconducting magnets, typically operating at field strengths between 0.5 Tesla (T) and 1.5 T, with 3 T systems becoming increasingly prevalent in research settings. Higher field strengths offer enhancements of 30–50% in signal-to-noise ratio (SNR) and of 96% in contrast-to-noise ratio, while also reducing variability. However, these improvements come with drawbacks such as greater susceptibility to artifacts and image distortions (41).

2.1.Basic Principles

2.1.1. Source of MR Signal

MRI uses constant magnetic fields in conjunction with oscillating electromagnetic fields to generate resonance by matching the frequency of spinning nuclei. The latter act like magnets spinning around their own axes while immersed in a constant magnetic field.

The ability of being influenced by such fields is linked to the "spin" property which is dependent upon the number of protons in the nucleus to be considered. Hydrogen is the most frequently used for such analysis, but other possible options include carbon-13, sodium, and phosphorus (39). The uneven distribution of protons and neutrons creates a magnetic moment with a local magnetic field which aligns with the external one [Figure 2.1].

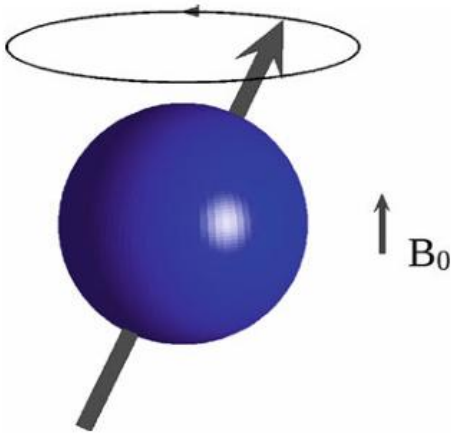

Figure 2.1: Schematic representation of the magnetic moment of a proton and its precession about a magnetic field, B_0 (39)

Without an aligning field, dipoles are randomly oriented in space resulting in a net magnetic vector of magnitude zero. In the presence of a constant external magnetic field B_0, the proton aligns with the field either in the same direction of the field (parallel) or in the opposite direction (antiparallel).

Parallel alignment is energetically favoured thus resulting in most nuclei to be directed in such way resulting in only about 10 out of a million to be directed in the antiparallel way. The presence of the latter manifests in the generation of a net magnetization vector (M_z). As the energy between the two states is matched by incident radiation, the proton can absorb it and change from one state to the other in a process known as magnetic resonance.

Due to the rotational momentum of nuclei, they do not perfectly align with the external magnetic field, they precess around the field direction [Figure 2.1]. The frequency of precession (ω_0), used to trigger magnetic resonance, can be calculated by using the Larmor equation $\omega_0=\gamma*B_0$ where γ is the gyromagnetic ratio of the nucleus.

2.1.2. Excitation and Relaxation Phase

In its equilibrium state, the net magnetization vector (M_z) of nuclei within a magnetic field remains static and does not generate a detectable signal. To extract information from nuclear spins, the direction of the net magnetization must be altered within the static magnetic field (B_0) by applying a radiofrequency (RF) magnetic field (B_1) at the Larmor frequency (resonance frequency), oriented perpendicular to B_0. This energy is typically delivered in short pulses lasting microseconds, and it is absorbed by the nucleus, which then undergoes a transition between energy states, causing the spins to precess in phase.

Under equilibrium conditions in the presence of B_0, the magnetization vector M_0 has only a longitudinal component (M_Z). Applying a 90° RF pulse induces a transition that effectively rotates M_0 by a specific angle relative to B_0. The effect is that the net magnetization (M_Z) flips by 90° into the transverse plane, leaving M_0 with only its transverse component (M_{XY}) [figure 2.2]. As this transverse magnetization precesses around a receiver coil, it induces an alternating current (AC) in the coil according to Faraday's law of electromagnetic induction.

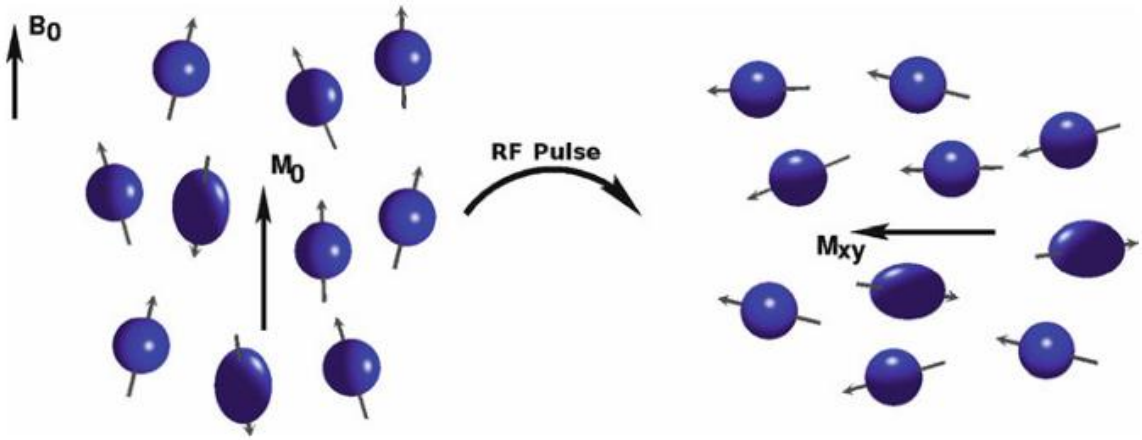

Figure 2.2: Classical representation of the interaction of the spins with a 90° RF pulse to produce spin rotation. This leads to a macroscopic magnetisation, M_{xy}, perpendicular to the static field B_0. (39)

After the RF frequency is stopped, magnetization will decay over time towards the initial state in a process called "Free-Induction Decay" (FID). The detector registers this phenomenon as a sinusoidal signal with an exponential amplitude decrease [Figure 2.3].

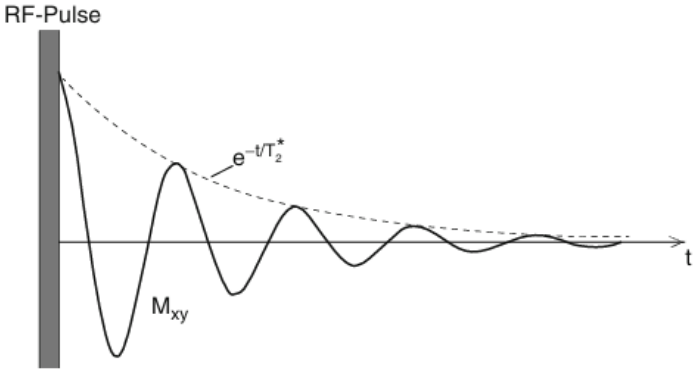

Figure 2.3: Representation of a registered "free induction decay" FID signal. (39)

The restoring of the initial conditions is the process of relaxation, and its timing is a critical aspect. This process is composed of two parts: transverse relaxation and longitudinal relaxation whose timing is independent of each other.

The realignment of the spins to the direction of the external magnetic field is the longitudinal relaxation process and it's linked to the interactions with the environment of the nucleus. Its relaxation time is T_1, defined as the time required for the system to recover 63% of the value at equilibrium.

Transverse relaxation, the second relaxation process, is linked with the precession of spins around the magnetization vector and the gradual loss of phase coherence among them due to spin-spin interactions. Immediately following RF pulse excitation, the spins precess in complete synchrony and, over time, they dephase making the detected signal diminish. This process is characterized by T_2 relaxation time which is the time it takes for dephasing to decay to 37% of its original value.

Another relaxation phenomenon can be observed due to B_0 inhomogeneities which causes differences in precession frequencies across the sample and an acceleration of the dephasing process. The time linked to this exponential decay is T_2* and it's related to the magnetic properties of the sample.

These timings are critical to the identification of different tissues, for example water and cerebrospinal fluid (CSF) have long T_1 values (3000–5000 ms), appearing dark on T_1-weighted images, while fat has a short T_1 value (260 ms) appearing bright on T_1-weighted images.

2.1.3. Spatial Encoding

To generate an image, the MR signal from hydrogen protons must contain spatial information about their positions within the body and this is accomplished through three fundamental steps: slice selection, frequency encoding, and phase encoding. Specifically, magnetic field gradients are used to introduce controlled variations in the static magnetic field strength, thus altering the Larmor frequency, and can be applied along three orthogonal axes using dedicated gradient coils.

To isolate a specific imaging slice a magnetic gradient of approximately 5 mT/m is briefly applied along the longitudinal (z-axis) direction for a few milliseconds. Midway through this gradient application, an RF pulse is delivered into the body consisting of a narrow band of frequencies centred around a target resonance frequency [Figure 2.4]. The latter is dependent on the local magnetic field determined by the sum of the gradient field strength and B_0 allowing for narrow slice acquisition.

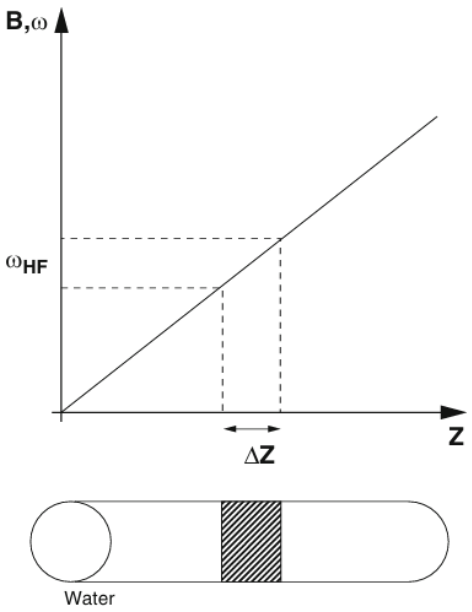

Figure 2.4: Slice selection: the Larmor frequency is varied through the application of a magnetic field gradient which allows for selective excitation of spins. (39)

Following the RF pulse, only the excited protons will undergo relaxation and generate signal, which is detected by the receiving coil. Another parallel slice can be acquired by modifying the excitation frequency. To encode spatial information within a selected slice, frequency encoding and phase encoding are applied, allowing the differentiation of individual points within the slice.

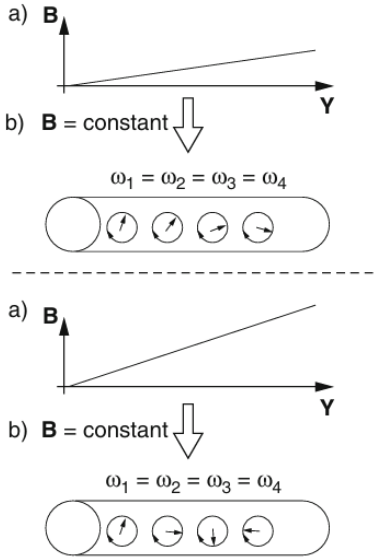

Figure 2.5: Phase encoding: the phase encode gradient is switched on (top) and then off after a short period of time (a) causing a phase shift while retaining frequency once turned off (b). When another line is acquired (bottom), a different phase encoding gradient is used which triggers a different phase shift. Its accumulation is retained up to the time the signal is read. (39)

In phase encoding, a brief, temporary change in the magnetic field along the y-axis is introduced between the RF excitation pulse and signal readout [Figure 2.5]. During this process, spins precess at different frequencies due to the magnetic field variation. However, once the phase-encoding gradient is turned off, all spins revert to precessing at the same frequency while retaining the phase shift.

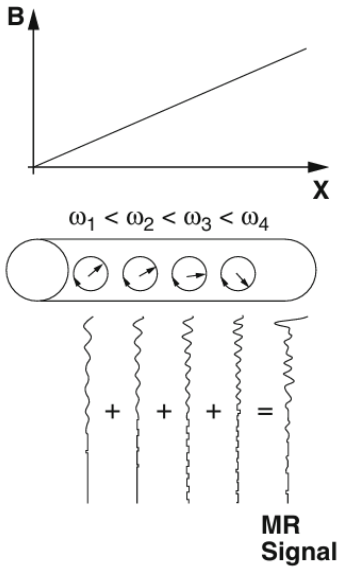

Figure 2.6: Frequency encoding: during acquisition of the signal, a gradient field (orthogonal to the phase encoding direction) is switched on leading to a spatially dependent frequency. (39)

Frequency encoding is used to distinguish pixels that share the same phase encoding by applying a magnetic gradient during the signal readout phase. This causes spins to precess at different frequencies, which correspond to their spatial locations along the applied gradient axis. By analysing the signal frequencies and knowing the amplitude of the readout gradient, each frequency can be correlated with a specific spatial position.

By combining phase and frequency encoding, a structured grid is formed in which each pixel is defined by a unique combination of phase and frequency values. This matrix of raw signal data is referred to as k-space. To reconstruct the image, a fast Fourier transform is applied to the data converting it from an amplitude as a function of time to a function of frequency corresponding to a single spatial coordinate.

The frequency encoding process, which relies on the readout gradient, has minimal impact on total acquisition time due to its short duration, typically lasting only a few milliseconds, while phase encoding significantly influences it, as it requires one RF pulse per echo and is dependent on the repetition time, which is mainly determined by the desired image contrast.

2.1.4. Contrast Modulation

A weighted MRI scan can be performed by leveraging tissue properties which increase its contrast when observed in particular acquisition sequences. T_1-weighted images emphasize differences in longitudinal relaxation times, whereas T_2-weighted images highlight variations in the decay of transverse magnetization. The alteration of these properties, and the resulting variation of contrast, due to pathological conditions is at the basis of the interpretation of MRI for medical diagnosis.

MRI contrast is mainly determined by two key parameters: echo time (TE) and repetition time (TR). Echo time refers to the interval between the radiofrequency pulse and the peak of the detected signal, defining when the signal is measured. Repetition time is the period between successive excitation pulses, which influences how frequently images are acquired. Adjusting TE and TR enables MRI sequences to highlight specific tissue properties and improve diagnostic accuracy [Figure 2.7].

T_2-weighted imaging relies on an extended TE, which allows sufficient time for T_2 relaxation time to happen, and an extended TR, which minimizes T_1 relaxation. Typically, an echo time longer than 80 milliseconds is chosen to enhance tissue contrast, while TR is set above 2 seconds to optimize image clarity.

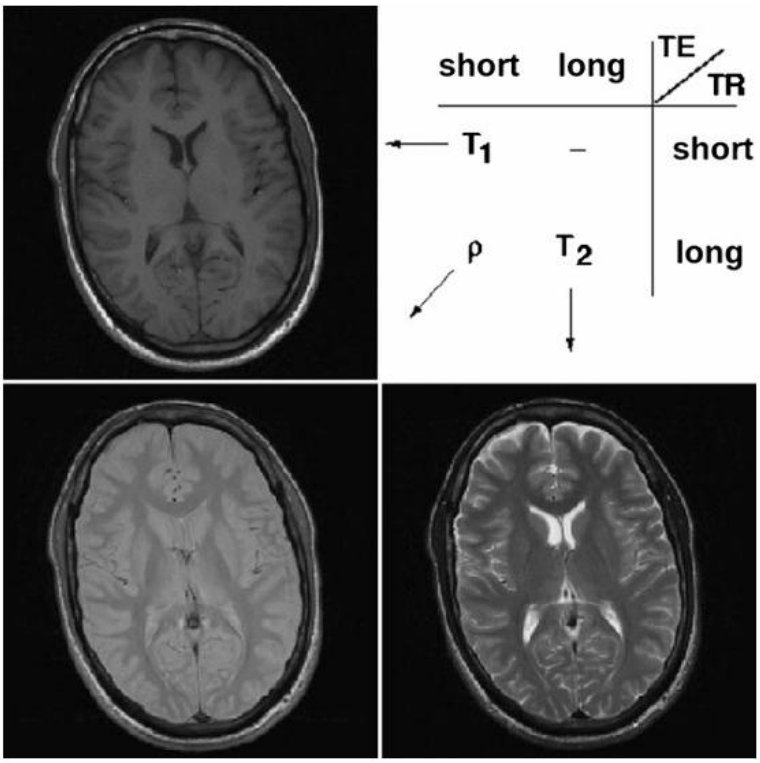

Figure 2.7: MR images of the same transaxial slice through the human brain acquired by weighting the acquisition for T_1 (longitudinal relaxation), T_2 (transverse relaxation), or ρ (proton density). The desired weighting is achieved by varying the echo time (TE) and repetition time (TR). (39)

In contrast, T_1-weighted imaging requires a short TE, below 25ms, which allows contrast to be governed by longitudinal relaxation. This is often accompanied by a short TR, below 200ms, to allow sufficient longitudinal magnetization recovery before the next excitation pulse.

A proton density-weighted image is generated when a long TR (greater than 2 seconds) and a short TE (less than 25 milliseconds) are applied. This type of image offers a high signal-to-noise ratio (SNR) but generally has lower contrast compared to T_1 and T_2-weighted images.

In addition to conventional weighting techniques, inversion recovery sequences are used to achieve specific contrast adjustments by modifying the inversion time (TI). A short TI (STIR) significantly reduces fat signal intensity, while a long TI suppresses signals from fluids such as cerebrospinal fluid (CSF) in fluid-attenuated inversion recovery (FLAIR) sequences which is widely used in brain imaging to darken CSF and enhance the visibility of other structures and pathological lesions.

2.1.5. Pulse Sequences

To obtain an FID signal, it's sufficient to send out a 90-degree pulse which triggers transverse net magnetization. Before sending out a different pulse, necessary in certain sequences, it's necessary to wait 3 to 5 times the longest T_1 of the sample called the repetition time (TR). The sequential use of 90-degree pulses is identified as saturation recovery (SR).

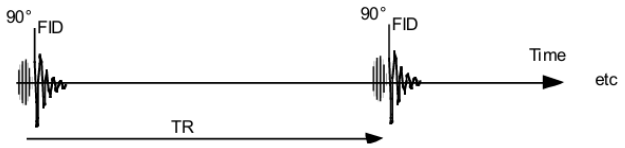

Figure 2.8: Schematic RF-pulse sequence for Saturation Recovery (SR). (42)

However, waiting for TR is not an optimal strategy when having to spatially encode the output signals or using a second signal to manipulate contrast across tissues. The pulse sequence can be finely controlled to obtain more informative scans by modifying RF and magnetic pulses, sampling intervals and time gaps between pulses.

One of the sequences is the definition of the spin echo method which relies on the application of two radiofrequency (RF) pulses: an initial 90° RF pulse (excitation pulse) followed by a 180° RF pulse (refocusing pulse). The first pulse rotates all spins moving the magnetization vector (M) into the transverse plane and rephasing them together. Once the RF pulse is turned off, the spins begin to precess and gradually lose phase coherence.

Then, a 180-degree pulse is applied at a time t=TE/2 after the application of the initial pulse which rotates the spins by 180° relative to their original positions refocusing the spins. After this, the spins remain in the transverse plane, but those with higher precessional frequencies ("faster" spins) shift behind those with lower precessional frequencies ("slower" spins). This phase accumulation causes by magnetic field inhomogeneities between $t = 0$ and t = TE/2 is corrected after the 180° RF pulse, leading to a rephasing effect at t = TE (echo time), which occurs TE/2 seconds after refocusing.

Since B_0 field inhomogeneities are static over time, they are cancelled out by this method. However, spin-spin interactions fluctuate over time, meaning that T_2 decay persists. The longer a spin echo takes to be acquired, the greater the effect of T_2 relaxation.

The 180° RF pulse can be applied repeatedly, producing multiple echoes of diminishing amplitude. This sequence, known as the Carr-Purcell-Meiboom-Gill (CPMG) train, consists of a repeated cycle: *90° – TE/2 – 180° – TE – 180° – TE – 180°* [Figure 2.9]. The echo time (*TE*) represents both the interval between consecutive 180° pulses and the time between successive echoes, which appear midway between RF pulses. Importantly, *TE* must always be shorter than T_2.

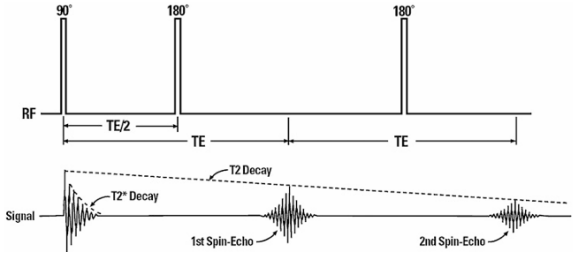

Figure 2.9: Carr-Purcell-Meiboom-Gill (CPMG) Train of pulses. (42)

Gradient echo (GRE) is another sequence that utilizes, rather than an RF pulse, a gradient pulse which is a controlled linear variation in magnetic field strength over a brief period of time.

In a GRE, an excitation pulse is applied, followed by two gradient pulses. The first gradient pulse is activated immediately after the excitation pulse, altering the local magnetic field strength as a function of spatial position. According to the Larmor equation, spins precess at different frequencies within this gradient field, leading to phase accumulation and a reduction in the observed signal. When the first gradient is turned off, a second gradient pulse of equal amplitude but opposite polarity is applied. Spins that were initially forced to precess at slower frequencies than those in the presence of B_0 now precess faster under the influence of the second gradient. Over time, this reverses the phase dispersion, leading to partial rephasing of the spins.

These two techniques modify contrast based on TE and TR, but another important parameter is TI which can be used in inversion recovery to get rid of undesired signals during imaging. This is done by sending a 180-degree pulse at time TI before the 90-degree excitation pulse making CSF or fat signal null. [Figure 2.10]

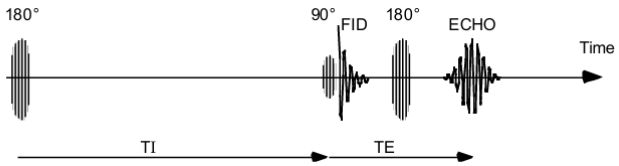

Figure 2.10: Schematic RF-pulse sequence for Inversion Recovery (IR). (42)

Acquiring images using conventional MRI pulse sequences can be highly time-consuming as even a TR of 1 second can lead to hours long acquisitions which are impractical for a clinical setting. To mitigate this issue, several strategies have been developed to accelerate MRI acquisition.

A compromise can be reached by reducing the number of data points, with the cost of having a lower resolution, or using multi-slice imaging, which allows simultaneous acquisition of data from multiple slices within the intervals between excitation pulses, capturing 16 or 32 slices at once by subjecting each slice to slightly different magnetic fields. The latter technique can substantially decrease total scan time to around 30 minutes.

To further accelerate imaging, the Turbo Spin Echo (TSE) method, which captures multiple spin echoes within a single pulse sequence, can be utilized reducing scan duration to around ten minutes or less. TSE is primarily used to generate T_2-weighted images, with contrast variations dependent on the echo time.

Another rapid imaging method is single-shot echo planar imaging (SS-EPI), which enables the capture of a complete image in a single RF excitation by alternating the direction of the x-gradient rapidly while short phase encoding gradients are applied in the other directions. Although SS-EPI is extremely fast and useful for functional MRI (fMRI), angiography and diffusion imaging, it presents technical challenges due to its complexity making multi-shot EPI a more stable alternative for routine MRI.

In recent years, the Magnetization-Prepared Rapid Gradient Echo (MPRAGE) sequence has become a widely adopted technique for obtaining high-resolution T_1-weighted images of the human brain, particularly in high-field MRI. This technique consists of three main phases: magnetization preparation which optimizes contrast, data acquisition utilizing a gradient-echo sequence with a short TR, and magnetization recovery allowing further contrast control.

A refined version of MPRAGE, known as MP2RAGE, further enhances image quality. This method begins with a 180° inversion pulse to prepare magnetization, followed by multiple gradient-echo acquisitions at a low flip angle [Figure 2.11]. After a delay, a second gradient-echo block is applied with a different flip angle, followed by another recovery period. This cycle is repeated to sample the space in three dimensions. The final image is generated by combining data acquired at different inversion times, leading to improved contrast and image clarity. (43)

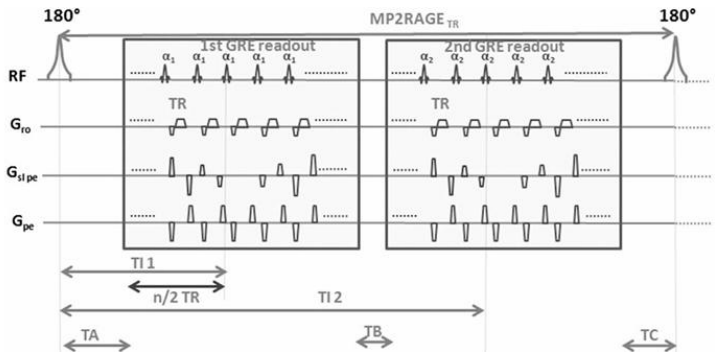

Figure 2.11: Schematic RF-pulse sequence for MP2RAGE (43).

2.2.Structural MRI

Structural MRI provides high-resolution images of the anatomical features of the brain, allowing for the assessment of the brain's spatial distribution and the detection of physical abnormalities such as atrophy or lesions. From such scans we can identify two types of brain tissue matter: white (WM) and grey (GM). The former consists mainly of myelinated axons while the latter includes neuronal cell bodies and glial cells. The presence of myelin is the relevant factor in MRI investigations as it affects contrast by decreasing T_1, T_2 and proton density by reducing the interaction between free water and macromolecules in its sheath (44).

For structural MRI, high-resolution T_1-weighted 3D sequences such as MPRAGE and MDEFT (Modified Driven Equilibrium Fourier Transform) are commonly used as these sequences are optimized to enhance contrast between grey matter, white matter, and cerebrospinal fluid, allowing for detailed anatomical visualization (43).

In these images, fat and WM exhibits high signal intensity, appearing white, whereas fluids and GM produce low signal intensity, appearing darker. Although T_1-weighted imaging effectively differentiates between white and grey matter, it is less useful for distinguishing cerebrospinal fluid from grey matter. This limitation makes it challenging to visualize fluid compartments such as the ventricles, the cerebral aqueduct, and the subarachnoid space[6].

Conversely, in T_2-weighted images, fluids generate high-intensity signals which makes for an excellent contrast between cerebrospinal fluid and brain tissue. More recently, fluid-attenuated inversion recovery (FLAIR) has been developed as a complement or even a potential replacement for conventional T_2-weighted imaging, particularly for detecting abnormalities in the presence of fluid compartments (45).

2.2.1. Extraction of GM Thickness

Particularly important in the study of neurodegenerative diseases is the ability to estimate cortical thicknesses and brain volumes to track atrophy. The extraction process is done by using FreeSurfer, a widely used open-sourced tool, and it involves several key steps, leveraging advanced image processing algorithms to accurately delineate and quantify cortical structures.

The processing of structural T_1-weighted MRI scans includes steps of normalization to a standardized atlas (Tailarach Atlas), removal of non-brain tissues, automatic segmentation of brain tissues, such as grey matter, white matter and cerebrospinal fluid (CSF), pial and white matter surface reconstruction, cortical thickness calculation and a final step of registration and parcellation.

The last step in particular is made to allow for intra- and inter-subject comparisons. Registration is the process of alignment of the image to a standard brain template which ensures that corresponding regions of different brains are aligned. Once this procedure is completed, the cortex is then subdivided into anatomical regions through a process called parcellation. FreeSurfer uses the Desikan-Killiany atlas to label regions enabling region-specific analysis of grey matter thickness.

An option in the processing of structural MRI scans in FreeSurfer is the use of a longitudinal processing pipeline which is specifically designed to enhance the analysis of brain changes over time, making it particularly useful for studying progressive changes in brain structure like the ones in PD (46). This pipeline offers several distinct advantages over cross-sectional processing, which only analyses individual time points independently, like enhancing the accuracy and sensitivity of detecting structural changes in the brain by leveraging the temporal relationship between multiple time points.

One of the key features of FreeSurfer's longitudinal processing is the creation of a subject-specific template generated by averaging the MRI data across all its time points. This is done by using a technique called inverse consistent registration which aligns and averages the images from different time points to form a common reference space which serves as a baseline for subsequent analysis, reducing variability which might be introduced by differences in image quality or misalignment between scans taken at different time points.

Each time point is then analysed in relation to the template leading to more reliable measurements of brain volumes and cortical thicknesses which is particularly beneficial in settings where following individual patients over time can reveal early signs of neurodegeneration.

2.3.Functional MRI

Functional MRI (fMRI) is used to detect regional time-dependent changes in brain metabolism, which may result from task-induced cognitive state changes or spontaneous resting-state processes. It manages to obtain this information while relying on the same MRI equipment as the one used for structural scans and being non-invasive.

An fMRI time series reflects the changes in the blood oxygen level-dependent (BOLD) signal, which is an evoked response resulting in a complex and nonlinear function arising due to neuronal activity changes in response to a stimulus or task. Neural activity in the brain requires energy in the form of adenosine triphosphate (ATP), which is primarily generated by mitochondria through the oxidative metabolism of glucose, which produces carbon dioxide as a byproduct. When a specific brain region is activated, increased neural activity raises the local energy demand, leading to an elevated cerebral metabolic rate of oxygen consumption in that area (47).

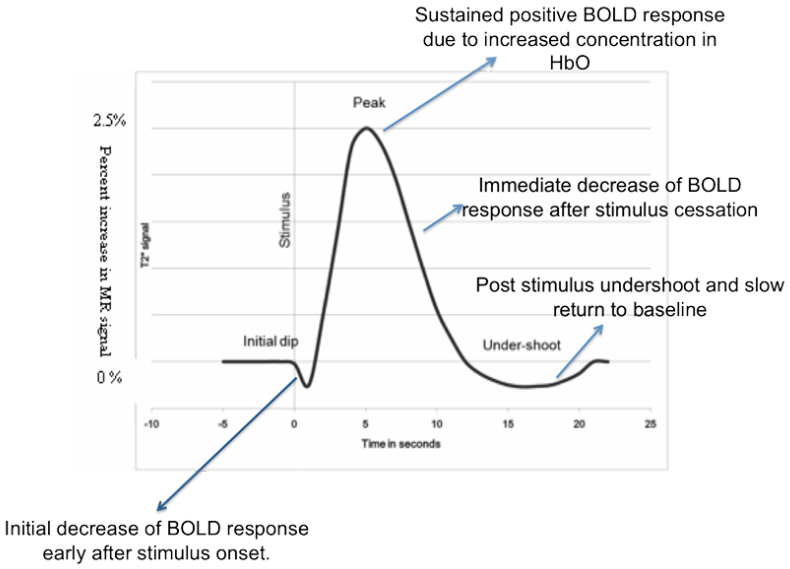

Figure 2.12: Typical BOLD response divided into three different regions: initial dip, peak, and post-stimulus undershoot. (48)

This process, known as the hemodynamic response, enhances regional cerebral blood flow and oxygen delivery. These changes alter the relative concentrations of oxyhaemoglobin (O_2Hb) and deoxyhaemoglobin (HHb), which can be detected using MRI due to their different magnetic susceptibilities. Unlike O_2Hb, which has minimal magnetic susceptibility differences compared to surrounding tissues or water, HHb is highly paramagnetic, causing significant slowing of the decay rate of the MRI signal, leading to an overall increase in signal strength which is generally small—around 1% or less—but can vary depending on the strength of the magnetic field. (49)

The temporal characteristics of neural activity as captured by fMRI, which reflect low-frequency fluctuations in the BOLD signal, differ significantly from those observed in neurophysiological studies that directly measure high-frequency neural firing. The BOLD signal typically begins about two seconds after neuronal activation, reaches its peak around 5–8 seconds after peak activity, and then drops below baseline in a phase known as the post-stimulus undershoot, which lasts approximately 10 seconds. This undershoot occurs because the reduction in blood flow outpaces the decline in blood volume, resulting in an increased concentration of

HHb in the activated brain regions. Additionally, a brief decrease in oxygenation can be observed shortly after neural activation, leading to an initial negative BOLD response, sometimes referred to as the "negative dip," within the first one to two seconds following stimulation. (48)

The fMRI signal is influenced by random noise and other factors arising from both the scanning hardware and the subjects. One particular source of noise is the thermal motion of electrons within both the subject and the scanner, which generating a random noise that is independent of experimental conditions that can be managed by averaging data across multiple acquisitions.

Another source of signal fluctuation is scanner drift, which results from instabilities in the MRI system and introduces slow, low-frequency variations in voxel intensity over time. Since this drift varies across different regions of the brain, it must be accounted for in fMRI analyses. Physiological noise, including subject movement, respiration, and heartbeat, also affects the fMRI signal by causing spatial and temporal fluctuations. While some of this noise can be modelled and corrected, periodic variations due to cardiac and respiratory cycles remain challenging to fully eliminate.

Despite its many advantages, fMRI has inherent limitations that affect its ability to measure brain activity coming from constraints on spatial and temporal resolution. Although MRI can achieve sub-millimeter anatomical resolution, acquiring such high-resolution functional images would take too long for practical use in fMRI. In typical fMRI studies, spatial resolution is approximately 3×3×5 mm, with image dimensions around 64×64×30 voxels, acquired within approximately 2 seconds.

Temporal resolution, which is dictated by the repetition time (TR) between image acquisitions, generally ranges from 0.5 to 4.0 seconds. While shorter TR values improve the ability to track rapid neural events, they often come at the expense of spatial resolution. Another significant challenge in fMRI research is making population-level inferences, as individual subjects have different brain sizes and anatomical variations. To compare data across participants, brain images are transformed onto a standard template which can introduce some degree of inaccuracy and blurring (50).

2.3.1. Resting-State Networks

Resting-state fMRI (rs-fMRI) captures brain activity in the absence of external stimuli or specific tasks, allowing researchers to examine neural activity during rest. This can be done by focusing on spontaneous low-frequency fluctuations in the BOLD signal. The concept of these fluctuations was first introduced by Biswal in 1995, who demonstrated synchronized activity between primary and higher-order somatosensory areas. (51)

Research has identified two opposing brain systems, commonly referred to as "task-positive" and "task-negative" (or "intrinsic" and "extrinsic") networks. Task-positive networks are engaged during cognitive tasks and goal-directed activities, such as processing external stimuli or executing tasks. In contrast, task-negative networks are more active when the brain is at rest or disengaged from external stimuli. An example of a task-negative network is the Default Mode Network (DMN), one of the primary resting-state networks which includes the medial prefrontal cortex and the posterior cingulate cortex, initially identified through PET studies and later confirmed using fMRI. (52)

2.4.MRI findings in PD Patients

2.4.1. Structural MRI findings

MRI has identified specific morphological and metabolic brain changes associated with PD which can also be used for the diagnosis of parkinsonian syndromes.

Structural MRI studies have reported notable changes in the frontal, parietal, and occipital lobes, particularly in advanced cases and patients with cognitive impairment (53). Additionally, distinct atrophy patterns have also been identified in early-stage PD (54). Other research also highlights thinning of the substantia nigra pars compacta, relatively less atrophy in the frontal cortex, and possible enlargement of the ventricles (55).

In newly diagnosed Parkinson's disease patients, significant grey matter atrophy or cortical thinning may not be evident at baseline compared to healthy controls although some longitudinal studies suggest that early-stage patients show initial cortical changes, with atrophy occurring primarily in the basal ganglia and progressive cortical thinning in the fronto-parietal and hippocampal regions over 1.5 to 3 years. On the other hand, middle-stage Parkinson's disease is more easily associated with initial cortical thinning, followed by widespread cortical atrophy while, in advanced stages, MRI can detect hyperintensities on T_2-weighted sequences and blurred boundaries of the red nucleus near the SN (54).

To detect SN changes, new techniques have been developed such as neuromelanin-sensitive T_1-weighted imaging and inversion recovery sequences, which take advantage of the paramagnetic properties of neuromelanin, which binds iron and increases signal intensity in neuromelanin-rich regions like the substantia nigra and locus coeruleus. They are emerging as valuable tools for early detection and monitoring disease progression (54).

Inversion recovery sequences, including T_2-FLAIR and Fast Inversion Recovery for Myelin Suppression, further enhance contrast by selectively suppressing certain tissue signals. Both sequences help detect atrophy in critical brain regions while also identifying ventricular enlargement and deep white matter hyperintensities, which could serve as additional PD markers for early diagnosis (55).

Recent developments in high-field (3.0 T) and ultra-high-field (7.0 T) MRI have shown promise in detecting abnormalities in the substantia nigra and nigrostriatal pathway. The improved signal-to-noise ratio at higher field strengths enhances anatomical detail, increases sensitivity to small lesions, and provides sharper grey-to-white matter contrast, resulting in clearer images and more precise visualization of brain (54).

A systematic review by Filippi et al. (2022) examined various neuroimaging studies focusing on GBA-associated parkinsonism. Specifically, certain longitudinal structural MRI studies reported that GBA-PD patients experience a more aggressive disease progression, characterized by greater cortical involvement and more significant atrophy in both grey and white matter regions. However, other studies failed to observe these differences suggesting that, while GBA mutations may contribute to distinct neurodegenerative patterns, further research is needed to clarify their impact. Nonetheless, incorporating genetic information into the clinical assessment and monitoring of PD patients remains essential (56).

2.4.2. Functional MRI findings

The brain is organized into several intrinsic functional networks that remain active even when the body is at rest, which can be picked up through rs-fMRI. These include the default mode network (DMN), sensorimotor network, executive control network, and others whose integrity can be analysed to evaluate disease progression (57). In PD, disruptions in these resting-state networks have been identified, providing insights into how the disease affects brain function beyond the motor symptoms (58).

Additionally, rs-fMRI enables the study of functional connectivity alterations through connectomics, providing valuable insights into how neurodegenerative diseases impact brain function. The next section explores this approach in greater detail.

3. Connectomics

Advanced imaging techniques have allowed for the analysis of brain networks through connectomics, by representing the brain as a connectome, a graph where each brain region serves as a node linked to others by connections or edges. One such graph is the structural connectome, derived from diffusion tensor imaging (DTI) or diffusion-weighted imaging (DWI), which reconstructs axonal pathways, reflecting the brain's physical network architecture, and is crucial for detecting disruptions seen in neurodegenerative processes.

In contrast, the functional connectome, extracted from rs-fMRI, is constructed based on temporal correlations between the BOLD signals of different brain regions. This connectome captures functional interactions rather than direct anatomical connections, providing information into how regions communicate dynamically. The analysis of this connectome has been particularly valuable in studying neurodegenerative diseases, as it can reveal early pathological changes, track disease progression, and serve as a potential biomarker for monitoring cognitive and motor impairments.

3.1.Functional Connectome (FC)

Recent studies have shown that PD patients exhibit reduced functional connectivity in motor-related regions such as the basal ganglia, thalamus, and motor cortex but also in networks related to cognition (59). These changes are thought to reflect the dysfunction of the dopaminergic pathways that are central to the motor control deficits in PD.

The analysis of FC also holds promise in identifying early-stage PD or individuals at risk for developing the disease especially in tandem with machine (60) and deep learning techniques (61) as rs-fMRI can detect subtle changes in brain connectivity even before evident motor and non-motor symptoms appear. It also plays a critical role in assessing the effects of therapeutic intervention by examining changes in FC pre- and post-treatment. For example, levodopa therapy, which temporarily restores dopamine levels, has been shown to affect the connectivity patterns in the primary motor cortex (62).

A study by Sezgin et al. (63) investigated FC in asymptomatic carriers of heterozygous GBA mutations and the researchers focused on the striatocortical circuitry, a network integral to motor and cognitive functions, revealing significant alterations in FC between the striatum and various cortical regions, including the prefrontal cortex and sensorimotor areas, when compared to non-carrier controls. These findings suggest that disruptions in striatocortical connectivity may occur prior to the onset of clinical symptoms in GBA mutation carriers, potentially serving as early biomarkers for PD.

In summary, the analysis of FC is instrumental in advancing the understanding of degenerative mechanisms of PD. The identification of key disruptions in brain networks not only offers new insights into disease progression but also aids in the identification of potential biomarkers for early diagnosis and evaluation of the impact of therapeutic interventions.

3.2.Graph Theory

One technique used for the identification of alterations is graph theory, which provides a mathematical framework for analysing brain networks which can be represented as graphs where nodes correspond to single brain regions and edges represent the structural or functional connections between them. These connections can be extracted through neuroimaging techniques such as fMRI for functional connectomes and diffusion tensor imaging (DTI) for structural connectomes (64).

The characterization of functional connectomes is carried out with measures of global and local properties. Global properties evaluate various aspects related to maximization of information flow along with minimization of resource costs (65). The first global property is functional segregation, which reflects the

network's ability to form specialized, highly efficient communities. The second, functional integration, provides insight into the efficiency of information flow across nodes. The third, small-worldness, characterizes the system's ability to balance high segregation with high integration, effectively merging the previous aspects. Lastly, network resilience represents the network's ability to recover from failure. In contrast, local properties rely on the characterization of hubs or nodes with central, highly relevant positions within the network which affect its topology. These are divided into connector and provincial hubs based on indexes of nodal centrality within the network, such as nodal degree, nodal strength, betweenness and eigenvector centrality.

The identification of such measures is useful for the identification of functional connectivity alterations within neurodegenerative diseases such as AD. Specifically researchers identified degeneration of brain hubs with the reduction of local and global measures consistent with disconnection phenomena previously identified in AD. The application was also extended to multiple sclerosis, another neurodegenerative disorder, in which measures of eigenvector centrality reported alterations consistent with clinical indexes of disability (66). In the context of PD, graph theory have identified significant differences in topological measures between PD patients and controls, particularly within the DMN and occipital lobes (67).

No applications in literature were identified for PD patients carrying GBA mutations spurning the interest for carrying out such analysis on FC coming from this subgroup.

3.3.Network Based Statistics (NBS)

Another statistical method for the analysis of complex brain networks is Network Based Statistics as introduced by Zalesky et al. (68). This approach identifies alterations in brain networks while avoiding challenges related to multiple comparison analysis which reduce statistical power by comparing results with null distributions.

This method relies on three steps: mass-univariate testing, component identification and significance assessment. Mass-univariate testing is performed by analysing each connection independently for differences across groups, component identification is used to identify connected subnetworks based on topological network adjacency and significance assessment is carried out through permutation testing to generate a null distribution whose components will be compared to the observed components to obtain statistically significant alterations.

The focus on interconnected networks allows for control over family-wise error rate, increasing the sensitivity to changes in FC. While this technique was introduced for spotting alteration in schizophrenia patients, the identification of FC alterations can be applied to neurodegenerative diseases.

In AD patients, several disconnected components were identified in regions connected to the DMN, an observation consistent with alterations identified with other techniques (69). In PD patients, NBS has been used to identify functional connectivity alterations distinguishing those eligible for DBS from those who are not. This approach highlights the potential of NBS as a highly sensitive tool for the early identification of DBS-eligible patients, aiding in more precise and timely treatment decisions. (70)

In summary, NBS's ability to grant a powerful statistic framework, while enhancing sensitivity even in multiple comparisons, make it suitable for the identification of differences across GBA carrier and non-carrier PD patients.

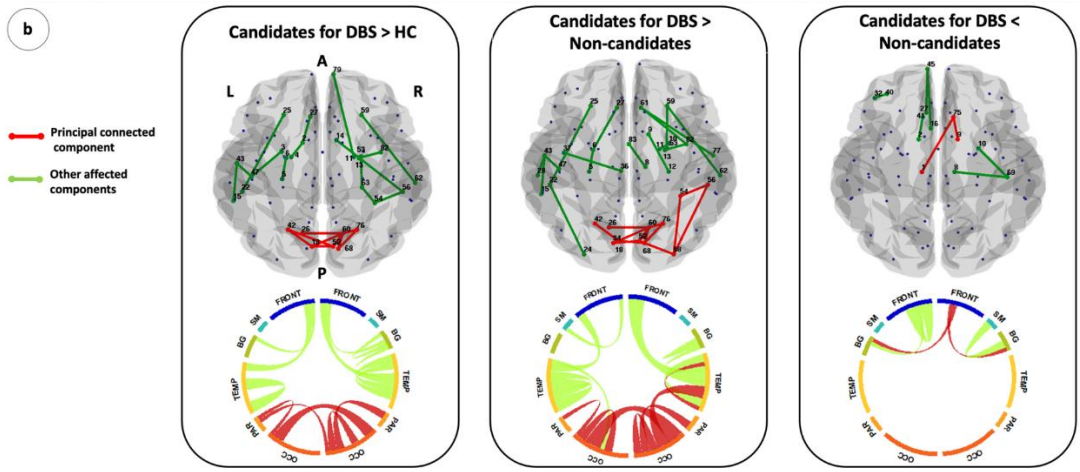

Figure 3.3: Regional analysis results obtained with NBS, from left to right: increased functional connectivity in candidates for DBS relative to controls; increased functional connectivity in Candidates for DBS relative to non-candidates; decreased functional connectivity in Candidates for DBS relative to non-candidates. (70)

3.4.Modelling Neurodegeneration

Neurodegenerative diseases are characterized by the progressive loss of neuronal function and cell death in specific brain regions, making their tracking and prediction crucial for understanding disease mechanisms. While significant progress has been made in identifying pathological hallmarks, such as the accumulation of misfolded proteins, the precise mechanisms underlying their spatial and temporal progression remain largely unknown.

In this regard, computational models have emerged as powerful tools for simulating disease progression, integrating biological, structural, and functional data to uncover underlying mechanisms. Various modelling approaches have been developed, each based on different hypotheses regarding how neurodegeneration spreads. The following sections will explore these diverse frameworks, examining their applications and potential for advancing future research.

3.4.1. Models Based on Local Gene Expression

Neurodegenerative diseases exhibit regionally selective vulnerability, with certain brain areas deteriorating earlier and more severely than others. Increasing evidence suggests that local gene expression patterns, particularly those related to synaptic maintenance, protein homeostasis, and immune responses, play a crucial role in shaping these atrophy patterns. To better understand how genetic susceptibility interacts with disease progression, recent modelling approaches have integrated transcriptomic data into agent-based frameworks.

One such approach leverages the Susceptible-Infected-Removed (SIR) model, originally designed for epidemiological studies, to describe neurodegenerative disease spread at the neuronal level. In this context:

- Susceptible (S) neurons belong to brain regions at risk of pathology,
- Infected (I) neurons are affected by disease-related misfolded proteins,
- Removed (R) neurons are permanently damaged or lost due to disease progression.

The model is governed by differential equations, where the rates of pathology spread, and neuronal loss can be adapted to be region-dependent and influenced by local gene expression patterns.

A study by Shafiei et al. (71) applied this approach to behavioural variant frontotemporal dementia (bvFTD), demonstrating that regional gene expression of disease-relevant genes, such as C9orf72 and TARDBP,

significantly contributes to local vulnerability. Their model, incorporating gene expression maps alongside structural and functional connectivity data from healthy controls, successfully predicted the spatiotemporal distribution of atrophy. This emphasizes the importance of integrating molecular factors alongside network connectivity in disease modelling.

Similarly, Abdelgawad et al. (72) applied an SIR model to longitudinal data from PD patients. In this case, pathology spread was modulated by structural connectivity and by the expression of genes GBA and SNCA, both implicated in PD. The model achieved significant correlations between simulated and actual atrophy patterns over the first two time points, demonstrating the potential of transcriptomic-informed models in predicting neurodegeneration dynamics.

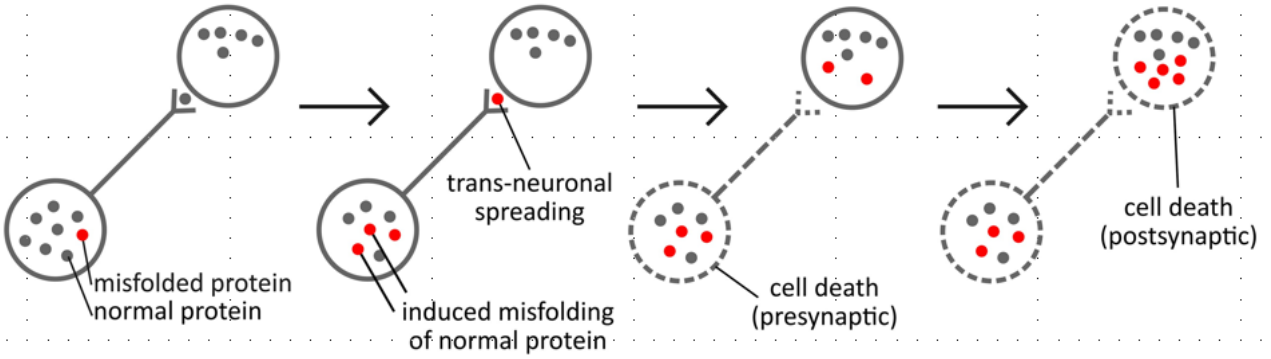

Figure 3.4.1: Simulation of pathology spread through a SIR model. Proteins propagate via the structural connections between brain regions and induce atrophy, both pre- and post-synaptically. (71)

3.4.2. Machine and Deep Learning Models

Recent advancements in computational modelling for neurodegenerative diseases have increasingly incorporated machine learning and deep learning techniques to enhance predictive accuracy and uncover complex disease mechanisms.

The first approach by Zhang et al. (73) leverages Physics-Informed Neural Networks (PINNs) to enforce generic physical models while using symbolic regression to discover the underlying reaction-diffusion equations governing tau propagation. By integrating clinical imaging data, the model optimizes parameters of the reaction function, allowing for patient-specific predictions of disease progression. The system of differential equations incorporates brain connectivity data, ensuring that the diffusion process aligns with known anatomical pathways of neurodegeneration. While this approach shows promise in observing long-term tau concentrations, the data presented by the study is limited to short-term casting doubts on the predictive powers of such model.

The study by Young et al. (74) focuses on FTD, examining how different MAPT mutations influence clinical features and atrophy patterns analysed by an unsupervised machine learning technique. The Subtype and Stage Inference (SuStaIn) algorithm is trained on longitudinal clinical and imaging data to identify distinct atrophy trajectories associated with specific mutations linking genotype to phenotype and providing insights into how tau pathology leads to region-specific neurodegeneration.

In another study, Sanz Perl et al. (75) applied a deep-learning whole-brain perturbational modelling approach to investigate how neurodegenerative diseases alter brain connectivity in patients diagnosed with Alzheimer's disease and behavioural variant frontotemporal dementia. By introducing perturbations, they identified critical regions and pathways involved in disease progression, providing insights into potential therapeutic targets.

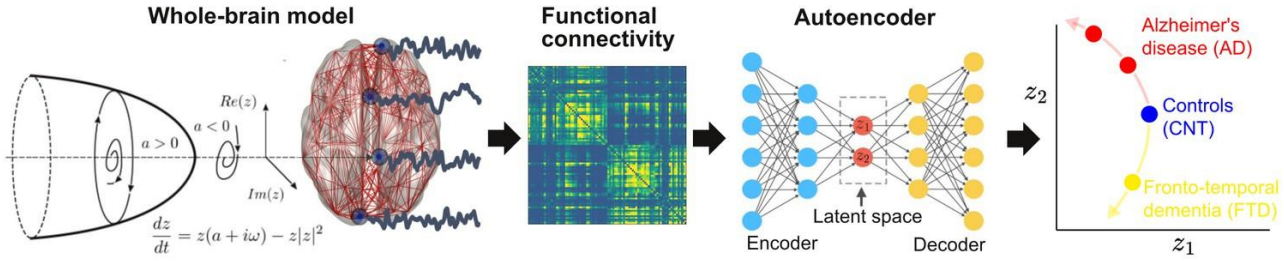

Figure 3.4.2. Methodological outline of whole-brain perturbational modelling through a deep-learning approach (75).

3.4.3. Computational Models based on Network Based Diffusion

Network-based diffusion models have become instrumental in understanding the progression of neurodegenerative diseases by simulating how pathological agents, such as misfolded proteins, propagate through the brain's structural connectivity network, offering insights into disease dynamics and potential therapeutic targets.

Chen et al. (76) developed a mathematical framework to study tau pathology spread in Alzheimer's disease and related disorders. Their model comprises a system of partial differential equations addressing two primary propagation pathways: Intracellular Diffusion, where tau spreads through synaptic connections or nanotubes crossing adjacent neurons, and extracellular diffusion, where secreted protein diffuses through interstitial fluid and is taken up by neighbouring cells. Numerical simulations revealed that intracellular diffusion aligns with the gradual progression observed in clinical Alzheimer's cases emphasizing the significance of cross-membrane tau transport and extracellular clearance in maintaining neuronal health.

Tora et al. (77) introduced a Network Transport Model (NTM) to capture the directional spread of tau proteins in Alzheimer's disease. Unlike traditional diffusion models, the NTM incorporates active transport mechanisms along axonal pathways, accounting for the observed directional bias in tau propagation. This model, parameterized by microscopic processes such as aggregation and transport rates, provides a comprehensive framework linking molecular dynamics to macroscopic disease progression.

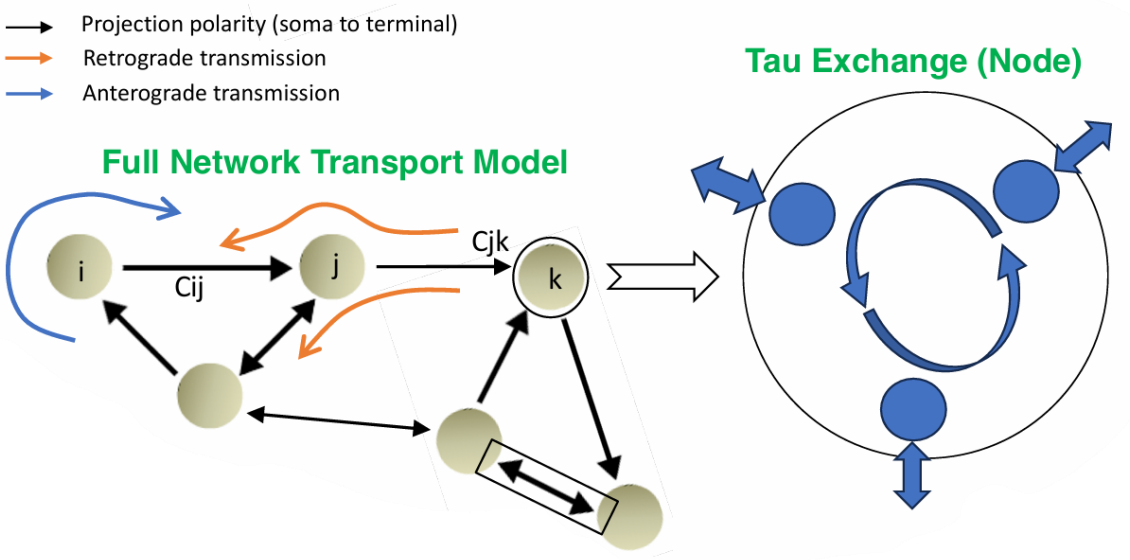

Figure 3.4.3. Illustration of NTM in which brain regions are represented by nodes and white matter fibre projections between them by edges. Tau pathology propagates through active diffusion in an anterograde or retrograde direction, depending on the cell polarity and the solubility of tau (77).

3.4.4. Network Diffusion Models (NDM)

The NDM has emerged as a pivotal tool in elucidating the progression of neurodegenerative diseases. By simulating the transneuronal spread of pathological proteins along the brain's structural connectivity, this model offers insights into disease dynamics across various prion-like diseases.

Raj et al. (78) first introduced the NDM to investigate disease propagation in AD and behavioural variant Frontotemporal Dementia (bvFTD). Utilizing diffusion MRI data from healthy individuals, they constructed the structural connectivity network to model how misfolded proteins disseminate along neuronal pathways. The model's predictions closely mirrored observed atrophy patterns in AD and bvFTD patients, supporting the hypothesis that neurodegenerative diseases spread through the brain's network architecture.

Expanding upon this framework, Pandya et al. (79) tailored the NDM to PD by focusing on the propagation of misfolded alpha-synuclein proteins. By integrating structural connectivity data, the model simulated the spread of pathology originating from randomized seed regions. The simulations accurately reflected the spatial and temporal progression of PD, aligning with known neuropathological stages. Notably, the model identified the substantia nigra as the most probable seed region, reinforcing its central role in PD pathogenesis. This study underscored the utility of the NDM in predicting disease trajectories and highlighted their potential in refining diagnostic and therapeutic strategies.

Another application of NDM was carried out by Bhattarai et al. (80) to predict neurodegeneration patterns in patients with limb-onset ALS. By utilizing structural MRI data, the model simulated the spread of pathology through the brain's connectome. Findings indicated that the NDM could accurately replicate both the severity and progression of neurodegeneration observed in these patients, highlighting its potential as a predictive tool for ALS progression.

Collectively, these studies demonstrate the versatility and robustness of the NDM in capturing the complex dynamics of neurodegenerative disease progression. By leveraging the brain's structural connectivity, NDM provides a unified framework to simulate the dissemination of pathological prion-like proteins, offering valuable insights into disease mechanisms and potential therapeutic targets across various neurodegenerative conditions.

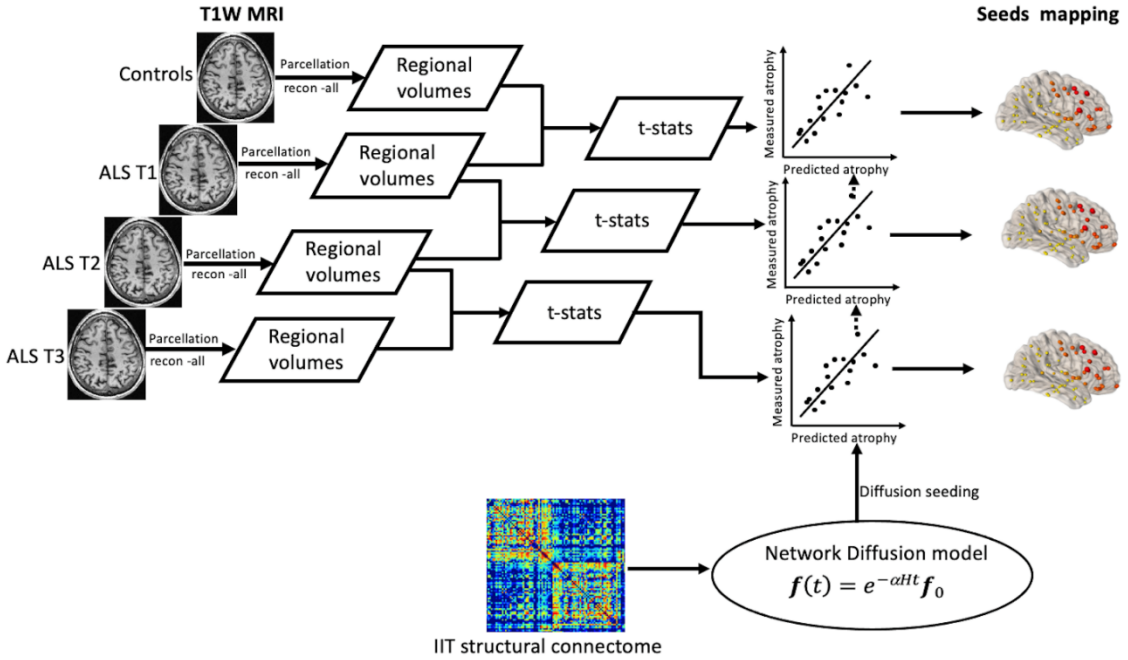

Figure 3.4.4. Application of the NDM for ALS in which model output is related to measured atrophy to predict neurodegeneration. (80)

3.4.5. Models Simulating Aggregation

While models based on diffusion alone show promising results, they can be expanded by considering protein aggregation phenomena which play a crucial role in the progression of neurodegenerative diseases. Recently, a growing number of computational approaches have started to integrate such concepts to more accurately model disease mechanisms.

Lindstrom et al. (81) developed an aggregation-based model to explore the molecular origins of Alzheimer's disease, focusing on the formation and accumulation of amyloid-beta monomers into dimers and trimers. By emphasizing the role of reaction kinetics in driving protein aggregation, the model simulates the transition from monomeric species to toxic species such as oligomers and fibril formations. The model replicates the rapid increase in AD incidence with age by incorporating age-related changes in protein dynamics while providing a quantitative framework for understanding how molecular interactions contribute to disease progression.

Brennan et al. (82) introduced a model integrating network-based diffusion with protein aggregation kinetics to study the dynamics and treatment of AD. This approach captures the spread of misfolded proteins across the structural connectome while incorporating the processes of nucleation, elongation, and fragmentation of aggregates. By simulating disease progression within a network framework, the model offers a powerful tool for predicting atrophy patterns and evaluating potential therapeutic interventions targeting specific brain regions or molecular pathways.

3.4.6. Aggregation-Network-Diffusion (AND) Model

Raj et al. (83) developed a mathematical model that integrates protein aggregation kinetics with network diffusion to simulate tau propagation in AD. The AND model describes mathematically the biophysical mechanisms underlying misfolded protein production, aggregation, and diffusion across the brain's structural connectivity. The following section provides a detailed analysis of the model's mechanics, laying the groundwork for its adaptation to α-Syn propagation in PD in the methods section.

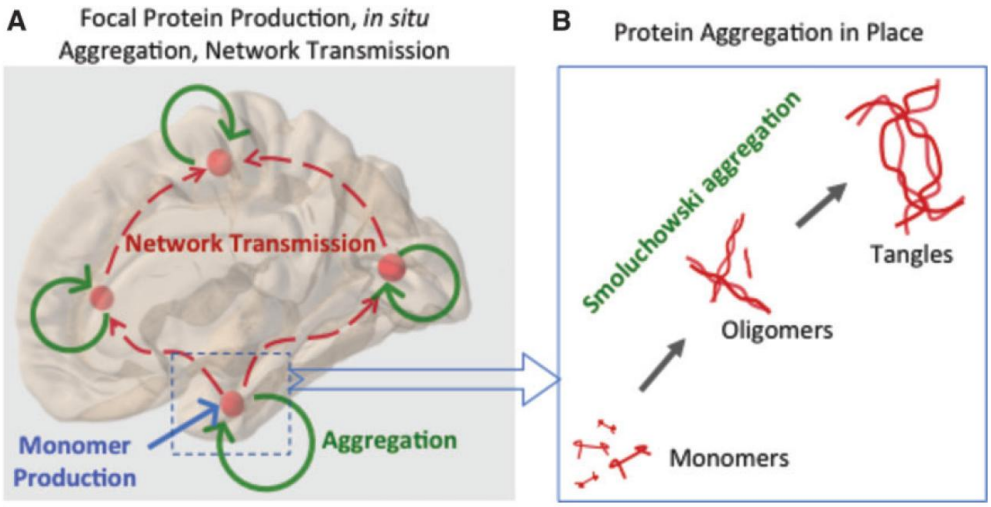

Figure 3.4.6.1 Illustration of the mechanisms of monomer production, aggregation and network transmission (left) with a focus on Smoluchowski aggregation from monomers to tangles (right). (83)

3.4.6.1.Smoluchowski Aggregation

The aggregation process follows a system of infinite discrete differential equations first described by Smoluchowski in 1917 to model the rapid coagulation of aerosols. This theory is based on pairwise coagulation, making it applicable to various fields that require modelling the evolution of diffusing particle densities, such as polymerization, biological populations, and fuel mixtures. More recently, Smoluchowski's equations have been used to describe the aggregation of Aβ amyloid (84) and τ-polymers (85). The established parallels between these proteins and α-Syn in the context of prion-like propagation provide the foundation for applying this theory to α-Syn aggregation in PD.

The theory offers characterization of the behaviour of polymers of length k (P_k) as sets of k identical monomers which are free to move within a medium. This approximation is made in the context of aggregation phenomena within brain regions, diffusion is mediated through implementation of network-based diffusion in the following section. The aggregation is described in through a probability that two monomers or oligomers might approach each other and merge into bigger oligomers of size equal to the sum of the lengths of the original species. Admitting only binary reactions, the coalescence process is described through:

$$P_k + P_j \rightarrow P_{k+j}$$

for the two polymers of size k and j. To characterize this process, the assumption of Brownian diffusion is made and the concentration of polymer P_m of size $m \in [1, M]$ being $u_m(x,t)$ at a spatial location x at time t. The discrete diffusive coagulation of the polymer follows this reaction-diffusion equation:

$$Q_m(u) = \frac{\partial\, \mathrm{u_m(x,t)}}{\partial\, \mathrm{t}} - \mathrm{d_m}\, \Delta_{\mathrm{x}}\, \mathrm{u_m(x,t)}$$

Where net gain of polymer (Q_m) is result of the subtraction between increments over time of concentration and the diffusion of said polymer mediated through diffusion coefficient d_m over space variations of Δ_x.

The net gain can be further expressed as being as the subtraction between gain ($Q_{g,m}(u)$) and loss ($Q_{l,m}(u)$) of polymer due to aggregation phenomena in the following way:

$$Q_m(u) = Q_{g,m}(u) - Q_{l,m}(u)$$

$$with \quad \begin{cases} Q_{g,m}(u) = \frac{1}{2}\sum_{j=1}^{m-1} a_{m-j,j}\ u_{m-j}\, u_j \\ Q_{l,m}(u) = u_m \sum_{j=1}^{\infty} a_{m,j}\ u_j \end{cases}$$

where, $a_{m,j}$ represents the kinetic coagulation rate, which defines the reaction leading to the formation of a polymer of length $m + j$ from polymers of sizes m and i.

The gain term accounts for the aggregation of smaller polymers into a polymer of size m, while the loss term represents the depletion of polymers of size m as they aggregate into larger polymers. Since polymer aggregation has no intrinsic upper bound, polymers can theoretically grow indefinitely. Merging the equations together to obtain an ordinary differential equation for the aggregation process:

$$\frac{\partial\, u_m(x,t)}{\partial\, t} = d_m\, \Delta_x\, u_m(x,t) + \frac{1}{2}\sum_{j=1}^{m-1} a_{m-j,j} u_{m-j}\, u_j - u_m \sum_{j=1}^{\infty} a_{m,j} u_j$$

3.4.6.2.Network Diffusion

The postproduction transmission of prion-like proteins through neural pathways is modelled through the implementation of the aforementioned NDM, initially ideated for τ propagation (78), which has found successful implementation in α-Syn progression in PD (79) and in the spread of FTD (86). The NDM relies on propagation of pathological proteins through the brain network following this graph diffusion term:

$$\frac{\partial u_m(v,t)}{\partial t} = -d_m \Delta_\Gamma u_m(v,t)$$

Where Δ_Γ is the positive weighted Laplacian associated with the graph Γ, which in our case if the functional connectivity matrix, and is defined as:

$$\Delta_\Gamma = I - D^{-\frac{1}{2}} C D^{-\frac{1}{2}}$$

Where C is the functional connectivity matrix, D is the diagonal matrix of node degree, and I is the identity matrix. This formulation of the Laplacian allows for enforcement of row and column normalization, making the model insensitive to variance in region size and node degree (87). Effectively this formulation replaces the diffusive term, which was previously reliant on Brownian motion only, with one that reflects the complexity of the brain network and its preferential routes for pathology spread.

3.4.6.3.Misfolded Monomer Production

The last component of this model is the generation of misfolded monomers of the protein driving the disease which happens only in one region, i.e. the seed region. Production is therefore modelled as an additive term which only comes in play for the monomer equations following a gamma shaped function:

$$f_{\tau}(v_i, t) = \begin{cases} \frac{t}{\sigma_f} exp(-\frac{t}{\sigma_f}) & , \quad v_i = v_{seed} \\ 0 & , \quad \text{otherwise} \end{cases}$$

Where v is the vector identifying the single regions, v_{seed} is the seed region fixed as the entorhinal cortex, and σ_f is the support of the gamma function fitted to the potential duration of the disease, set to 25 years arbitrarily.

3.4.6.4.Aggregation and Diffusion Rate

Aggregation and diffusion rates were defined to ensure a reduction of transmission that would decrease as oligomer length increased. This scaling behaviour was set to fit empirical *in vitro* data on amyloids through a gamma-shaped expression (88):

$$a_{m,j} = \frac{mj}{\sigma_{agg}^2} exp\left(-\frac{mj}{\sigma_{agg}^2}\right) \qquad and \qquad d_m = \frac{m}{\sigma_{diff}} exp\left(-\frac{m}{\sigma_{diff}}\right)$$

where σ_{agg} and σ_{diff} are scaling constants arbitrarily set to values of two and one respectively.

3.4.6.5.Complete AND Model

While the mathematical implementation calls for the modelling of an infinite number of polymers of different length, a feasible approach calls for the use of some simplifications. First is the upper bound on the polymer length which is set to the last τ form observed in literature of τ tangles, second is the grouping of polymers of similar lengths into 5 protein forms: monomers (m = 1), small oligomers (m = 2), large oligomers (m =3), protofibrils (m = 4) and tangles (m = M = 5). This effectively limits the amount of ordinary differential equations to 5 expressed in the following way:

$$\begin{cases} \frac{\partial \tau_1(v,t)}{\partial t} = -\beta d_1 \Delta_{\Gamma} \tau_1(v,t) - c_1 \tau_1(v,t) + \sum_{j=1}^{M} a_{1j} \tau_j(v,t) + c_2 f_{\tau}(v,t) \,, & for\ m = 1 \\ \frac{\partial \tau_m(v,t)}{\partial t} = -\beta d_m \Delta_{\Gamma} \tau_m(v,t) + c_1 \left[\frac{1}{2} \sum_{j=1}^{m-1} a_{j,m-j} \tau_j(v,t) \tau_{m-j}(v,t) - \tau_m(v,t) \sum_{j=1}^{M} a_{m,j} \tau_j(v,t) \right], & for\ 2 \geq m \geq 4 \\ \frac{\partial \tau_M(v,t)}{\partial t} = \frac{c_1}{2} \sum_{j+k \geq M;\ k,j<M} a_{j,k} \tau_j(v,t) \tau_k(v,t) \,, & for\ m = M = 5 \end{cases}$$

3.4.6.6.Results

The evaluation of the model's results was based on correlations with three types of empirical data. First, atrophy patterns observed in MRI scans were compared to tangle concentrations, yielding significant correlations. Second, tangle concentrations were validated against tau-PET imaging data, confirming the model's accuracy in capturing regional tau distributions. Third, CSF phosphorylated tau levels were assessed by comparing them to the sum of protein concentrations, weighted by their diffusivity rate, providing a biochemical validation of the model's predictions.

These results suggests that a similar framework could be used to model α-Syn spread and validate it against observed neurodegeneration in PD, providing a quantitative tool for studying disease progression.

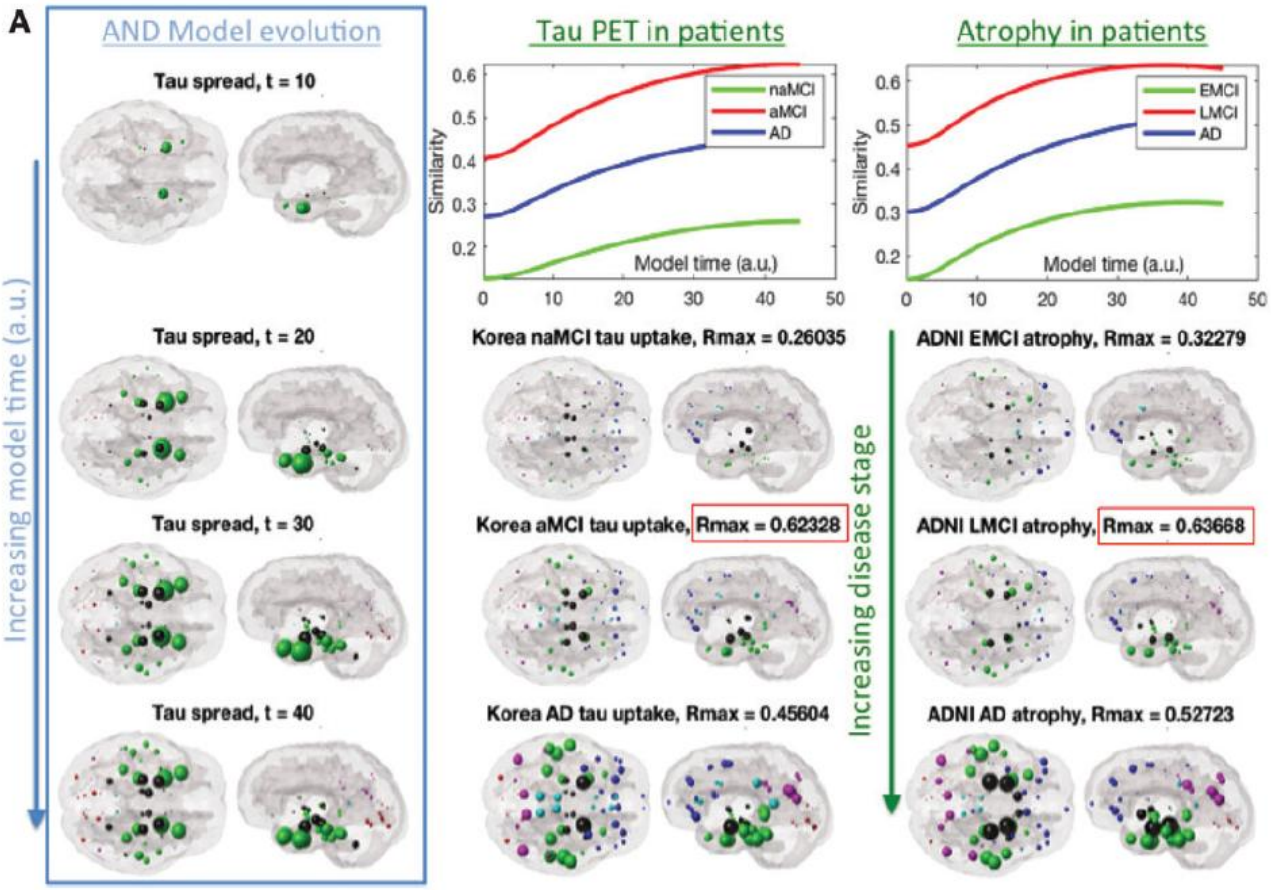

Figure 3.4.6.2. Glass brain rendering of the AND Model evolution in terms of τ burden (left) and its comparison to regional Flortaucipir-PET scans (middle) and regional atrophy (right). (83)

4. Materials and Methods

4.1.Subjects

A total of a hundred and fifty-four patients diagnosed with PD with H&Y under or equal to 4 were prospectively recruited from the Movement Disorders Department of the Neurology Clinic, Clinical Center of Serbia, as part of an ongoing longitudinal study. All participants met the UK Parkinson's Disease Society Brain Bank diagnostic criteria (89). At the time of enrolment, the cohort included both treatment-naïve patients and those receiving stable dopaminergic therapy. Patients underwent assessments at baseline and were re-evaluated annually or biennially for a minimum of two and up to five follow-up visits within a seven-year observational period. Exclusion criteria included moderate to severe resting head tremor, dementia at study entry based on the Movement Disorder Society (MDS) diagnostic criteria for PD dementia (Emre et al., 2007), cerebrovascular disease, intracranial masses detected on routine MRI, a history of traumatic brain injury, or any other significant neurological or medical conditions.

At baseline, all patients underwent genetic screening to identify GBA mutations. Among the 154 PD patients, 13 were found to carry a GBA mutation (GBA-positive). From the remaining PD non-carriers (GBA-negative) patients, 39 individuals were selected to match the GBA-positive group based on age, age at onset, sex, education, and disease severity as measured by the UPDRS-III total score. Additionally, 60 healthy controls, matched for age, sex and education, free from any neurological, psychiatric, or major medical conditions, were recruited from non-consanguineous relatives, institute personnel, and word-of-mouth referrals. Healthy controls underwent clinical, cognitive/behavioural, and MRI assessments only at baseline. The demographic characteristics of the study cohort are summarized in Table 4.1. All participants provided written informed consent prior to enrolment.

Variables	HC	PD GBA-Positive	PD GBA-Negative	p: HC vs PD GBA-positive	p: HC vs PD GBA-negative	p: PD GBA-positive vs PD GBA-negative
N	60	13	39			
Age [years]	61.96 ± 9.34 (46.14-77.72)	62.37 ± 4.32 (54.45-67.93)	61.98 ± 7.02 (43.05-75.86)	1.00	1.00	1.00
Sex [man/ woman]	16 (41.00)/ 23 (59.00)	5 (38.46)/ 8 (61.54)	19 (48.72)/ 20 (51.28)	0.87	0.49	0.52
Education [years]	13.17 ± 2.49 (8.00-16.00)	12.53 ± 2.87 (8.00-17.00)	13.17 ± 2.63 (8.00-20.00)	1.00	1.00	1.00
Age at onset [years]	-	58.15 ± 5.58 (49.00-66.00)	58.95 ± 7.89 (40.00-74.00)	-	-	0.53
Disease duration [years]	-	4.21 ± 3.92 (1.35-13.37)	3.03 ± 3.99 (0.11-22.49)	-	-	0.53
UPDRS-III total	-	22.38 ± 15.44 (5.00-59.00)	18.07 ± 8.91 (7.00-51.00)	-	-	0.23
Hoehn & Yahr	-	1.42 ± 0.67 (1.00-3.00)	1.15 ± 0.52 (1.00-4.00)	-	-	0.18

Table 4.1: Demographic characteristics of the cohort: values are reported as mean ± standard deviation (range) or absolute and percentage frequency (%) for continuous and categorical variables, respectively. Differences between Parkinson's Disease (PD) patients and healthy controls (HC) and between PD patients carrying GBA mutation (GBA-positive) and PD non-carrier patients (GBA-negative) were assessed using one-way ANOVA (for continuous demographic and general clinical variables) and Chi squared test (for all categorical variables). P-values were adjusted for multiple comparisons.

The distribution of baseline and follow-up assessments of the selected cohort is reported in Table 4.2.

Group	Baseline	Follow-up Visit				
		1 Year	2 Years	3 Years	5 Years	7 Years
PD GBA-positive	39	39	38	34	30	21
PD GBA-negative	13	13	12	9	6	5

Table 4.2: Availability of evaluations for PD patients.

4.1.1. Clinical Evaluation

At baseline and each follow-up visit, an experienced neurologist conducted clinical. Patients were examined in ON state (i.e., period when the dopaminergic medication is working and symptoms are well controlled). Demographic and general clinical data, including sex, education, age, age at onset, and disease duration, were collected using a semi-structured interview. Disease severity was assessed using the HY stage and UPDRS-III.

4.1.2. Genetic Screening

Sequence analysis of exons 8–11 of the GBA gene was performed. Primers used for the amplification of exons 8 and 9 were specific to the functional GBA gene, avoiding co-amplification of its pseudogene (GBAP). Exons 10 and 11 were amplified using a nested PCR approach with partially mismatched primers to

prevent interference from GBAP. Subjects carrying the D409H mutation were additionally sequenced for the H255Q variant.

4.1.3. Neuropsychological and Behavioural Evaluations

Neuropsychological and behavioural assessments were conducted at baseline and each follow-up visit, within 48 hours of MRI acquisition. Healthy controls underwent the same test battery at baseline only. Assessments were administered by trained neuropsychologists who were blinded to the clinical data, GBA status, and MRI results. All neuropsychological and behavioural variables were measured at each time point.

The neuropsychological assessment included global cognition assessed with the Mini-Mental State Examination (MMSE) and the Addenbrooke's Cognitive Examination-Revised (ACE-R). Memory was evaluated using the Rey Auditory Verbal Learning Test, the Pattern Recognition Memory (PRM) tests from the Cambridge Neuropsychological Test Automated Battery (CANTAB), and the Digit Span forward. Executive function was assessed with the Digit Span backward, the Clock Drawing Test, the Intra/Extra Dimensional Set Shift test from CANTAB, and the Stroop color-word test. Attention and working memory were measured using the Trail Making Test, the Digit Ordering Test, and the Letter Cancellation Test. Language abilities were examined with the Boston Naming Test and the language subtest of ACE-R. Fluency was assessed through semantic and phonemic fluency tests. Visuospatial abilities were evaluated using the Hooper Visual Organization Test and the visuospatial subtest of ACE-R. Mood was assessed with the Hamilton Depression Rating Scale, the Hamilton Anxiety Rating Scale, the Beck Depression Inventory (BDI), and the Apathy Evaluation Scale.

4.2. MRI Acquisition

Brain MRI scans were acquired at each time point using a 1.5 T Philips Achieva scanner at the Clinic of Neurology in Belgrade, Serbia. The imaging protocol included three MRI sequences.

First, a dual-echo (DE) turbo spin-echo (SE) sequence (TR = 3125 ms, TE = 20/100 ms, echo train length = 6, in-plane sensitivity encoding parallel reduction factor = 1.5) was used to acquire 44 axial slices with a slice thickness of 3 mm. The field of view (FOV) was 240 × 232 mm², resulting in a voxel size of 0.94 × 0.94 × 3 mm.

Second, a high-resolution 3D sagittal T1-weighted Turbo Field Echo (TFE) sequence (frequency direction = anterior-posterior, TR = 7.1 ms, TE = 3.3 ms, inversion time = 1000 ms, flip angle = 8°, out-of-plane SENSE parallel reduction factor= 1.5, sagittal orientation) was acquired with an FOV of 256 × 256 mm², yielding a voxel size of 1 × 1 × 1 mm.

Third, for resting-state functional MRI (rs-fMRI), a gradient-echo planar imaging sequence was used (TR = 3000 ms, TE = 35 ms, flip angle = 90°). The acquisition covered an FOV of 240 × 240 mm² with a slice thickness of 4 mm, generating 200 volumes consisting of 30 contiguous axial slices. During rs-fMRI acquisition, subjects were instructed to remain motionless with their eyes closed while not thinking about anything.

4.3.MRI Analysis

4.3.1. Brain Parcellation

4.3.1.1.Cortical Thickness Measurement

To estimate cortical atrophy, cortical reconstruction and cortical thickness estimation were performed using the FreeSurfer image analysis suite, version 5.3 (90). Contrast between grey matter (GM) and white matter (WM) was enhanced by nulling image values below the mean cerebrospinal fluid (CSF) intensity and rescaling intensities above this threshold. Following registration to Talairach space and intensity normalization, an automatic skull stripping procedure was applied to remove extra-cerebral structures, including the cerebellum and brainstem. All images were manually inspected for skull stripping errors to ensure segmentation accuracy.

Subsequently, images were segmented into GM, WM, and CSF, with cerebral hemispheres separated and subcortical structures delineated from cortical components. The WM/GM boundary was tessellated, and the surface was deformed along intensity gradients to optimally delineate WM/GM and GM/CSF borders, producing the WM and pial surfaces. The cortical surface was then inflated and registered to a spherical atlas, and the cerebral cortex was parcellated into 34 regions per hemisphere based on gyral and sulcal structures, following the Desikan et al. atlas (91). Cortical thickness was computed as the mean shortest distance between the WM boundary and the pial surface.

For longitudinal analysis of cortical changes in PD patients, T_1-weighted images from each subject across multiple time points were processed using FreeSurfer's longitudinal processing pipeline. This approach generated an unbiased within-subject template from the T_1-weighted scans through a robust, inverse consistent registration.

Several image processing steps, including skull stripping, Talairach transformation, and atlas registration, were initialized using a single-subject template to enhance consistency and statistical power compared to the standard cross-sectional FreeSurfer pipeline, as previously described. Individual surface maps from all timepoints were aligned to a common average surface and smoothed using a Gaussian kernel with a full width at half maximum (FWHM) of 10 mm. This procedure resulted in 68 cortical thickness measures per subject per scan.

4.3.1.2. Gray matter volumetry

Grey matter volumetry was extracted by employing FMRIB's Integrated Registration and Segmentation Tool (FIRST) in FSL (92) to automatically segment GM regions. These regions included the brainstem along with 7 regions per hemisphere: caudate, pallidum, putamen, thalamus, nucleus accumbens, amygdala and hippocampus. A total of 15 mean GM volumes were extracted and further multiplied by a volume scaling normalization factor derived from a SIENAx analysis (93) accounting for the differences in head size across subjects.

4.3.1.3. Cortical Thickness and GM Volumetry Normalization

Once all cortical thickness and subcortical volume data were extracted, extreme outlier detection was performed. Values that deviated by more than three standard deviations from the mean at each time point were flagged. Further manual inspection confirmed that these outliers resulted from segmentation inaccuracies, and they were excluded from subsequent analyses by setting them as not a number.

To facilitate between-subject comparisons, all cortical thickness and volume values were normalized using baseline data from healthy controls. Regional values were converted into atrophy z-scores based on the following formula:

$$A_{PD} = \frac{x_{PD} - \overline{x_{HC}}}{\sqrt{\frac{\sigma_{HC}^2}{n_{HC}}}}$$

where A_{PD} represents the z-scored regional atrophy value for each region, for each patient at each time point; x_{PD} is the regional cortical thickness or subcortical volume of the PD patient; $\overline{x_{HC}}$ is the average regional value from the 60 healthy controls; σ_{HC} is the standard deviation of the control group's regional values; and n_{HC} is the number of healthy controls.

4.3.2. Functional Connectivity

Rs-fMRI Preprocessing

The first step in Rs-fMRI image preprocessing was the registration to T1-weigthed images, which were previously skull stripped with the Brain Extraction Tool and segmented using FMRIB's Automated Segmentation Tool (94), through a 7 degrees-of-freedom linear affine transformation through the FMRIB's Linear Image Registration Tool (95).

The second preprocessing step was performed using the Statistical Parametric Mapping software package (SPM12) running on MATLAB and FSL. During this stage, the first four volumes of the acquisition were discarded to allow for magnetization signal stabilization, minor head movement was corrected using MCFLIRT, and non-brain tissue was removed.

Subsequently, the REST software was employed for temporal filtering with linear detrending and bandpass filtering between 0.01 and 0.08 Hz to minimize high-frequency noise and signal drift. Additionally, REST was used to compute six motion parameters, along with the mean signals from the ventricular CSF and WM, which were used to reduce the impact of non-neuronal sources of signal synchrony and motion-related artifacts.

4.3.2.1.Functional Connectome Reconstruction

In healthy controls, undirected, weighted graphs describing brain network functional connectivity were obtained by computing correlations between the 83 GM segmented ROIs. Mean time series were extracted from each of the 83 regions of interest by averaging signals from all voxels belonging to the region. In order to exclusively take into account the voxels that correspond to the GM and prevent the influence of atrophy, resting data was masked with the GM map of each subject to not consider the effects of atrophy. The Pearson's correlation coefficient between the mean time-series of each node pair was calculated and entered into a functional connectivity matrix.

Pearson's correlation coefficients were then converted to z-scores using Fisher's r-to-z transformation. The matrix was further filtered based on the presence of anatomical connections in an independent healthy control sample.

4.3.2.2. Structural Connectome Construction of Independent Controls

The construction of these anatomical connections relied on a pulsed gradient SE single shot echo-planar acquisition (with TR = 6713ms, TE = 86ms, flip angle = 90°, FOV = 224x220mm) resulting in 50 contiguous axial slices with voxel size 2x2x2.6mm with diffusion-encoding gradients applied in 65 non-collinear directions (b factor = 1000s/mm^2) and seven averages of the acquisition with b equal to 0. The resulting images were parcellated in the same way as previously described, skull-stripped (with Brain Extraction Tool from FSL), and corrected for distortions (96).

To correct for motion and eddy current distortions, a rigid-body three-dimensional motion correction (six parameters) was combined with a constrained nonlinear warping procedure (eight parameters) based on a model of expected eddy current distortions. These transformations were concatenated with an additional affine transformation to register diffusion-weighted (DW) images to MNI space, and the resulting transformation was applied to the DW data.

The diffusion tensor (DT) was estimated on a voxel-by-voxel basis using the DTIfit toolbox, which is part of the FMRIB Diffusion Toolbox (FDT) within FSL. This process generated voxel-wise fractional anisotropy (FA) maps, which were used for subsequent white matter tractography.

White matter (WM) fibre tracts were reconstructed using Diffusion Toolkit/TrackVis (97) with the Fiber Assignment by Continuous Tracking (FACT) algorithm. Whole brain tractograms were generated by initiating fibre tracking from each WM voxel, following the principal diffusion direction. Tracking was terminated if the streamline entered a voxel with FA < 0.15, if the trajectory made a turn with a curvature angle exceeding 45°, or if the streamline exited the brain mask.

An individual structural brain network was generated for each healthy control using the following procedure (98). First, the streamlines from the whole-brain tractogram that connected each pair of nodes were identified. The number of streamlines for each tract was then computed and recorded in an adjacency matrix. If no streamlines connected a pair of nodes, a zero was assigned to indicate the absence of a structural connection. To reduce the presence of spurious fibres, connections with fewer than three streamlines were set to zero along with connections present in less than 40% of the sample.

This process was repeated for each pair of nodes, resulting in an undirected, weighted connectivity matrix. Finally, functional connectivity matrices for both patients and controls were masked using the structural connectivity matrix derived from the independent healthy control sample. If a structural connection was absent in this reference matrix, the corresponding functional correlation coefficient in the functional connectivity matrix was set to ‘NaN’ (not a number).

4.4.Connectomics

4.4.1. Graph Analysis

To analyse differences across functional connectivity matrices between controls and PD groups, graph analysis was employed. The graph measures to be extracted were selected based on the framework established in previous graph-theoretical studies of brain networks. (66) (65) (99).

a) Clustering Coefficient

The clustering coefficient quantifies the extent to which a node's neighbours are also connected to each other, thereby forming tightly interconnected communities within the network. This measure reflects functional segregation, which describes the brain's ability to form specialized processing units. Higher clustering coefficients indicate stronger local connectivity and the presence of modular structures within the network. The clustering coefficient for the network is calculated in the following way:

$$C = \frac{1}{n}\sum_{i \in N} C_i = \frac{1}{n}\sum_{i \in N} \frac{2t_i}{k_i(k_i - 1)}$$

where:

- C_i is the clustering coefficient of node i,
- t_i is the number of triangles (fully connected triplets) formed by the node,
- k_i is the degree of the node (the number of edges connected to it),
- n is the number of nodes in the network.

b) Transitivity

Another measure of functional segregation is transitivity which assesses the overall tendency of the network to form tightly connected communities. Higher transitivity values suggest a network that maintains modular processing while still enabling long-distance communication. Transitivity is calculated in the following way:

$$T = \frac{\sum_{i \in N} 2t_i}{\sum_{i \in N} k_i(k_i - 1)}$$

c) Local Efficiency

Last measure reflecting integration is local efficiency, a variant of global efficiency that quantifies the efficiency of information transfer within the local neighbourhood of a node.

$$E_{loc} = \frac{1}{n}\sum_{i \in \mathrm{N}} E_{loc,i} \;=\; \frac{1}{n}\sum_{i \in N} \frac{\sum_{j,h \in N, j \neq i} a_{ij} a_{ih} \left[d_{jh}(N_i)\right]^{-1}}{n - 1}$$

Where:

- $E_{loc,I}$ is the local efficiency of node i,
- a_{ij} is the presence of the connection between nodes i and j (1 if the connection exists and 0 if it doesn't),
- d_{jh} is the shortest path length between the nodes j and h.

d) Characteristic Path Length

Characteristic path length represents the average shortest path between all pairs of nodes in the network and provides insight into functional integration, or how efficiently information is transferred across distant brain regions. Networks with shorter characteristic path lengths tend to support faster and more efficient global communication. It is calculated as:

$$L = \frac{1}{n}\sum_{i\in \mathrm{N}} L_i = \frac{1}{n}\sum_{i\in N}\frac{\sum_{j\in N, j\neq i} d_{ij}}{n-1}$$

where L_i is the average distance between node *i* and all other nodes, and d_{ij} represents the shortest path length between each pair of nodes.

e) Global Efficiency

Another measure of functional integration is global efficiency which measures the efficiency of parallel information transfer in a network and is the inverse of the characteristic path length. It is defined as:

$$E = \frac{1}{n}\sum_{i\in \mathrm{N}} E_i = \frac{1}{n}\sum_{i\in N}\frac{\sum_{j\in N, j\neq i} d_{ij}^{-1}}{n-1}$$

f) Mean Distance

Mean distance quantifies the average distance between a node and all other nodes in the network. It provides insight into how well the network maintains efficient communication despite potential disruptions and it's calculated as:

$$D_{mean} = \frac{1}{n}\sum_{i\in N} D_i = \frac{1}{n}\sum_{i\in N}\frac{1}{n-1}\sum_{j\in N, j\neq i} l_{ij}$$

Where:

- D_i is the mean distance of node *i* from other nodes,
- l_{ij} represents the number of edges in the shortest path between nodes.

g) Nodal Degree

Nodal degree is a fundamental measure of hub identification, representing the number of direct connections a node has with other nodes. Higher average degree values indicate more highly connected nodes, which may serve as key hubs within the network. Calculated in the following way:

$$k_{mean} = \frac{1}{n}\sum_{i\in N} k_i = \frac{1}{n}\sum_{i\in N}\frac{1}{n-1}\sum_{j\in N, i\neq j} a_{ij}$$

where k_i is the degree of a node.

h) Nodal Strength

Nodal strength extends the concept of nodal degree by incorporating the weight of connections, rather than considering only their presence or absence. This measure provides a more nuanced assessment of node influence within the network.

$$k_{mean}^{w} = \frac{1}{n}\sum_{i\in N} k_i^w = \frac{1}{n}\sum_{i\in N}\frac{1}{n-1}\sum_{j\in N, i\neq j} w_{ij}$$

where w_{ij} is the weight of the connection between nodes.

i) Betweenness Centrality

Betweenness centrality quantifies the extent to which a node acts as a bridge for information flow between other nodes. It is a key metric for identifying connector hubs, which facilitate communication between different modules of the network and its mean is calculated as:

$$BC = \frac{1}{n}\sum_{i\in N} BC_i = \frac{1}{n}\sum_{i\in N}\frac{1}{(n-1)(n-2)}\sum_{h\neq j\neq i}\frac{\rho_{hj}(i)}{\rho_{hj}}$$

where:

- BC_i is the betweenness centrality of node *i*,
- ρ_{hj} is the total number of shortest paths from node *h* to node *j*,
- $\rho_{hj}(i)$ is the number of those paths that pass through node *i*.

j) Eigenvector Centrality

Eigenvector centrality provides a measure of node influence by considering not only a node's connections but also the importance of its neighbours. This metric is particularly useful for identifying highly influential hubs within the network. It is extracted as:

$$EC = \frac{1}{n}\sum_{i\in N} EC_i = \frac{1}{n}\sum_{i\in N} eig(FC)$$

where EC_i is the eigenvector centrality of node *i*, which is the i-th element in the eigenvector corresponding to the largest eigenvalue of the functional connectivity matrix (FC). (99)

Global and local metrics were compared between groups using ANOVA models, followed by post-hoc pairwise comparisons, Bonferroni-corrected for multiple comparisons ($p<0.05$). Box plots were used to visualize metrics distribution among patients and lobes.

4.4.2. Network Based Statistics

To investigate differences in functional connectivity between patient and control groups, network-based statistical (NBS) analysis was employed (68). When comparing PD groups to healthy controls, age and sex were included as covariates. For comparisons between different PD subgroups, UPDRS-III score was incorporated to correct for disease severity.

The analysis followed a network-based statistical approach, designed to identify clusters of significantly altered connections while controlling for multiple comparisons. Rather than examining each connection independently, this method assesses whether sets of functionally connected regions exhibit systematic group differences in pairwise comparisons

To assess differences in functional connectivity, a multivariate analysis of covariance (MANCOVA) was applied at each connection in the network. To account for multiple comparisons, network-based correction was applied by identifying clusters of significantly altered connections be retaining only connections where the p-value was below a predefined threshold ($p < 0.05$). They were then assessed for network-wide significance by examining the largest set of interconnected nodes that exhibited significant alterations.

To determine whether the observed connectivity differences were statistically meaningful, a permutation-based significance test was conducted by randomly shuffling group labels 5000 times and repeating the analysis for each permutation. This generated a null distribution of network differences that would be expected due to random variation.

By comparing this null distribution with the observed alterations from the original group labels, an empirical p-value was computed. A p-value below 0.05 was considered indicative of statistically robust differences.

4.5.Model

4.5.1. System of Ordinary Differential Equations (ODE)

The model used for simulating atrophy progression is the Aggregation-Network-Diffusion (AND) Model, developed by Raj et al. (2021), originally used for progression of tau pathology in AD, and characterized by a system of ordinary differential equations. This implementation adapts the model to α-Syn pathology in PD by incorporating modifications that account for key differences between the two proteins, such as variations in protein form classification. The characteristic mechanisms of this model, i.e. monomer production, aggregation and network diffusion, are integrated as follows:

- Monomer Production

Misfolded protein production starts and continues in a seed region, following a gamma-shaped function with temporal support corresponding to the duration of the neurodegenerative disease. This aspect is considered exclusively for monomers (m = 1) and is modelled in the following way:

$$\frac{\partial \alpha_{1,f}(v,t)}{\partial t} = c_2 f_\alpha(v,t)$$

where c_2 is the global constant linking monomer production rate to network diffusivity, and f_α is the gamma shaped function defined as:

$$f_\alpha(v_i,t) = \begin{cases} f_\alpha(t) & , \quad v_i = v_{seed} \\ 0 & , \quad \text{otherwise} \end{cases}$$

with

$$f_\alpha(t) = \frac{t}{\sigma_f} exp(-\frac{t}{\sigma_f})$$

Where v is the vector identifying the region with v_{seed} as the seed for disease start, t is the time in years, σ_f is the time scale of monomer production indicative of total disease.

- Aggregation of α-Syn

This process follows Smoluchowski kinetics, describing the aggregation of α-Syn into groups of protein forms codified through the variable *m*, from monomers (m = 1) to mature fibrils (m = M = 6) passing from each intermediate species: dimers (m = 2), oligomers (m = 3), prefibrillar species (m = 4), large prefibrillar assemblies (m = 5) (26). The phenomenon is described through the following aggregative terms, which are part of the system of ordinary differential equations describing the model:

$$\begin{cases} \dfrac{\partial \alpha_{1,agg}(v,t)}{\partial t} = -c_1 \alpha_1(v,t) \sum_{j=1}^{M} a_{1j} \alpha_j(v,t) \quad , \quad for\ m = 1 \\ \dfrac{\partial \alpha_{m,agg}(v,t)}{\partial t} = c_1 \left[\dfrac{1}{2} \sum_{j=1}^{m-1} a_{j,m-j} \alpha_j(v,t) \tau_{m-j}(v,t) - \tau_m(v,t) \sum_{j=1}^{M} a_{m,j} \alpha_j(v,t) \right], \quad for\ 2 \geq m \geq 6 \end{cases}$$

where α_m is the concentration of amount of protein form present in region v at time t, c_1 is the global constant relating aggregation rate to network diffusivity and $a_{m,j}$ is the aggregation rate parameter defined as:

$$a_{m,j} = \frac{mj}{\sigma_{agg}^2} exp\left(-\frac{mj}{\sigma_{agg}^2}\right)$$

Where m and j are the protein form numbers, and σ_{agg} is the scaling constant governing relationship between aggregation and oligomer size.

- Diffusion of α-Syn

Network-based diffusion is used to model the propagation of misfolded α-Syn across the brain functional connectivity. This term relies on this formulation:

$$\frac{\partial \alpha_{m,diff}(v,t)}{\partial t} = -\beta d_m \Delta_\Gamma \alpha_m(v,t)\,, \qquad for\ 1 \geq m \geq 6$$

Where Δ_Γ is the Laplacian of the averaged functional connectivity matrix of healthy controls, d_m is the diffusion rate expressed in the following way:

$$\begin{cases} d_M = \dfrac{m}{\sigma_{diff}} exp\left(-\dfrac{m}{\sigma_{diff}}\right), \qquad for\ 1 \geq m > 6 \\ d_M = 0\,, \qquad for\ m = M\ = 6 \end{cases}$$

Which governs the diffusion of different protein forms. The formulation for mature fibrils (m = M = 6) is set to zero due to the hard constraint on the diffusion of mature fibrils, considered too heavy to diffuse across the network.

- Complete System of Ordinary Differential Equations

Accounting for each of the mechanisms described, the system of ODE defines separate equations for each of the species considered. Monomer modelling includes all three terms of diffusion, aggregation and production in the following way:

$$\frac{\partial \alpha_1(v,t)}{\partial t} = \frac{\partial \alpha_{1,diff}(v,t)}{\partial t} + \frac{\partial \alpha_{1,agg}(v,t)}{\partial t} + \frac{\partial \alpha_{1,f}(v,t)}{\partial t},$$

$$\frac{\partial \alpha_1(v,t)}{\partial t} = -\beta d_1 \Delta_\Gamma \alpha_1(v,t) - c_1 \alpha_1(v,t) + \sum_{j=1}^{M} a_{1j} \alpha_j(v,t) + c_2 f_\alpha(v,t)\,.$$

On the other hand, dimers, oligomers, prefibrillar species and large prefibrillar assemblies are modelled only through terms of diffusion and aggregation as follows:

$$\frac{\partial \alpha_m(v,t)}{\partial t} = \frac{\partial \alpha_{m,diff}(v,t)}{\partial t} + \frac{\partial \alpha_{m,agg}(v,t)}{\partial t}\,,$$

$$\frac{\partial \alpha_m(v,t)}{\partial t} = -\beta d_m \Delta_\Gamma \alpha_m(v,t) + c_1 \left[\frac{1}{2} \sum_{j=1}^{m-1} a_{j,m-j} \alpha_j(v,t) \alpha_{m-j}(v,t) - \alpha_m(v,t) \sum_{j=1}^{M} a_{m,j} \alpha_j(v,t) \right],$$

with m indicating each of the protein forms ranging from 2 corresponding to dimers to 5 corresponding to large prefibrillar assemblies. Last, mature fibrils are only modelled through aggregative terms:

$$\frac{\partial \alpha_M(v,t)}{\partial t} = \frac{\partial \alpha_{M,diff}(v,t)}{\partial t},$$

$$\frac{\partial \alpha_M(v,t)}{\partial t} = \frac{c_1}{2} \sum_{j+k \geq M;\, k,j<M} a_{j,k} \alpha_j(v,t) \alpha_k(v,t)\,.$$

The combination of these equations forms the basis for the AND model and allows for the analysis of the temporal evolution of the concentration of each of the 6 species.

4.5.2. ODE45

The numerical solution of the system of ODEs to obtain temporal evolution of concentration values is entrusted to the ODE45 solver in MATLAB (100) which is a variable-step, Runge-Kutta (4,5) method, which is well-suited for solving non-stiff ordinary differential equations. This solver was selected as it was used by the initial proposers of the AND model in use. (83)

4.5.2.1.Initialization

For each simulation, the solver was initialized with:

- A zero-state vector representing baseline conditions across all regions indicating the absence of misfolded α-Syn in the system.
- A set of time points defining the times at which the solution must be evaluated for comparison with observed atrophy.
- A function representing the system of ODEs of the AND model with its parameters.

4.5.2.2.Configuration

The ODE45 solver was configured with appropriate numerical tolerances to ensure stable and accurate solutions:

- Relative Tolerance set to 10^{-2} controlling error estimation to maintain a balance between precision and efficiency.
- Absolute Tolerance equal to 10^{-4} ensuring accurate resolution of small changes in atrophy dynamics.
- Non-negativity constraints enforced to prevent implausible negative values in protein concentration.

4.5.3. Evaluation of System Output

The evaluation of the system by the ODE45 solver generates a matrix representing α-Syn concentration for the six considered forms across all 83 brain regions and at each timepoint. In contrast, the real atrophy data is structured as a bidimensional matrix, capturing atrophy values across the same 83 regions but with time points varying based on scan availability.

To evaluate the model's accuracy, correlations were computed by selecting specific combinations of α-Syn forms from the model output. The simulated atrophy (SA) for each region and time point was calculated as:

$$SA(r, tp) = \sum_{f \in C} O_f(r, tp)$$

where:

- *SA(r,tp)* represents the predicted atrophy for region *r* at time point *tp*.
- $O_f(r,tp)$ is the ODE solver output for each α-Syn form *f*.
- *C* denotes the subset of protein forms considered in each trial.

Once the predicted atrophy was extracted for each region at each time point, Pearson's correlation coefficient was computed between the predicted values and the z-scored real atrophy of PD patients. The predicted and real atrophy values for the seed region were excluded from this calculation, as the gamma-shaped monomer generation function could, if monomers were in the subset *C*, introduce a reduction in simulated atrophy at later timepoints, which should otherwise follow a monotonically increasing trend.

Correlation values were considered significant if the associated p-value was below a significance threshold of 0.05, generating multiple correlation values for each patient depending on the number of available scans. Non-significant correlations were set to not a number, ensuring that atrophy predictions at baseline were always assigned a null value, as the model inherently produces a zero solution at time zero.

4.5.4. Optimization

The implementation and optimization of the model involved several trials testing its components and strategic adjustments to maintain its generalizability, ensuring its applicability to the broadest population possible. The initial approach leveraged parameter values from the first implementation of AND to provide an individualized strategy for selecting seed regions. The next phase of development shed fixed-variable assumptions by exploring broad parameter ranges, establishing a robust basis for choosing the protein forms incorporated into the simulated atrophy. Both these aspects and their results culminated in a complete model, enabling a MATLAB optimizer to determine optimal individualized model parameters.

4.5.4.1.Seed Region Selection

The first investigation focused on selecting the seed region, a critical component of the model. The objective was to determine whether the seed region could be established as an *a priori* variable or if it needed to be individualized for each patient. Despite literature indicating uncertainty about the initial regions of α-Syn misfolding, both approaches were explored using a model with fixed parameters used in the first implementation of AND by Raj et al. (83).

Given the lack of consensus in the literature regarding the neurotoxic effects of mature fibrils of α-Syn, and the understanding that neurodegeneration is likely caused by a combination of protein forms (26), the predicted atrophy was calculated by including all six protein forms generated by the model.

To evaluate the performance of each approach, correlations were averaged across the entire dataset while setting negative and non-significant values to zero. The individualized region selection approach involved two steps: first, running the model for all potential regions, and second, choosing the region that yielded the

highest correlation performance at the first follow-up time point. This approach was designed to facilitate potential future applications of the model where the initial region could be determined based on early simulated atrophy correlations, allowing for accurate progression simulations.

To evaluate the effectiveness of this approach, it was compared against a fixed-region approach, where the model was run using each region as the seed. The performance of both methods was compared to determine whether individualized region selection provided a significant advantage, and the best strategy was selected and used for each model run for the following trials.

4.5.4.2.Exploration of Suitable Parameters Bounds

The next step involved identifying suitable upper and lower bounds parameter values for following optimization steps. This was done through a series of trials and manual visualization of single-subject results, allowing for the observation of instances where individual patients required bound expansions values.

First approach utilized a grid search to explore potential values for global parameters (β, c_1, c_2) only, ensuring manageable computational time while exploring variable spaces. During this phase, the scaling parameters were maintained at the values proposed by Raj et al. (83), and the model output was calculated as the sum of all six protein forms, in the same way as previously done.

Once the grid was sufficiently wide to encompass peak correlation values for all patients, the strategy evolved to include the scaling parameters, whose bounds were determined. The result of this analysis provided a solid foundation for the following process, facilitating more precise optimization of the model's predictive performance.

4.5.4.3.Protein Form Selection

As described in Section 5.3.3, the AND model output must be converted into simulated atrophy through a weighted sum, determined by the specific combination of α-Syn protein forms contributing to neurodegeneration. This approach stems from the hypothesis that different α-Syn species may drive atrophy in PD (26), challenging the assumption made in the tau-based implementation of this model, where only mature fibrils were considered. To systematically evaluate all possible protein form contributions, a six-dimensional grid was constructed based on the bounds of each model parameter. Each point of the grid corresponded to a set of parameters which was used to generate a system output and combined to generate simulated atrophy values.

Given that six protein forms were analysed, the total number of possible combinations was 2^6 (63) minus one, excluding the scenario where no protein form was selected, resulting in 63 distinct atrophy simulations for each grid point. For each point, the simulated atrophy was correlated with real atrophy data across all patients, and the combination yielding the highest average Pearson correlation coefficient was identified as optimal. The most frequently selected combination across all patients was then used as the reference for the following optimization efforts.

By following this process, the generalizability of this selection was significantly improved, ensuring that the optimal combination of protein forms would perform consistently across diverse patient profiles and not just under narrowly defined conditions.

4.5.4.4.Constant Optimization

The ODE45 solver was embedded within an optimization function to estimate model parameters that yielded the best correlated simulated atrophy values. The *surrogateopt* (101) function in MATLAB was employed, which is a derivative-free global optimization method designed for high-dimensional problems where function evaluations are costly as the model evaluation is.

The objective function was evaluated based on a performance index calculated as the sum of significant correlations for each timepoint. The optimization was performed over a six-dimensional parameter space corresponding to the aforementioned model parameters (β, c_1, c_2, σ_f, σ_{diff}, σ_{agg}) and each parameter was scaled by a predefined multiplier to enforce integer constrains reducing the capillarity with which the variables needed to be investigated. Upper and lower bounds of evaluation were kept from previous steps.

The surrogateopt function was configured with the following settings:

- the maximum amount of function evaluations (MaxFunctionEvaluations) was set to 1000 to avoid excessive computational time;
- for the same reason, the maximum amount of time (MaxTime) per patient optimization was set to 10,000 seconds (2.8 hours);
- upper and lower bounds for each model variable corresponding to the ones determined during the exploration of parameter bounds;
- initial guess for parameters which was set arbitrarily through performance observations made in the grid searching phase.

To enhance computational efficiency, parallel computing was enabled using MATLAB's parfor (102) function. This allowed multiple patient-specific optimizations to run concurrently, reducing the overall runtime significantly.

Each patient underwent an independent optimization run, with the best-fit parameter set identified based on the highest correlation between predicted and actual atrophy progression. Once optimization was complete, the selected parameters were scaled back to their original values for further analysis.

5. Results

5.1.Connectomics

5.1.1. Graph Analysis

The statistical analysis of network measures revealed significant differences in only a subset of the evaluated graph measures across the contrasts considered, as detailed in Table 5.1. The comparison between GBA-positive patients and healthy controls identified reductions in two key network measures. A decrease in nodal degree was observed in the temporal, sensorimotor, and parietal lobes, indicating that several regions within these lobes became functionally disconnected from the rest of the network, reducing overall brain efficiency and synergy potential and impairing communication.

Additionally, betweenness centrality differences were recorded in the left hemisphere, suggesting alterations that affect the capacity of specific regions to facilitate information flow. Further differences in the same measure were identified when comparing GBA-positive and GBA-negative patients, specifically in the left occipital lobe, as well as in the right frontal lobe when comparing GBA-negative patients and healthy controls.

These findings suggest that network disruptions follow distinct patterns depending on genetic mutation with GBA-positive patients exhibiting more pronounced functional connectivity alteration and efficiency reduction.

Contrast	**Measure**	**Lobe**	**p-Value**
GBA-positive vs HC	Nodal Degree	Temporal	0.037
		Left-Temporal	0.017
		Sensorimotor	0.049
		Left-Sensorimotor	0.023
		Right-Hemisphere	0.033
		Right-Frontal	0.034
		Right-Parietal	0.022
	Betweenness Centrality	Left-Hemisphere	0.027
GBA-positive vs GBA-negative	Betweenness Centrality	Left-Occipital	0.023
GBA-negative vs HC	Betweenness Centrality	Right-Frontal	0.035

Table 5.1 : Significantly affected graph measures for all contrast between the three groups: HC, GBA-negative and GBA-positive.

5.1.2. Network Based Statistics

Network-based statistics confirm that the most significant differences are observed in the comparison between healthy controls and GBA-positive patients. In this contrast, functional connectivity was affected in 26 connections involving nodes in the parietal, left temporal, left occipital, sensorimotor, and right frontal regions. No affected connections were identified in other contrasts, further suggesting that GBA-positive patients experience more pronounced network disruptions compared to GBA-negative patients or healthy controls.

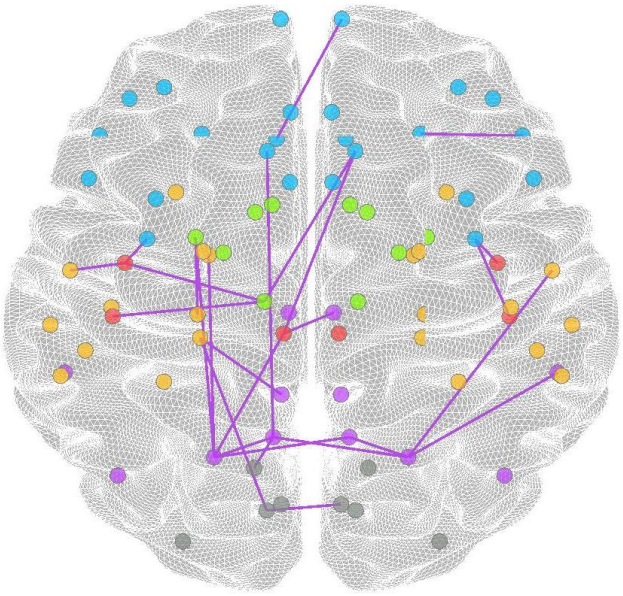

Figure 5.1: Transversal view of affected connections which are highlighted in purple. The colour of each region is relative to the lobe they are part of, following this code: blue is frontal lobe, green is basal ganglia, red is sensorimotor lobe, purple is parietal, yellow is temporal and grey is occipital.

5.2.Simulating Atrophy

5.2.1. Seed Region Selection

To investigate which seed region selection strategy was the most effective between the fixed and individualized one, the average correlation performance was conducted over the whole dataset. At no timepoint did any single region prove effective enough to generate correlations comparable to those obtained with the personalized selection approach. Even though the effectiveness of the personalized strategy declined in later timepoints, as indicated by a reduction in average correlation performance, the fixed seed reference remained significantly less effective throughout the progression.

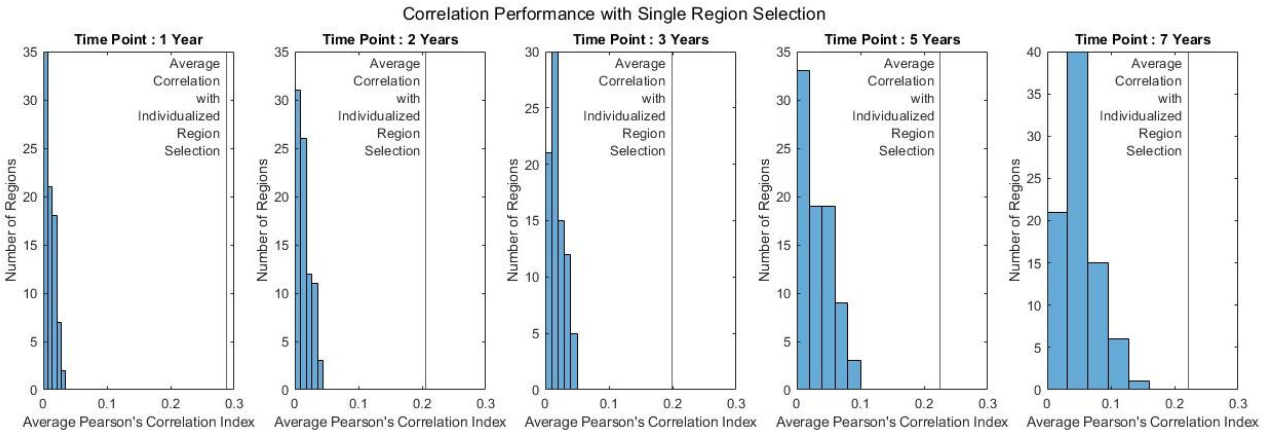

Figure 5.2.1: Histograms comparing the average Pearson's correlation performance between seed region selection strategies across all considered time points. The distribution of performance for the fixed region approach across all patients is represented in blue, while the black line denotes the performance obtained through an individualized approach.

5.2.2. Exploration of Suitable Parameter Bounds

The first phase of the exploration focused on evaluating global parameters, revealing that single patient Pearson's correlation values were highly dependent on the diffusive parameter β while showing relative robustness to parameters c_1 and c_2. The sensitivity to each parameter was assessed by visually inspecting graphs of each patient while evaluating whether to expand boundaries in the effort of increasing maximum correlation performance, one example of this tendency can be seen in figure 5.2.2.

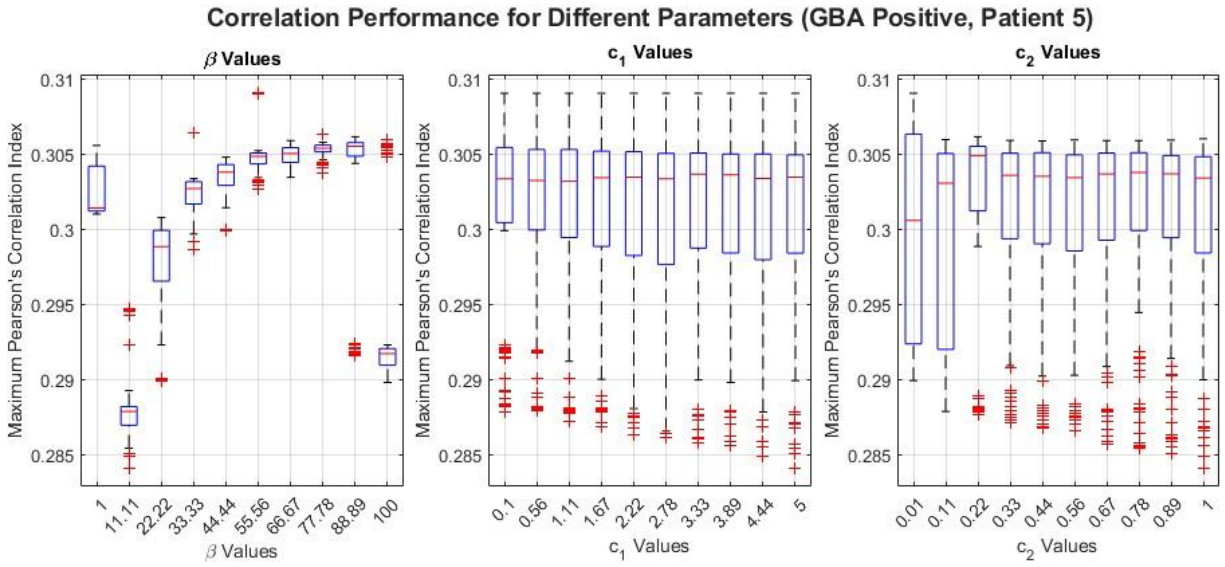

Figure 5.2.2.1 Boxplots representing the maximum Pearson's correlation indexes achieved with varying model parameter values of β, c_1, c_2, for patient 5 from the GBA-positive group.

Analysis of β distribution showed that the performance variation within the same parameter value was limited with respect to the variations observed with different β values, indicating that it was the primary determinant of model performance, while reinforcing the reduced influence of c_1 and c_2. As a result, β required broader parameter bounds to achieve meaningful performance improvements across all patients leading to the upper bound set to 100.

Once these values were determined, the same process was applied to the scaling parameters, with a reduced resolution in the step sizes used for global parameters. A heightened dependency of maximum correlation was identified for the σ_{diff} parameter which carries a similar meaning to β as it is related to diffusivity within the model as this variable affects the diffusivity of different protein forms in different ways, favouring diffusion of monomers with respect to fibrils.

The emergence of this pattern across both β and σ_{diff} is consistent with the model's mathematical formulation, in which these parameters are multiplicatively linked. Their combined variation directly influences the diffusion component of the model, which serves as the primary driver of atrophy spread.

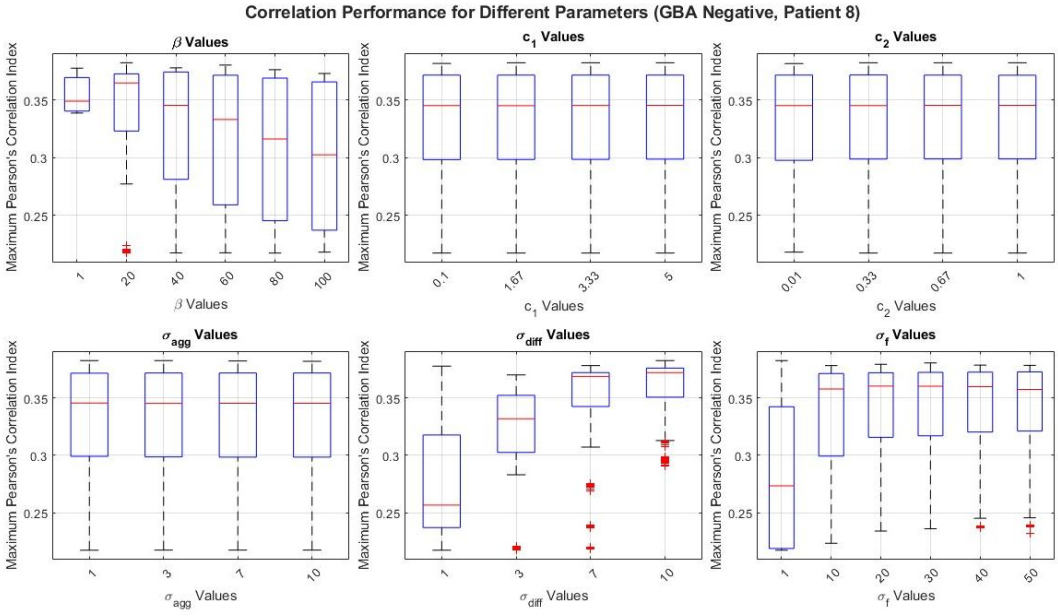

Figure 5.2.2.2: Boxplots representing the maximum Pearson's correlation indexes achieved with varying all model parameter values for patient 8 from the GBA-negative group.

5.2.3. Protein Form Selection

For each point of the grid of parameter sets, the optimal combination of protein forms was selected, and the resulting distribution was analysed.

The most frequently selected combination, accounting for more than 27% of parameter sets, included only monomers. The second and third most favoured combinations, representing 13% and 7% of selections, involved a mix of monomers with high molecular weight protein forms of large prefibrillar assemblies and mature fibrils. The fourth most preferred combination, chosen in 6% of cases, relied solely on mature fibrils.

Other combinations, each selected in 5% or fewer parameter sets, also incorporated prefibrillar species alongside monomers, large prefibrillar assemblies, or mature fibrils. These preferences indicate a recurring pattern in which monomers, either alone or in combination with larger aggregated species, play a significant role in driving atrophy dynamics in the model.

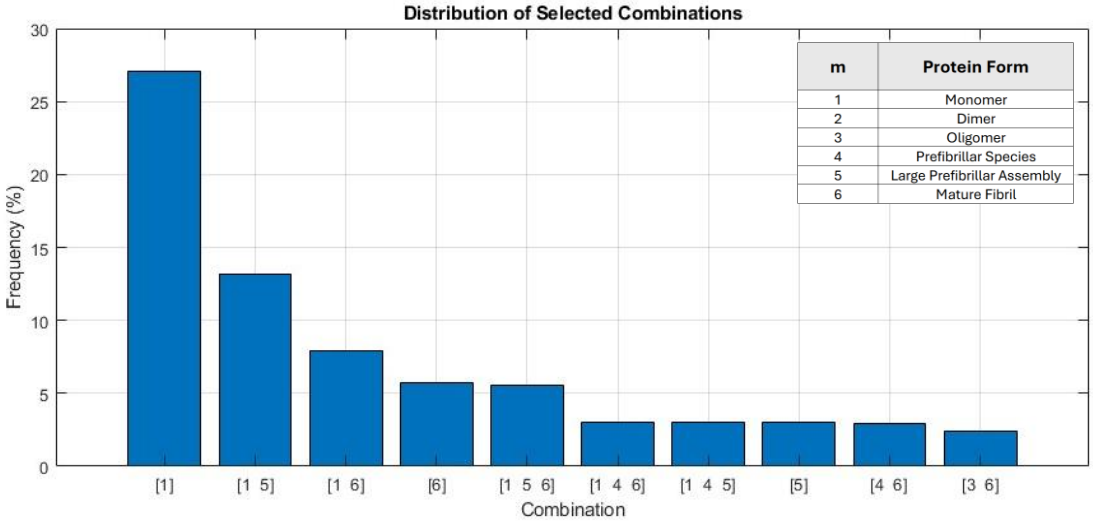

Figure 5.2.3: Distribution of combinations which retrieved the best correlations among the grid search parameter sets.

5.2.4. Performance of the Optimization Process

The individualized region selection and the use of monomers for the calculation of simulated atrophy, within the optimization framework resulted in significant correlations across most timepoints for the majority of patients. Among GBA-negative patients, only two individuals exhibited no correlated timepoints, suggesting that, despite identifying the global minimum of the objective function, the optimization process may not always yield suitable parameter values.

For most of these patients, all available timepoints were positively and significantly correlated, while a minority reported significant correlations in only a part of all timepoints. The model demonstrated a higher success rate in GBA-positive subjects compared to GBA-negative subjects, with only two GBA-positive patients showing incomplete correlations across available follow-up scans.

Across both datasets, the highest percentage of significant correlations were observed at the earliest timepoints, with a progressive decline in later stages. This pattern is likely influenced by the strategy used for selecting the seed region, introducing a performance bias favouring the early stages of disease progression.

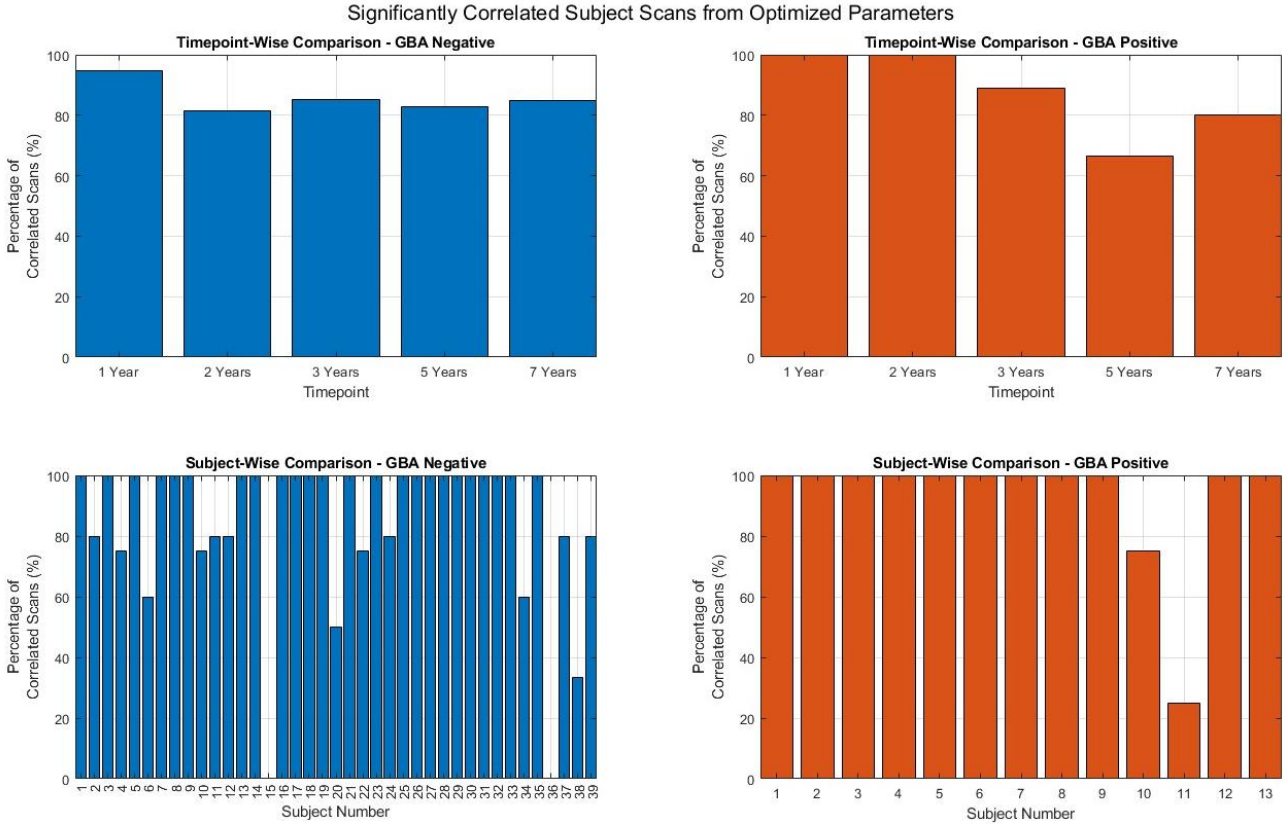

Figure 5.2.4.1: Histograms representing the percentage of significant and positively correlated scans for both GBA groups. Histograms on top represent comparisons across timepoints while the ones on the bottom represent comparisons across all patients within their respective PD group.

The decline in performance after the first follow-up is evident in the distributions of correlation metrics in Figure 5.2.4.2, where the maximum and median Pearson's correlation indexes decrease at later timepoints. Despite this reduction, the overall distribution of correlations remains relatively stable, indicating that the model maintains a broadly consistent performance across timepoints.

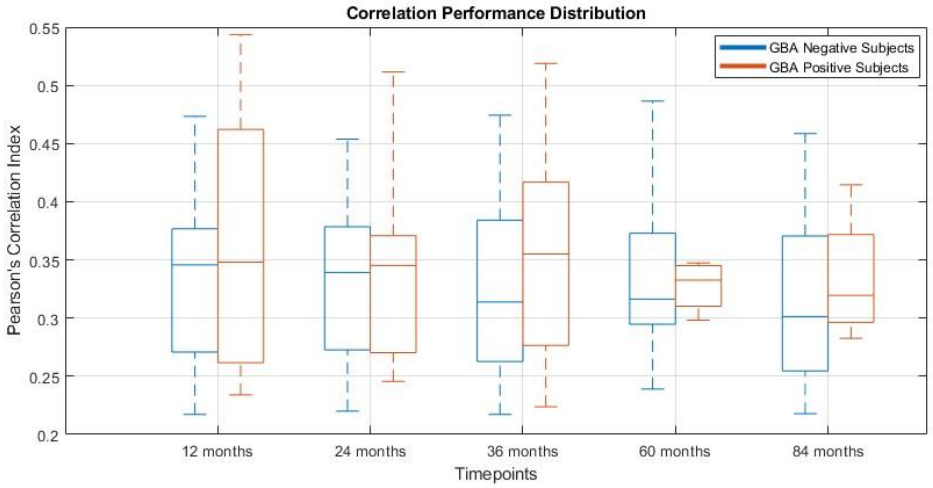

Figure 5.2.4.2: Boxplot of correlation performance across timepoints for both GBA-positive subjects (orange) and GBA-negative subjects (blue).

5.2.5. Parameters Selected in the Optimization Process

The optimization process allowed for the identification of parameters tailored to each patient, whose distribution was not uniform across the range. The β parameter, for example, exhibited a notable accumulation of selected values at the lower bound, with 15 GBA-positive and 4 GBA-negative patients selecting the lowest available value. Beyond this accumulation, the remaining distribution of β values was evenly spread across the range in both GBA groups, reflecting that the previous processes identified a sufficiently high upper bound.

Another pattern was observed for parameters c_1, c_2, and σ_{agg}, with values clustering at both the lower and upper bounds across both GBA groups. While this trend might suggest a need for further boundary adjustments, previous analyses indicated that these parameters have a limited impact on correlation performance, making further expansion unnecessary. In contrast, σ_{diff} and σ_f displayed a tendency toward the upper bounds of their respective ranges while still maintaining a sufficient spread across the full parameter space.

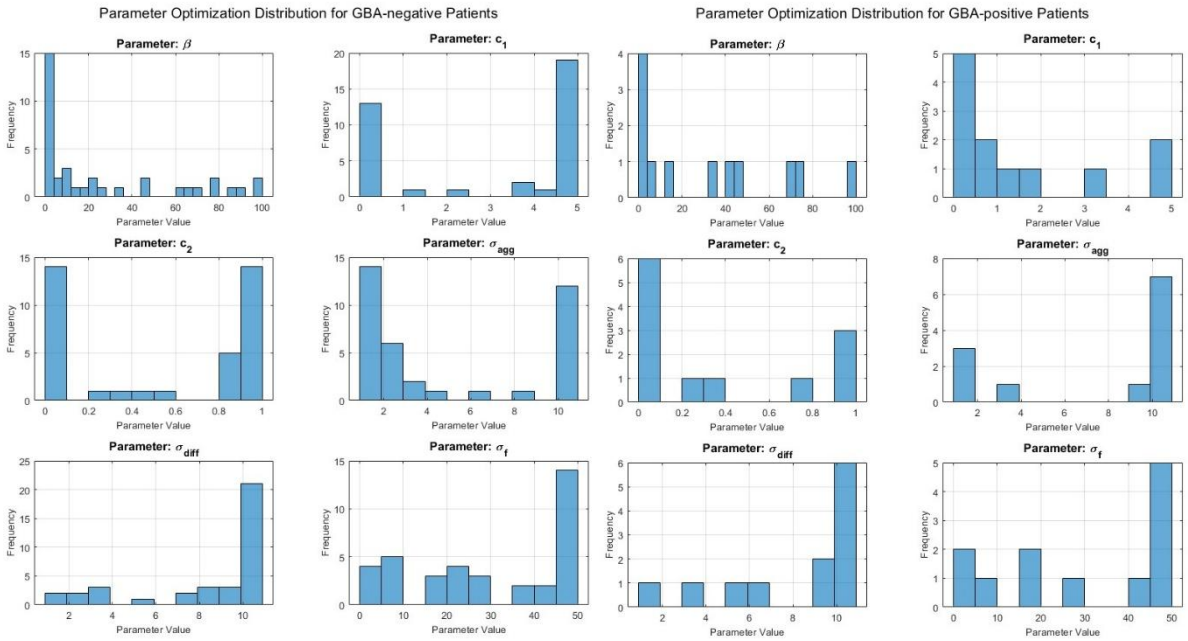

Figure 5.2.5: Histograms of the distribution of parameters selected by the optimization process for GBA-negative patients (left) and GBA-positive patients (right).

5.2.6. Regions Selected in the Optimization Process

Additionally, the distribution of selected seed regions was examined. GBA-negative patients predominantly exhibited a preference for seed regions within the temporal lobe, with secondary selections primarily located in the frontal lobe. GBA-positive patients also showed a strong preference for temporal lobe regions but demonstrated a separate secondary preference for the basal ganglia and sensorimotor areas. This differentiation in regional selection may reflect underlying differences in disease propagation patterns between the two groups.

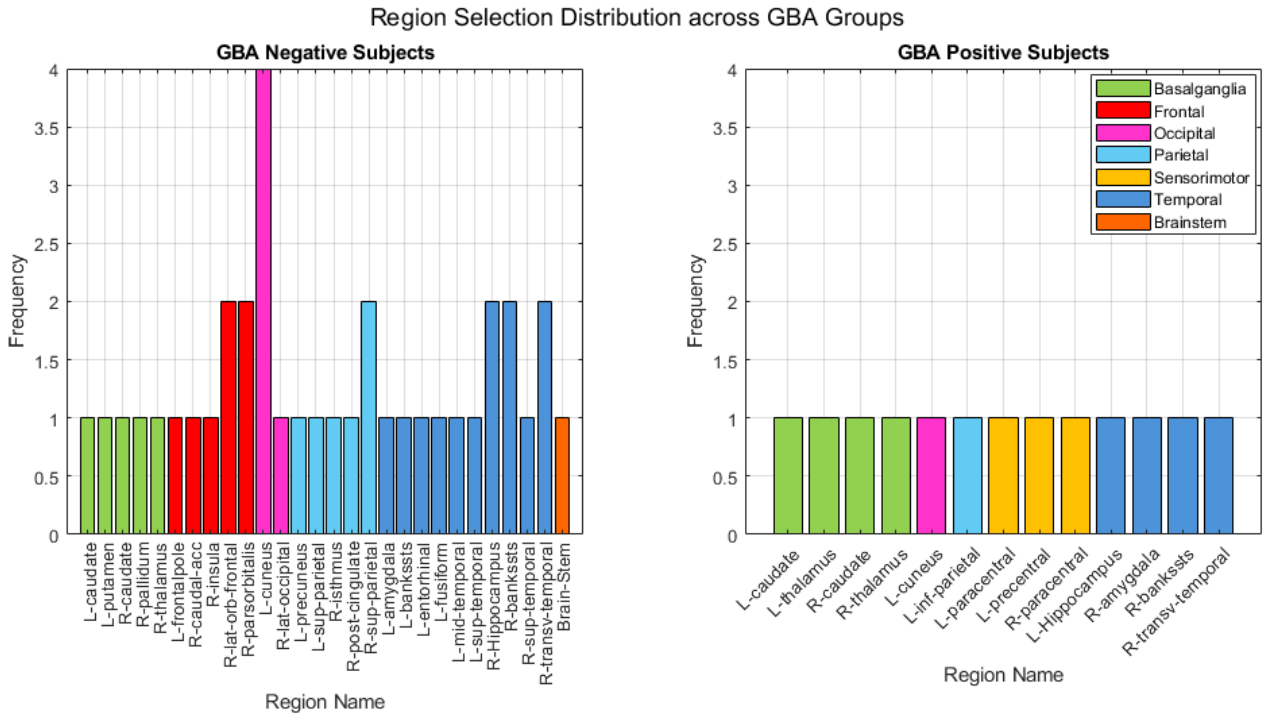

Figure 5.2.6: Histogram of the distribution of regions selected for GBA negative patients (left) and GBA positive patients (right).

5.2.7. Characteristic Atrophy Patterns

A defining parameter of the model is β, the network transmissibility constant governing the spread of atrophy across the functional network, as its variation had the widest impact on performance and on the shape of disease progression.

The difference between these low and high β patterns is evident while observing correlation plots between z-scored observed atrophy and simulated atrophy [Figure 5.2.6]. Lower β values were associated with a more localized and gradual spread of atrophy, with several regions remaining minimally affected throughout all the timepoints. In contrast, higher β values led to widespread involvement of most brain regions, even at the earliest stages of progression, with a further burden increase in the later timepoints.

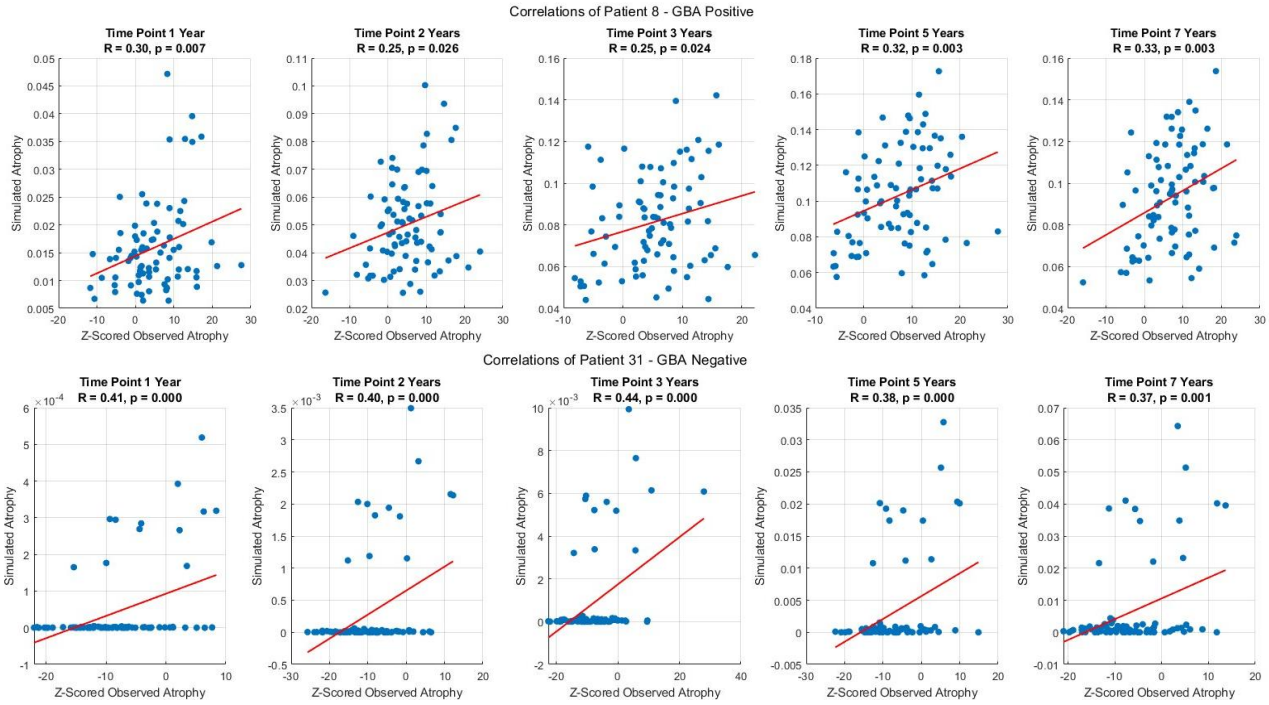

Figure 5.2.7 : Scatter plots correlating simulated to z-scored observed atrophy for patient 8, from GBA positive group, and Patient 31, from GBA negative group, highlighting differences in atrophy patterns along with β parameter variations.

5.2.8. Spatial and Temporal Evolution of Simulated Atrophy

A more comprehensive understanding of simulated atrophy dynamics can be achieved by visualizing its spatial progression across affected regions, as illustrated in Fig. 5.2.8. In the GBA-negative patient, the model identified the left amygdala as the seed region of misfolded α-Syn production along with optimized parameters characterized by a β parameter whose low value suggested that the atrophy spread would remain highly localized and close to the initial region. At the two-year timepoint, atrophy was confined to the left temporal lobe, with only mild involvement of other regions within the left hemisphere. As the disease progressed to year three, there was an overall increase in atrophy burden while still maintaining a largely lateralized pattern. By year five, atrophy extended further within the left hemisphere, progressively affecting the remaining lobes, without spreading to the right hemisphere yet. At the seven-year timepoint, the atrophy burden saturated the left hemisphere and finally extended into the right hemisphere. This pattern highlights the regionally restricted progression characteristic of low β values, where atrophy remains localized for an extended period before expanding more widely.

In contrast, the GBA-positive patient exhibits a very different atrophy trajectory driven by a high β value which is associated with rapid diffusivity through the network with early and widespread involvement of regions. By the two-year timepoint, atrophy starting from the seed region of the right banks of the superior temporal sulcus has already spread beyond the right temporal lobe the right parietal lobe. As the disease progresses to year three, the influence of the high β value becomes evident as atrophy extends across hemispheres, reaching lobes within the left hemisphere. By year five, a widespread increase in atrophy burden is observed, affecting all lobes across both hemispheres. This pattern continues into year seven, with extensive neurodegeneration observed across all major brain regions. Although this widespread atrophy trajectory is demonstrated here for a GBA-positive patient, it is a characteristic feature of all cases with a high β value even the GBA-negative ones, indicating that disease progression in such individuals is significantly more aggressive compared to those with lower β values.

The simulated patterns demonstrate that β values play a critical role in dictating atrophy spread dynamics. Low β values result in a localized, slower progression, while high β values lead to early, extensive neurodegeneration providing basis of reasoning for interpreting model parameters after fitting with possible applications for stratification of patients.

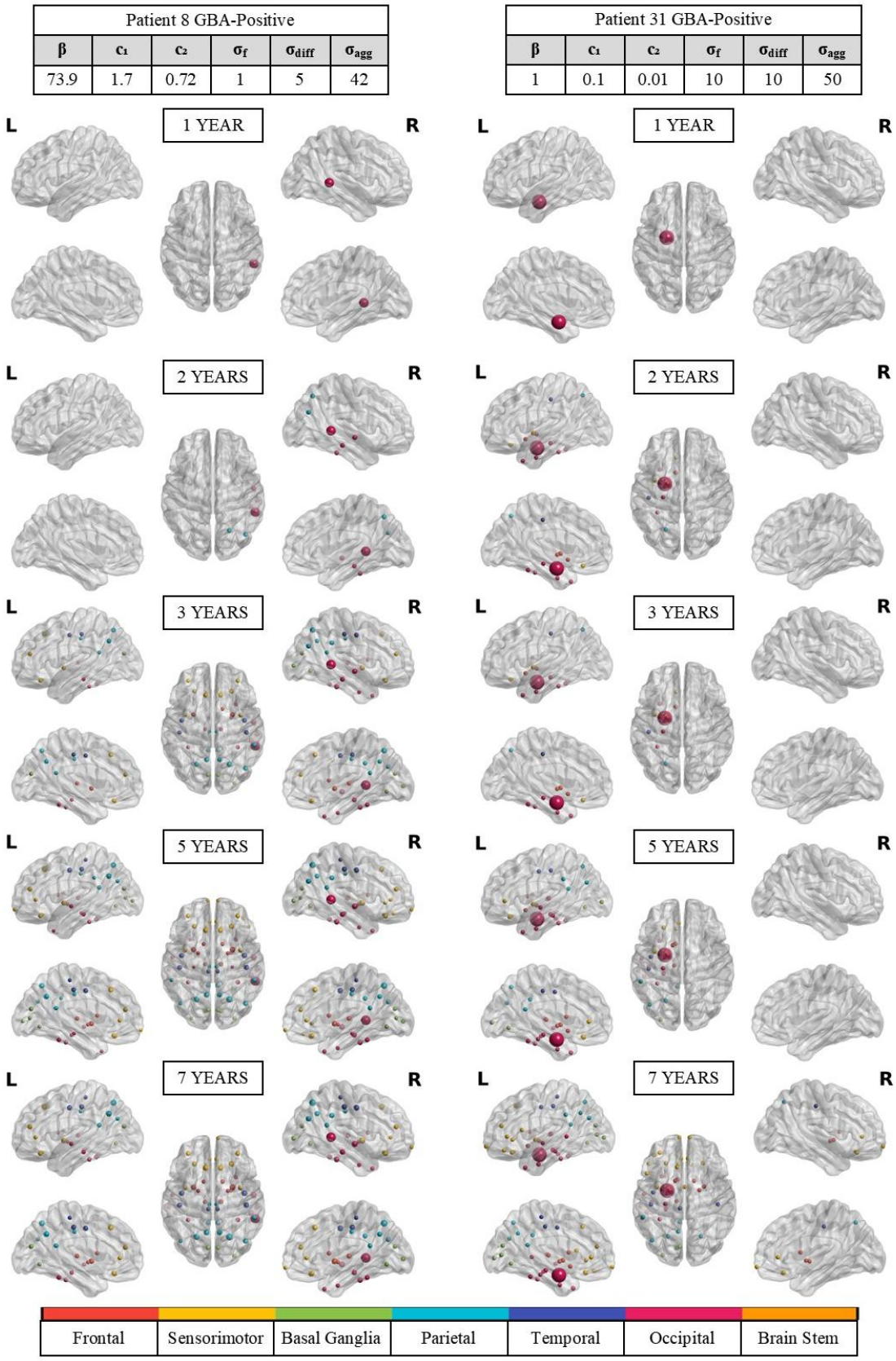

Figure 5.2.8: Representations of simulated atrophy for patient 8, from GBA positive group, and patient 31, from GBA negative group, highlighting differences in atrophy patterns along with β parameter variations.

6. Discussion

6.1.Connectomics

The investigation of graph measures obtained from functional connectivity reveals significant alterations in brain network topology associated with GBA mutations. The observed reductions in nodal degree and betweenness centrality, particularly in temporal, sensorimotor and parietal lobes suggest a pattern of decrease integration within these regions. Given the crucial roles of these areas in motor, sensory and cognitive functions, their disconnection may contribute to the poorer clinical outcomes observed in GBA-positive PD patients (56).

In contrast, GBA-negative patients exhibited reduced betweenness centrality within the right frontal lobe compared to healthy controls, indicating that PD without GBA mutations affects brain information transmission in different locations and to a lesser extent to GBA-positive PD.

The distinction between PD groups is further supported by betweenness centrality alterations within the left occipital lobe when comparing GBA-positive and GBA-negative patients, highlighting differences in affected brain regions and extent of connectivity disruptions.

NBS results further emphasize the greater disruption of connectivity in GBA-positive patients relative to healthy controls, in connections spanning multiple regions, including the parietal, temporal, occipital, sensorimotor, and frontal areas. The absence of significant connections in the contrasts (GBA-positive vs. GBA-negative and GBA-negative vs. HC) reinforces the notion that GBA mutations may drive unique alterations of functional network degeneration in PD. This is in line with previous research suggesting that GBA mutations lead to earlier and more aggressive disease progression, potentially mediated by glucocerebrosidase deficiency and its downstream effects on α-synuclein accumulation and neuroinflammation. (56)

Taken together, our findings support the hypothesis that GBA-positive PD represents a distinct subtype with pronounced network alterations. The observed disruptions may contribute to the increased cognitive and motor impairments often reported in this patient group. Future studies integrating longitudinal imaging and clinical assessments are needed to determine the progression of these connectivity changes over time and their potential as biomarkers for disease severity and therapeutic response.

6.2. Neurodegeneration Modelling

The results of the AND model highlighted the importance of individualized solutions for accurately simulating atrophy progression in PD. The single-patient selection of seed region proved instrumental in enhancing model performance as individualized seed selection consistently outperformed fixed seed references, yielding stronger correlations across all time points. This approach fits with the expectation of heterogeneity of PD progression.

The exploration of suitable parameter bounds highlighted that diffusion-related parameters (β and σ_{diff}) play a central role in determining model performance, exhibiting the greatest influence on correlation outcomes. This dependency reinforces the hypothesis that disease propagation in PD is primarily driven by network diffusion mechanisms, aligning with previous studies suggesting that a key driver of α-Syn pathology is its ability to spread through the brain network, ultimately contributing to progressive neurodegeneration (79). The strong influence of diffusive parameters further supports the notion that connectivity-based transmission plays a fundamental role in PD pathogenesis, similar to the network-based spread observed in other prion-like neurodegenerative conditions, such as AD.

A key aspect of the AND model was determining which protein forms contributed most prominently to the progression of atrophy. Monomeric α-Syn was the most frequently selected contributor, either alone or in combination with prefibrillar assemblies and mature fibrils. The consistent presence of monomers supports the hypothesis that the highly diffusive nature of this species of α-Syn is a major factor in disease propagation,

while larger aggregates may contribute locally rather than through widespread diffusion. The inclusion of high-molecular-weight protein forms in other favoured combinations suggests that atrophy progression results from a combination of effects from different α-Syn forms, rather than a single toxic species.

The presence of monomers as the primary protein form driver of PD atrophy progression is in line with the strong role of diffusive processes due to the properties of monomers of having the highest capabilities of diffusion across the network as per the model definition (83). As a consequence to this prevalence, the aggregation phenomena tend to play a secondary role possibly influencing in a stronger way local dynamics rather than whole brain mechanisms.

Parameter optimization and the analysis of their values revealed no distinct patterns in parameter value selection across the two PD subgroups highlighting the heterogeneity of PD progression. Notably, many patients from both subgroups converged toward low diffusivity parameters while a subset of patients, required a wider range of parameter values to achieve optimal correlations having high diffusivity parameters. This suggests that standard fixed-parameter models may overlook important inter-individual differences, which could provide insights into previously ignored disease progression patterns. By capturing this variety, the AND model proves its effectiveness as a patient-specific simulation tool, allowing for a more granular understanding of neurodegeneration dynamics.

The analysis of atrophy patterns in relation to the β parameter revealed clear differences in regional involvement. Specifically, lower β values were associated with a lateralized progression across most time points, a tendency that has been widely reported in the literature (103). Conversely, patients with higher β values exhibited early bilateral involvement, leading to widespread atrophy in both hemispheres even at the initial disease stages suggesting that lateralization may be a characteristic of only certain PD subtypes. The fact that some patients follow a lateralized trajectory, while others experience more diffuse, aggressive progression, underscores the need for biomarkers that can distinguish between these different disease courses.

Given its strong association with disease spread patterns, β could serve as a key biomarker for stratifying PD patients based on their disease trajectory. This offers a potential means of distinguishing between slow and aggressive disease courses, facilitating earlier intervention strategies and allowing for targeted therapeutic approaches aimed at slowing neurodegeneration before significant atrophy occurs.

7. Conclusion

The results of this investigation highlight critical differences in functional connectivity between GBA-positive and GBA-negative PD patients, with more pronounced network alterations observed in GBA-positive individuals. However, differences between GBA-positive and GBA-negative groups were not apparent in the simulated atrophy generated by the individualized AND model. Instead, the findings showed considerable variability in the choice of seed regions, individually optimized parameters, and the progression patterns of atrophy across individual patients.

Despite distinct functional connectivity disruptions, the similar atrophy dynamics simulated by the AND model across both PD subgroups suggest that genetic distinctions alone may not fully account for differences in neurodegenerative trajectories. Instead, the interplay of genetic factors, disease stage, and individual neurobiological variability must be considered to enhance personalized prognostic accuracy and therapeutic targeting in PD research.

Additionally, the individualized AND model demonstrates significant potential as a tool for early detection of PD by simulating disease progression based on patient-specific network properties. Future research should aim at integrating additional biomarkers, genetic details (particularly specific GBA mutations), and longitudinal clinical data to refine disease modelling. Further studies might also explore factors capable of better stratifying even GBA-negative patients, thus improving the precision and clinical relevance of PD simulations.

Bibliography

1. *The History of Parkinson's Disease: Early Clinical Descriptions and Neurological Therapies.* Goetz, Christopher G. 2011, Cold Spring Harbor Perspectives in Medicine.

2. Common Symptoms of Parkinson's Disease. *American Parkinson Disease Association.* [Online] [Cited: 3 February 2025.] https://www.apdaparkinson.org/what-is-parkinsons/symptoms/.

3. *Global, regional, and national burden and attributable risk factors of neurological disorders: The Global Burden of Disease study 1990–2019.* Chenyu Ding, Yuying Wu, Xiaoyong Chen, Yue Chen, Zanyi Wu, Zhangya Lin, Dezhi Kang, Wenhua Fang, Fa Chen. 952161, 2022, Frontiers of Public Health, Vol. 10.

4. *The prevalence of Parkinson's disease: a systematic review and meta-analysis.* Pringsheim, T., Jette, N., Frolkis, A., & Steeves, T. D. L. 1583-1590, s.l. : Movement Disorders: Official Journal of the Movement Disorder Society, 2014, Vol. 29(13).

5. *Prevalence of Parkinson Disease in Italy: a systematic review and meta-analysis.* Riccò, M., Vezzosi, L., Balzarini, F., Gualerzi, G., Ranzieri, S., Signorelli, C., Colucci, M. E., & Bragazzi, N. L. e2020088, s.l. : Acta Bio-Medica : Atenei Parmensis, 2020, Vol. 91(3).

6. *Prevalence of Parkinson's disease across North America.* Marras, C., Beck, J. C., Bower, J. H., Roberts, E., Ritz, B., Ross, G. W., Abbott, R. D., Savica, R., Van Den Eeden, S. K., Willis, A. W., Tanner, C. M., & Parkinson's Foundation P4 Group. 21, s.l. : NPJ Parkinson's Disease, 2018, Vol. 4.

7. *Parkinson disease.* Balestrino, R., & Schapira, A. H. V. 27-42, s.l. : European Journal of Neurology: The Official Journal of the European Federation of Neurological Societies, 2020, Vol. 27(1).

8. *Parkinson's disease.* Bloem, B. R., Okun, M. S., & Klein, C. 2284-2303, s.l. : Lancet, 2021, Vol. 397(10291).

9. *Glucocerebrosidase mutations and Parkinson disease.* Vieira, S. R. L., & Schapira, A. H. V. 1105-1117, s.l. : Journal of Neural Transmission (Vienna, Austria), 2022, Vol. 129(9).

10. What are the causes of Parkinson's Disease? *Parkinsonsdisease.net.* [Online] [Cited: 12 03 2025.] https://parkinsonsdisease.net/basics/pathophysiology-what-is-it.

11. *Advances in markers of prodromal Parkinson disease.* Postuma, R. B., & Berg, D. 622-634, s.l. : Nature Reviews, 2016, Vol. 12(11).

12. Association, American Parkinson Disease. Symptoms of Parkinson's. [Online] [Cited: 12 03 2025.] https://www.apdaparkinson.org/what-is-parkinsons/symptoms/.

13. *Many faces of Parkinson's disease: Non-motor symptoms of Parkinson's disease.* Lee, H. M., & Koh, S.-B. 92-97, s.l. : Journal of Movement Disorders, 2015, Vol. 8(2).

14. *MDS clinical diagnostic criteria for Parkinson's disease: MDS-PD Clinical Diagnostic Criteria.* Postuma, R. B., Berg, D., Stern, M., Poewe, W., Olanow, C. W., Oertel, W., Obeso, J., Marek, K., Litvan, I., Lang, A. E., Halliday, G., Goetz, C. G., Gasser, T., Dubois, B., Chan, P., Bloem, B. R., Adler, C. H., & Deuschl, G. 1591-1601, s.l. : Movement Disorders: Official Journal of the Movement Disorder Society, 2015, Vol. 30(12).

15. *Parkinsonian syndromes.* Williams, D. R., & Litvan, I. 1189-1212, s.l. : Continuum, 2013, Vol. 19(5).

16. *Impact of DaTscan imaging on clinical decision making in clinically uncertain Parkinson's disease.* Isaacson, J. R., Brillman, S., Chhabria, N., & Isaacson, S. H. 885-889, s.l. : Journal of Parkinson's Disease, 2021, Vol. 11(2).

17. *Parkinson's Disease.* Poewe, W., Seppi, K., Tanner, C. M., Halliday, G. M., Brundin, P., Volkmann, J., Schrag, A.-E., & Lang, A. E. 17013, s.l. : Nature Reviews. Disease Primers, 2017, Vol. 3.

18. *Levodopa-induced dyskinesia in Parkinson disease: A population-based cohort study.* Turcano, P., Mielke, M. M., Bower, J. H., Parisi, J. E., Cutsforth-Gregory, J. K., Ahlskog, J. E., & Savica, R. e2238-e2243, s.l. : Neurology, 2018, Vol. 91(24).

19. *Deep brain stimulation for Parkinson's disease: meta-analysis of results of randomized trials at varying lengths of follow-up.* Mansouri, A., Taslimi, S., Badhiwala, J. H., Witiw, C. D., Nassiri, F., Odekerken, V. J. J., De Bie, R. M. A., Kalia, S. K., Hodaie, M., Munhoz, R. P., Fasano, A., & Lozano, A. M. 1199-1213, s.l. : Journal of Neurosurgery, 2018, Vol. 128(4).

20. *A-synuclein in Parkinson's disease.* Stefanis, L. a009399, s.l. : Cold Spring Harbor Perspectives in Medicine, 2012, Vol. 2(2).

21. *A-synuclein - regulator of exocytosis, endocytosis, or both? .* Lautenschläger, J., Kaminski, C. F., & Kaminski Schierle, G. S. 468-479, s.l. : Trends in Cell Biology, 2017, Vol. 27(7).

22. *Alpha-synuclein promotes SNARE-complex assembly in vivo and in vitro.* Burré, J., Sharma, M., Tsetsenis, T., Buchman, V., Etherton, M. R., & Südhof, T. C. 1663–1667, s.l. : Science, 2010, Vol. 329(5999).

23. *Neurodegeneration and the ordered assembly of α-synuclein.* Spillantini, M. G., & Goedert, M. 137–148, s.l. : Cell and Tissue Research, 2018, Vol. 373(1).

24. *Alpha-Synuclein in Parkinson's Disease: From Pathogenetic Dysfunction to Potential Clinical Application.* Lingjia Xu, Jiali Pu. s.l. : Parkinson's Disease, 2016, Vol. 1720621.

25. *Exposure to pesticides or solvents and risk of Parkinson disease.* Pezzoli, G., & Cereda, E. 2035-2041, s.l. : Neurology, 2013, Vol. 80(22).

26. *Intermediates of α-synuclein aggregation: Implications in Parkinson's disease pathogenesis.* Gadhe, L., Sakunthala, A., Mukherjee, S., Gahlot, N., Bera, R., Sawner, A. S., Kadu, P., & Maji, S. K. 106736, s.l. : Biophysical Chemistry, 2022, Vol. 281(106736).

27. *The prion-like spreading of alpha-synuclein in Parkinson's disease: Update on models and hypotheses.* Jan, A., Gonçalves, N. P., Vaegter, C. B., Jensen, P. H., & Ferreira, N. 8338, s.l. : International Journal of Molecular Sciences, 2021, Vol. 22(15).

28. *Mechanisms of secretion and spreading of pathological tau protein.* Brunello, C. A., Merezhko, M., Uronen, R.-L., & Huttunen, H. J. 1721-1744, s.l. : Cellular and Molecular Life Sciences: CMLS, 2020, Vol. 77(9).

29. *Neuronal spreading and plaque induction of intracellular Aβ and its disruption of Aβ homeostasis.* Roos, T. T., Garcia, M. G., Martinsson, I., Mabrouk, R., Israelsson, B., Deierborg, T., Kobro-Flatmoen, A., Tanila, H., & Gouras, G. K. 669-687, s.l. : Acta Neuropathologica, 2021, Vol. 142(4).

30. *Amyloid-beta peptides trigger aggregation of alpha-synuclein in vitro.* Köppen, J., Schulze, A., Machner, L., Wermann, M., Eichentopf, R., Guthardt, M., Hähnel, A., Klehm, J., Kriegeskorte, M.-C., Hartlage-Rübsamen, M., Morawski, M., von Hörsten, S., Demuth, H.-U., Roßner, S., & Schilling, S. 580, s.l. : Molecules, 2020, Vol. 25(3).

31. *The link between the GBA gene and parkinsonism.* Sidransky, E., & Lopez, G. 986–998, s.l. : Lancet Neurology, 2012, Vol. 11(11).

32. *Large-scale screening of the Gaucher's disease-related glucocerebrosidase gene in Europeans with Parkinson's disease.* Lesage, S., Anheim, M., Condroyer, C., Pollak, P., Durif, F., Dupuits, C., Viallet, F., Lohmann, E., Corvol, J.-C., Honoré, A., Rivaud, S., Vidailhet, M., Dürr, A., Brice, A., & French Parkinson's Disease Genetics Study Group. 202–210, s.l. : Human Molecular Genetics, 2011, Vol. 20(1).

33. *Cross-talks among GBA mutations, glucocerebrosidase, and α-synuclein in GBA-associated Parkinson's disease and their targeted therapeutic approaches: a comprehensive review.* Balestrino, R., & Schapira, A. H. V. (2020). Parkinson disease. European Journal of Neurology: The Official Journal of the European Federation of Neurological Societies, 27(1), 27–42. https://doi.org/10.1111/ene.14108. 4, s.l. : Translational Neurodegeneration, 2021, Vol. 10(1).

34. *Survival and dementia in GBA-associated Parkinson's disease: The mutation matters.* Cilia, R., Tunesi, S., Marotta, G., Cereda, E., Siri, C., Tesei, S., Zecchinelli, A. L., Canesi, M., Mariani, C. B., Meucci, N., Sacilotto, G., Zini, M., Barichella, M., Magnani, C., Duga, S., Asselta, R., Soldà, G., Seresini, A., Seia, M., … Goldwurm, S. 662–673, s.l. : Annals of Neurology, 2016, Vol. 80(5).

35. *GBA variants and Parkinson disease: Mechanisms and treatments.* Smith, L., & Schapira, A. H. V. 1261, s.l. : Cells, 2022, Vol. 11(8).

36. *Loss of glucocerebrosidase 1 activity causes lysosomal dysfunction and α-synuclein aggregation.* Bae, E.-J., Yang, N. Y., Lee, C., Lee, H.-J., Kim, S., Sardi, S. P., & Lee, S.-J. e153, s.l. : Experimental & Molecular Medicine, 2015, Vol. 47(3).

37. *The effect of mutant GBA1 on accumulation and aggregation of α-synuclein.* Maor, G., Rapaport, D., & Horowitz, M. 1768–1781, s.l. : Human Molecular Genetics, 2019, Vol. 28(11).

38. *L444P Gba1 mutation increases formation and spread of α-synuclein deposits in mice injected with mouse α-synuclein pre-formed fibrils.* Migdalska-Richards, A., Wegrzynowicz, M., Harrison, I. F., Verona, G., Bellotti, V., Spillantini, M. G., & Schapira, A. H. V. e0238075, s.l. : PloS One, 2020, Vol. 15(8).

39. *Introduction to the Basics of Magnetic Resonance Imaging.* Klaus Mollenhoff, Ana-Maria Oros-Peusquens, and N. Jon Shah. 2012.

40. *Magnetic resonance imaging: Historical overview, technical developments, and clinical applications.* Jahng, G.-H., Park, S., Ryu, C.-W., & Cho, Z.-H. 35–53, s.l. : Progress in Medical Physics, 2020, Vol. 31(3).

41. *Imaging artifacts at 3.0T. Journal of Magnetic Resonance Imaging.* Bernstein, M. A., Huston, J., 3rd, & Ward, H. A. 735–746, s.l. : Journal of Magnetic Resonance Imaging, 2006, Vol. 24(4).

42. SE., Forshult. *Magnetic Resonance Imaging: MRI: An Overview.* Karlstad University : Faculty of Technology and Science, Physics, 2007.

43. *MP2RAGE, a self bias-field corrected sequence for improved segmentation and T1-mapping at high field.* Marques, J. P., Kober, T., Krueger, G., van der Zwaag, W., Van de Moortele, P.-F., & Gruetter, R. 1271-1281, s.l. : NeuroImage, 2010, Vol. 49(2).

44. *Invited article: an MRI-based approach to the diagnosis of white matter disorders.* Schiffmann, R., & van der Knaap, M. S. s.l. : Neurology, 2009.

45. Baba, Y., & Niknejad, M. Fluid attenuated inversion recovery. *Radiopaedia.org.* [Online]

46. *Within-subject template estimation for unbiased longitudinal image analysis.* Reuter, M., Schmansky, N. J., Rosas, H. D., & Fischl, B. s.l. : NeuroImage, 2012.

47. *Metabolic and vascular origins of the BOLD effect: Implications for imaging pathology and resting-state brain function: Understanding BOLD in Disease and Rest.* Mark, C. I., Mazerolle, E. L., & Chen, J. J. 2015.

48. *nvestigations of recovery following optic neuritis using functional and structural imaging.* Zayed, N. M. H. 2010.

49. *Coupling mechanism and significance of the BOLD signal: a status report.* Hillman, E. M. C. s.l. : Annual Review of Neuroscience, 2014.

50. *Overview of functional magnetic resonance imaging.* Glover, G. H. s.l. : Neurosurgery Clinics of North America, 2011.

51. *Functional connectivity in the motor cortex of resting human brain using echo-planar MRI. .* Biswal, B., Yetkin, F. Z., Haughton, V. M., & Hyde, J. S. s.l. : Magnetic Resonance in Medicine, 1995.

52. *Resting-state fMRI: a review of methods and clinical applications.* Lee, M. H., Smyser, C. D., & Shimony, J. S. s.l. : AJNR. American Journal of Neuroradiology, 2013.

53. *Machine learning models for diagnosis of Parkinson's disease using multiple structural magnetic resonance imaging features.* a, Y., Ji, L., Jia, Y., Zou, N., Jiang, Z., Yin, H., Mao, C., Luo, W., Wang, E., & Fan, G. s.l. : Frontiers in Aging Neuroscience, 2022.

54. *Progression of grey and white matter brain damage in Parkinson's disease: a critical review of structural MRI literature.* Sarasso, E., Agosta, F., Piramide, N., & Filippi, M. s.l. : Journal of Neurology, 2021.

55. *A review of diagnostic imaging approaches to assessing Parkinson's disease.* Samson, E., & Noseworthy, M. D. s.l. : Brain Disorders , 2022.

56. *Neuroimaging in glucocerebrosidase-associated parkinsonism: A systematic review.* Filippi, M., Balestrino, R., Basaia, S., & Agosta, F. s.l. : Movement Disorders: Official Journal of the Movement Disorder Society, 2022.

57. *Default-mode network connectivity in cognitively unimpaired patients with Parkinson disease.* Tessitore, A., Esposito, F., Vitale, C., Santangelo, G., Amboni, M., Russo, A., Corbo, D., Cirillo, G., Barone, P., & Tedeschi, G. s.l. : Neurology, 2012.

58. *Within- and across-network alterations of the sensorimotor network in Parkinson's disease. .* Caspers, J., Rubbert, C., Eickhoff, S. B., Hoffstaedter, F., Südmeyer, M., Hartmann, C. J., Sigl, B., Teichert, N., Aissa, J., Turowski, B., Schnitzler, A., & Mathys, C. s.l. : Neuroradiology, 2021.

59. *The study of brain functional connectivity in Parkinson's disease.* Gao, L.-L., & Wu, T. s.l. : Translational Neurodegeneration, 2016.

60. *Mining imaging and clinical data with machine learning approaches for the diagnosis and early detection of Parkinson's disease. .* Zhang, J. 2022.

61. *Characterization of early stage Parkinson's disease from resting-state fMRI data using a long short-term memory network.* Guo, X., Tinaz, S., & Dvornek, N. C. s.l. : Frontiers in Neuroimaging, Guo, X., Tinaz, S., & Dvornek, N. C. .

62. *Levodopa changes functional connectivity patterns in subregions of the primary motor cortex in patients with Parkinson's disease.* Shen, Y., Hu, J., Chen, Y., Liu, W., Li, Y., Yan, L., Xie, C., Zhang, W., Yu, M., & Liu, W. s.l. : Frontiers of Neuroscience, 2020.

63. *Functional connectivity analysis in heterozygous glucocerebrosidase mutation carriers.* Sezgin, M., Kicik, A., Bilgic, B., Kurt, E., Bayram, A., Hanagası, H., Tepgec, F., Toksoy, G., Gurvit, H., Uyguner, O., Gokcay, G., Demiralp, T., & Emre, M. s.l. : Journal of Parkinson's Disease, 2021.

64. *Graph theory methods: applications in brain networks.* https://doi.org/10.31887/DCNS.2018.20.2/osporns. s.l. : Dialogues in Clinical Neuroscience, 2018.

65. *Network attributes for segregation and integration in the human brain.* Sporns, O. s.l. : Current Opinion in Neurobiology, 2013.

66. *Application of graph theory for identifying connectivity patterns in human brain networks: A systematic review.* Farahani, F. V., Karwowski, W., & Lighthall, N. R. s.l. : Frontiers in Neuroscience.

67. *Global and regional connectivity analysis of resting-state function MRI brain images using graph theory in Parkinson's disease.* Prajapati, R., & Emerson, I. A. s.l. : The International Journal of Neuroscience, 2021.

68. *Network-based statistic: identifying differences in brain networks.* Zalesky, A., Fornito, A., & Bullmore, E. T. s.l. : NeuroImage, 2010.

69. *Network-based statistic show aberrant functional connectivity in Alzheimer's disease.* Zhan, Y., Yao, H., Wang, P., Zhou, B., Zhang, Z., Guo, Y., An, N., Ma, J., Zhang, X., & Liu, Y. s.l. : IEEE Journal of Selected Topics in Signal Processing, 2016.

70. *Functional connectivity in Parkinson's disease candidates for deep brain stimulation.* Albano, L., Agosta, F., Basaia, S., Cividini, C., Stojkovic, T., Sarasso, E., Stankovic, I., Tomic, A., Markovic, V., Stefanova, E., Mortini, P., Kostic, V. S., & Filippi, M. s.l. : NPJ Parkinson's Disease, 2022.

71. *Network structure and transcriptomic vulnerability shape atrophy in frontotemporal dementia.* Shafiei, G., Bazinet, V., Dadar, M., Manera, A. L., Collins, D. L., Dagher, A., Borroni, B., Sanchez-Valle, R., Moreno, F., Laforce, R., Graff, C., Synofzik, M., Galimberti, D., Rowe, J. B., Masellis, M., Tartaglia, M. C., Finger, E., Vandenberghe, R., de. s.l. : Brain: A Journal of Neurology, 2023.

72. *Predicting longitudinal brain atrophy in Parkinson's disease using a Susceptible-Infected-Removed agent-based model.* Abdelgawad, A., Rahayel, S., Zheng, Y.-Q., Tremblay, C., Vo, A., Misic, B., & Dagher, A. s.l. : Network Neuroscience , 2023.

73. *Discovering a reaction-diffusion model for Alzheimer's disease by combining PINNs with symbolic regression.* Zhang, Z., Zou, Z., Kuhl, E., & Karniadakis, G. E. s.l. : arXiv [cs.LG], 2023.

74. *Characterizing the clinical features and atrophy patterns of MAPT-related frontotemporal dementia with disease progression modeling.* Young, A. L., Bocchetta, M., Russell, L. L., Convery, R. S., Peakman, G., Todd, E., Cash, D. M., Greaves, C. V., van Swieten, J., Jiskoot, L., Seelaar, H., Moreno, F., Sanchez-Valle, R., Borroni, B., Laforce, R., Jr, Masellis, M., Tartaglia, M. C., Graff,. s.l. : Neurology, 2022.

75. *Model-based whole-brain perturbational landscape of neurodegenerative diseases. .* Sanz Perl, Y., Fittipaldi, S., Gonzalez Campo, C., Moguilner, S., Cruzat, J., Fraile-Vazquez, M. E., Herzog, R., Kringelbach, M. L., Deco, G., Prado, P., Ibanez, A., & Tagliazucchi, E. s.l. : eLife, 2023.

76. *A mathematical model on the propagation of tau pathology in neurodegenerative diseases. .* Chen, C. Y., Tseng, Y. H., & Ward, J. P. s.l. : Journal of Mathematical Biology, 2024.

77. *A network-level transport model of tau progression in the Alzheimer's brain.* Tora, V., Torok, J., Bertsch, M., & Raj, A. s.l. : arXiv [math.AP], 2024.

78. *A network diffusion model of disease progression in dementia.* Raj, A., Kuceyeski, A., & Weiner, M. s.l. : Neuron, 2012.

79. *Predictive model of spread of Parkinson's pathology using network diffusion.* Pandya, S., Zeighami, Y., Freeze, B., Dadar, M., Collins, D. L., Dagher, A., & Raj, A. s.l. : NeuroImage, 2019.

80. *Network diffusion model predicts neurodegeneration in limb-onset Amyotrophic Lateral Sclerosis.* Bhattarai, A., Chen, Z., Chua, P., Talman, P., Mathers, S., Chapman, C., Howe, J., Lee, C. M. S., Lie, Y., Poudel, G. R., & Egan, G. F. s.l. : PloS One, 2022.

81. *From reaction kinetics to dementia: A simple dimer model of Alzheimer's disease etiology.* Lindstrom, M. R., Chavez, M. B., Gross-Sable, E. A., Hayden, E. Y., & Teplow, D. B. s.l. : PLoS Computational Biology, 2021.

82. *A network aggregation model for the dynamics and treatment of neurodegenerative diseases at the brain scale.* Brennan, G. S., & Goriely, A. s.l. : arXiv [math.DS], 2024.

83. *Combined Model of Aggregation and Network Diffusion Recapitulates Alzheimer's Regional Tau-Positron Emission Tomography.* Raj, A., Tora, V., Gao, X., Cho, H., Choi, J. Y., Ryu, Y. H., Lyoo, C. H., & Franchi, B. s.l. : NeuroImage, 2021.

84. *Probing the kinetics of beta-amyloid self-association.* Murphy, R. M., & Pallitto, M. M. s.l. : Journal of Structural Biology, 2000.

85. *Achdou, Y., Franchi, B., Marcello, N., & Tesi, M. C. .* Achdou, Y., Franchi, B., Marcello, N., & Tesi, M. C. s.l. : Journal of Mathematical Biology, 2013.

86. *Modelling pathological spread through the structural connectome in the frontotemporal dementia clinical spectrum.* Agosta, F., Basaia, S., Spinelli, E. G., Facente, F., Lumaca, L., Ghirelli, A., Canu, E., Castelnovo, V., Sibilla, E., Tripodi, C., Freri, F., Cecchetti, G., Magnani, G., Caso, F., Verde, F., Ticozzi, N., Silani, V., Caroppo, P., Prioni, S., … Filippi, M. s.l. : Brain: A Journal of Neurology, 2024.

87. *A method for inferring regional origins of neurodegeneration.* Torok, J., Maia, P. D., Powell, F., Pandya, S., & Raj, A. s.l. : Brain: A Journal of Neurology, 2018.

88. *Modelling amyloid fibril formation kinetics: mechanisms of nucleation and growth.* Gillam, J. E., & MacPhee. s.l. : Condensed Matter: An Institute of Physics Journal, 2013.

89. *Accuracy of clinical diagnosis of idiopathic Parkinson's disease: a clinico-pathological study of 100 cases. .* Hughes, A. J., Daniel, S. E., Kilford, L., & Lees, A. J. s.l. : Journal of Neurology, Neurosurgery, and Psychiatry, 1992.

90. *http://surfer.nmr.mgh.harvard.edu/.* [Online]

91. *An automated labeling system for subdividing the human cerebral cortex on MRI scans into gyral based regions of interest.* Desikan, R. S., Ségonne, F., Fischl, B., Quinn, B. T., Dickerson, B. C., Blacker, D., Buckner, R. L., Dale, A. M., Maguire, R. P., Hyman, B. T., Albert, M. S., & Killiany, R. J. s.l. : NeuroImage, 2006.

92. *http://www.fmrib.ox.ac.uk/fsl/first/index.html.* [Online]

93. *http://www.fmrib.ox.ac.uk/fsl/sienax/index.html.* [Online]

94. *https://web.mit.edu/fsl_v5.0.10/fsl/doc/wiki/FAST.html.* [Online]

95. *https://web.mit.edu/fsl_v5.0.10/fsl/doc/wiki/FLIRT.html.* [Online]

96. *Neuronal spreading and plaque induction of intracellular Aβ and its disruption of Aβ homeostasis.* Rohde, G. K., Aldroubi, A., & Dawant, B. M. s.l. : Acta Neuropathologica, 2021.

97. *https://www.nitrc.org/projects/trackvis.* [Online]

98. *Structural brain connectome and cognitive impairment in Parkinson disease.* Galantucci, S., Agosta, F., Stefanova, E., Basaia, S., van den Heuvel, M. P., Stojković, T., Canu, E., Stanković, I., Spica, V., Copetti, M., Gagliardi, D., Kostić, V. S., & Filippi, M. s.l. : Radiology, 2017.

99. *Mathematics of networks.* Newman, M. s.l. : Oxford University Press., 2018.

100. *https://www.mathworks.com/help/matlab/ref/ode45.html.* [Online]

101. *https://it.mathworks.com/help/gads/surrogateopt.html.* [Online]

102. *https://it.mathworks.com/help/matlab/ref/parfor.html.* [Online]

103. *Lateralisation in Parkinson disease. .* Riederer, P., Jellinger, K. A., Kolber, P., Hipp, G., Sian-Hülsmann, J., & Krüger, R. s.l. : Cell and Tissue Research, 2018.